Fermilab FERMILAB-THESIS-1998-43

Measurement of the Strong Coupling Constant from Two Jet Production Cross Section in 1.8-TeV Proton-Antiproton Collisions

Masakazu OKABE

Measurement of the Strong Coupling Constant from Two Jet Production Cross Section in 1.8-TeV Proton-Antiproton Collisions

January, 1998

Masakazu OKABE

A dissertation submitted to the Doctoral Program in Physics,
the University of Tsukuba
in partial fulfillment of the requirements for the degree of
Doctor of Philosophy (Science)

Abstract

We present the α_s measurement using two jet production cross sections in proton-antiproton collisions at a center of mass energy of 1.8 TeV. The experiment has been performed at the Fermi National Accelerator Laboratory in the United States using the Tevatron accelerator. The data were collected with the Collider Detector at Fermilab (CDF) during the 1994-95 Tevatron collider run, corresponding to an integrated luminosity of 86.3 pb^{-1}. Requiring one central jet and another (*second*) jet with $E_T > 10$ GeV, the two jet differential cross sections were measured as a function of E_T of the central jet in four different pseudorapidity (η) bins of the *second* jet. The cross sections are shown in the transverse energy range from 40 to ~ 400 GeV in the η range from 0.1 to 3.0. The magnitude and the shape of the cross section are sensitive to α_s through the higher order QCD processes. We evaluate α_s by fitting the cross sections to a theoretical calculation with various structure functions. The resulting α_s values for various structure functions are consistent to each other within $\Delta\alpha_s(\mathrm{M_Z}) \simeq \pm 0.005$. The running feature of α_s is clearly seen. We quote $\alpha_s(\mathrm{M_Z}) = 0.117 \pm 0.001(stat.) \pm 0.009(exp.sys.)$ where the first uncertainty is statistical and the second is the experimental systematic uncertainty only. This is the first measurement of α_s obtained at hadron colliders where pure QCD processes are involved. This result is consistent with the world average of 0.118 ± 0.003.

Acknowledgements

I would like to thank my thesis advisor, Professor Shinhong Kim, for his guidance and encouragements throughout my graduate career. His critical suggestions have been my motive power to carry out the present research. I express my gratitude to Professor Kunitaka Kondo who is the former CDF Japan group leader and Professor Koji Takikawa who is the present leader since 1995 for giving me the opportunity to work at CDF and for their continuous support in my research activity.

Discussions with Professor Shigeyuki Miyashita are unforgettable; the idea of the present thesis subject has come to my mind through the discussions with him. I wish to express my deepest appreciation to Professor Kazuhiko Hara, with whom I have discussed on physics and other various things. The present work would not have been finished without his continuous help.

I would like to thank the members of CDF QCD physics group: Drs. Michael G. Albrow, Joey Huston, Stephen E. Kuhlmann, Al Goshaw, Robert Plunkett, Stephan Behrends, Stephan Geer, Elizabeth Buckley-Geer, Eve Kovacs, Brenna Flaugher, Robert M. Harris, Anwar A. Bhatti, and Frank Chlebana. They gave me useful comments and suggestion while I was staying at Fermilab.

Dr. Walter T. Giele of Fermilab kindly let us use his program JETRAD which has been the key tool in this analysis.

Conversations with Professor Taiji Yamanouchi, Professor Masanori Mishina, Professor Junsuke Iwai, and Dr. Nobuaki Oshima are unforgettable and informative. I was very fortunate to have a good time in Warrenville with my roommates Mr. Mark Whitmer and Dr. Charles Nelson.

Discussions with Professor Kiyoshi Yasuoka and Professor Yoshihiro Seiya, and with my colleagues, Dr. Ryutaro Oishi, Mr. Masahiko Yokoyama, Dr. Makoto Shimojima, Mr. Nobuyuki Uemura, Dr. Takashi Asakawa, Mr. Tsuyoshi Takada, Mr. Toshiharu Uchida, Mr. Junichi Suzuki, Dr. Takeshi Takano, and other members of the Tsukuba high energy physics group were very useful to me.

I would like to express my great appreciation to Ms. Carol Picciolo, Ms. Kyoko Kunori, Ms. Mutsumi Uenishi, and Ms. Kazuko Kumashiro for their kind secretarial

works.

We thank the Fermilab staff and the technical staffs of the participating institutions for their vital contributions. This work was supported by the U.S. Department of Energy and National Science Foundation; the Italian Istituto Nazionale di Fisica Nucleare; the Ministry of Education, Science and Culture of Japan; the Natural Sciences and Engineering Research Council of Canada; the National Science Council of the Republic of China; the A. P. Sloan Foundation; and the Alexander von Humboldt-Stiftung.

Contents

1 Introduction **1**

1.1 Quantum Chromodynamics (QCD) 1

1.2 Previous α_s measurements 6

1.2.1 α_s from e^+e^- collisions 6

1.2.2 α_s from lepton-hadron collisions 15

1.2.3 α_s from hadron-hadron collisions 17

1.3 Outline of the Thesis 18

2 Apparatus **19**

2.1 Tevatron 19

2.2 Collider Detector at Fermilab 22

2.2.1 Tracking detectors 23

2.2.2 Calorimeters 25

2.2.3 Muon detectors 30

2.2.4 Beam-beam counter 31

2.2.5 Trigger system 31

2.2.6 Data acquisition system 32

2.2.7 Luminosity measurement 41

3 Two jet production cross section **43**

3.1 Event selection 43

3.1.1 Jet triggers 43

3.1.2 Jet reconstruction 44

3.1.3 Two jet event selection 45

3.2 Detection efficiency 46

3.2.1 Event vertex cut 46
3.2.2 $\not{E}_{\mathrm{T}}$ significance cut 47
3.2.3 Trigger efficiency 47
3.3 Two Jet Cross Section 50
3.3.1 E_{T} smearing due to finite calorimeter response 50
3.3.2 Central jet response function 51
3.3.3 Two jet production cross section 57
3.4 Systematic Uncertainties 61

4 Measurement of α_{s} 74

4.1 α_{s} determination from two jet production cross sections 74
4.1.1 Two jet production cross sections in NLO QCD 74
4.1.2 α_{s} with CTEQ4M structure functions 76
4.1.3 α_{s} with other structure functions 78
4.2 Systematic uncertainties on α_{s} 91
4.2.1 Experimental systematic uncertainties 91
4.2.2 Theoretical systematic uncertainties 92

5 Conclusion 103

List of Tables

2.1 Summary of CDF calorimeter properties. The symbol $\oplus$ signifies that the constant term is added in quadrature in the resolution. Energy resolutions for the electromagnetic calorimeters are for incident electrons and photons, and for the hadronic calorimeters are for incident isolated pions. Energy is given in GeV. Thicknesses are given in radiation lengths (X_0) and interaction lengths (λ) for the electromagnetic and hadronic calorimeters, respectively. 25

3.1 Integrated luminosity, prescale factors (PF), threshold transverse energies (in GeV), and E_{T} range used in this analysis. The numbers are given for jet triggers, Jet20 to Jet100 and for level-1 to level-3. No level-1 prerequisite is made at level-2 for Jet70 and Jet100, and no level-2 prerequisite at level-3 for Jet100. 44

3.2 Two jet cross sections as a function of the central jet E_{T}. Cross sections are listed for four η regions of the *second* jet with the central jet in $0.1<|\eta|<0.7$. $E_{\mathrm{T}}^{measured}$ is the measured E_{T} (pre-unsmearing). E_{T}^{*Low}, $<E_{\mathrm{T}}^{*}>$, and E_{T}^{*High} are the unsmeared values. The cross sections are divided by the $E_{\mathrm{T}}^{measured}$ bin width and η_1 and η_2 bin widths. 58

3.2 (Continued). 59

3.3 Fitted parameters for the true cross section curves in the region $0.1 < |\eta_1| < 0.7$ and $0.1 < |\eta_2| < 0.7$. Also shown are the parameters when one of the sources of systematic uncertainties is changed by ± 1 standard deviation. 65

3.3 (Continued). 66

3.4 The percentage change in the cross section from various "negative" systematic contributions. The "All" values are systematic uncertainties of all contributions (see text) added in quadrature. 67
3.4 (Continued) 68
3.5 The percentage change in the cross section from various "positive" systematic contributions and from uncertainty in the functional form of the calorimeter response function. The "All" values are systematic uncertainties of all contributions (see text) added in quadrature. . . . 69
3.5 (Continued). 70

4.1 Two jet cross section, calculated A_1, A_2, A_3, $\alpha_s(\mu)$, and $\alpha_s(M_Z)$ on each μ and η_2 bin. They are from JETRAD calculation using CTEQ4M structure function with energy scale $\mu_R = \mu_F = 0.5E_T$. The μ is the mean value of $0.5E_T$, where E_T is the transverse energy of the central jet ($0.1 < |\eta_1| < 0.7$), weighted by the differential cross section on each bin. 80
4.2 Similar to Table 4.1, but with energy scale $\mu_R = \mu_F = E_T$. 81
4.3 Similar to Table 4.1, but obtained using CTEQ4HJ. 82
4.4 Similar to Table 4.3, but with energy scale $\mu_R = \mu_F = E_T$. 83
4.5 Calculated $\alpha_s(M_Z)$ using various structure functions with energy scale $\mu_R = \mu_F = 0.5E_T$. The uncertainties are the rms spread of the weighted distribution of $\alpha_s(M_Z)$ calculated in each bin, which correspond to the statistical uncertainties conservatively. The range of $\alpha_s(M_Z)$ due to the systematic uncertainties of the cross section is shown in parentheses. 84
4.5 (Continued). 85
4.6 Similar to Table 4.1, but the energy scales are defined as $\mu = E_T$. . . 85
4.7 Contributions to the $\alpha_s(M_Z)$ uncertainty from various sources that determine the calorimeter response function. 92
4.8 Contributions to the theoretical uncertainties on $\alpha_s(M_Z)$. 94

List of Figures

1.1 Comparison among $\alpha_s(\mu_R)$'s summed to the first, second, third, and fourth orders in $\ln(\mu^2)^{-1}$ [see Eq.(1.25)]. The solid curve is the solution exact to $\mathcal{O}(\alpha_s^3)$. $\alpha_s(M_Z)$ is fixed to 0.118. The right plot shows the ratio normalized by the solid function. $\alpha_s(\mu_R)$ to the first order is not shown; it reaches out of the range of this plot. 7

2.1 Diagram of the Tevatron accelerator complex at Fermilab. 21

2.2 A perspective view of the CDF detector showing the central detector, the forward and the backward detectors. 34

2.3 A side-view cross section of the CDF detector. The detector is forward-backward symmetric about the interaction point. 34

2.4 Cross-sectional view of the central detectors. 35

2.5 Endplate of the CTC showing the arrangement of the slots which hold in total 36,504 wires. 36

2.6 Hadron calorimeter towers in one of eight identical η-ϕ quadrants ($\Delta\phi = 90°, \eta > 0$). The heavy lines indicate module or chamber boundaries. The EM calorimeters have complete ϕ coverage out to $\eta = 4.2$. 37

2.7 Schematic of a wedge module of the central calorimeter showing the layout of the light-gathering system. 38

2.8 Map of central muon detector coverage in η-ϕ. 39

2.9 A beam's eye view of one of the beam-beam counter planes. 40

3.1 Z_{vertex} distribution of four inclusive jet triggers. The percentage in each histogram is the number of events within $|Z_{\text{vertex}}| < 60\,\text{cm}$ divided by that within $|Z_{\text{vertex}}| < 150\,\text{cm}$. 46

3.2 Missing E_{T} significance distributions for the Jet20, Jet50, Jet70, and Jet100 triggers. The distributions are truncated at 12. 48

3.3 Trigger efficiency for the Jet20, Jet50, Jet70, and Jet100 triggers. The vertical dashed lines show the range of E_{T} used in this analysis. . . . 49

3.4 Measured two jet cross section for $0.1 < |\eta_1| < 0.7$ and $0.1 < |\eta_2| < 0.7$ as a function of the measured E_{T} (pre-unsmearing) taken from either Jet20, Jet50, Jet70, or Jet100 trigger. The cross section does not correct the trigger inefficiency. 54

3.5 Parameterization of the jet response map as a function of the detector pseudorapidity η_d for different slices of jet p_{T}. 55

3.6 The Parameters of the jet response function. The RMS is defined as $(SIGMA^2 + SLP1^2 + SLP2^2)^{1/2}$. 55

3.7 The ratio of measured to true jet E_{T} for jets with a true E_{T} of 10 GeV (dotted), 50 GeV (dashed), and 200 GeV (solid). The measured E_{T} is smeared by a parameterization of the detector response. 56

3.8 Cross section for two jet production as a function of the central ($0.1 < |\eta_1| < 0.7$) jet E_{T} (unsmeared). The unsmeared data (listed in column 7 in Table 3.2) are shown for four different η bins of the other most energetic jets. The uncertainties are statistical only. The unsmeared physics functions fitted to the data are given in text. 60

3.9 CDF central calorimeter response (E/p) to pions as a function of incident momentum. The high energy data are obtained from test beam measurements, and low energy data (≤ 12 GeV) are obtained from isolated tracks in minimum bias events. 64

3.10 The percentage changes in the cross section. The electron/photon response and the parton fragmentation function is changed by ± 1 standard deviation from the standard one. The underlying event energy is changed by $\pm 30\%$. The jet energy resolution is changed by $\pm 10\%$. 71

3.11 The percentage changes in the cross section. The calorimeter response to charged pions at low p_{T} and high p_{T} is changed by ± 1 standard deviation from the standard one. The calorimeter energy scale instability is changed by $\pm 1\%$. The response function is simplified to the gaussian. 72

3.12 Statistical and the total systematic uncertainties versus central jet E_{T}. The vertical line shows the statistical uncertainty and the curve is the systematic uncertainty including the normalization uncertainty of 8.0%. 73

4.1 The contributions of the LO and NLO$-$LO two jet cross sections using CTEQ4M with energy scale definition of $\mu = 0.5E_{\mathrm{T}}$ or $\mu = E_{\mathrm{T}}$. In high η_2 and E_{T}, NLO contribution get higher. 86

4.2 The α_{s} as a function of the central jet E_{T} obtained using CTEQ4M. The best fit $\alpha_{\mathrm{s}}(\mathrm{M_Z})$ is 0.1169 ± 0.0004 by taking in the region $0.1 < |\eta_1| < 0.7$ and $0.1 < |\eta_2| < 0.7$ with $50 < E_{\mathrm{T}} < 150$ GeV. The curve is based on this $\alpha_{\mathrm{s}}(\mathrm{M_Z})$ value with five flavors in the region $\mu = 0.5E_{\mathrm{T}} < 175$ GeV, and with six in the region beyond. 87

4.3 The α_{s} as a function of the central jet E_{T} obtained using CTEQ4HJ. The best fit $\alpha_{\mathrm{s}}(\mathrm{M_Z})$ is 0.1186 ± 0.0004 by taking in the region $0.1 < |\eta_1| < 0.7$ and $0.1 < |\eta_2| < 0.7$ with $50 < E_{\mathrm{T}} < 150$ GeV. The curve is based on this $\alpha_{\mathrm{s}}(\mathrm{M_Z})$ value with five flavors in the region $\mu = 0.5E_{\mathrm{T}} < 175$ GeV, and with six in the region beyond. 88

4.4 Similar to Fig. 4.2, but obtained using MRSA′115. The best fit $\alpha_{\mathrm{s}}(\mathrm{M_Z})$ is 0.1171 ± 0.0003. 89

4.5 Similar to Fig. 4.2, but obtained using GRV94300. The best fit $\alpha_{\mathrm{s}}(\mathrm{M_Z})$ is 0.1177 ± 0.0003. 90

4.6 The α_s obtained using CTEQ4M from systematically "deviated" cross sections. The cross section is deviated due to the electron/photon response uncertainty (-1σ), the underlying event energy (-30%), the parton fragmentation function (-1σ), or the calorimeter energy scale instability (-1%), respectively. 95

4.7 Similar to Fig. 4.6, but the cross section is deviated due to the jet energy resolution uncertainty (-10%), the calorimeter response to charged pions at low p_T (-1σ) or high p_T (-1σ), or the response function simplified to the gaussian, respectively. 96

4.8 Similar to Fig. 4.6, but the cross section is deviated due to the electron/photon response uncertainty ($+1\sigma$), the underlying event energy ($+30\%$), the parton fragmentation function ($+1\sigma$), or the calorimeter energy scale instability ($+1\%$), respectively. 97

4.9 Similar to Fig. 4.6, but the cross section is deviated due to the jet energy resolution uncertainty ($+10\%$), the calorimeter response to charged pions at low p_T ($+1\sigma$) or high p_T ($+1\sigma$), or the response function simplified to P6 in Eq.(3.9) being 0, respectively. 98

4.10 Similar to Fig. 4.2, but the energy scales are defined as $\mu = E_T$. The best fit $\alpha_s(M_Z)$ is 0.1215 ± 0.0004. The number of flavors is assumed to change to six at $\mu = 175$ GeV. 99

4.11 Similar to Fig. 4.3, but the energy scales are defined as $\mu = E_T$. The best fit $\alpha_s(M_Z)$ is 0.1238 ± 0.0004. 100

4.12 Summary of the $\alpha_s(M_Z)$ measurements. The obtained $\alpha_s(M_Z)$ values are shown for some of the recent structure functions. The circle and triangle are the central values of α_s with the factorization and renormalization scales defined as, $0.5E_T$ and E_T, respectively. The bar shows the statistical and total systematic error due to the cross section uncertainty; inside bar shows the statistical error only. X is the $\alpha_s(M_Z)$ used at parton evolution for each structure function. . . . 101

4.13 "Input" $\alpha_s(M_Z)$ versus "output" $\alpha_s(M_Z)$. "Input" $\alpha_s(M_Z)$ is the one used at parton evolution for each structure function. "Output" $\alpha_s(M_Z)$ is value obtained by a comparison with the experimental cross section. The vertical line shows the place where "Input" and "output" values are the same. CTEQ4M is equivalent to CTEQ4A3. 102

5.1 The result of $\alpha_s(M_Z)$ comparison with other measurements. Filled symbols are derived using NNLO QCD; open symbols are derived using NLO QCD or based on lattice calculations. The vertical line and the shaded area represent the world average of 0.118 ± 0.006, where the uncertainty of 0.006 corresponds to a estimate of a "90% confidence level", derived from the scatter of the individual results. . 104

The CDF Collaboration

F. Abe,[14] H. Akimoto,[32] A. Akopian,[27] M. G. Albrow,[7] S. R. Amendolia,[23] D. Amidei,[17] J. Antos,[29] C. Anway-Wiese,[4] S. Aota,[32] G. Apollinari,[27] T. Asakawa,[32] W. Ashmanskas,[15] M. Atac,[7] P. Auchincloss,[26] F. Azfar,[22] P. Azzi-Bacchetta,[21] N. Bacchetta,[21] W. Badgett,[17] S. Bagdasarov,[27] M. W. Bailey,[19] J. Bao,[35] P. de Barbaro,[26] A. Barbaro-Galtieri,[15] V. E. Barnes,[25] B. A. Barnett,[13] G. Bauer,[16] T. Baumann,[9] F. Bedeschi,[23] S. Behrends,[3] S. Belforte,[23] G. Bellettini,[23] J. Bellinger,[34] D. Benjamin,[31] J. Benlloch,[16] J. Bensinger,[3] D. Benton,[22] A. Beretvas,[7] J. P. Berge,[7] S. Bertolucci,[8] A. Bhatti,[27] K. Biery,[12] M. Binkley,[7] D. Bisello,[21] R. E. Blair,[1] C. Blocker,[3] A. Bodek,[26] W. Bokhari,[16] V. Bolognesi,[7] D. Bortoletto,[25] J. Boudreau,[24] L. Breccia,[2] C. Bromberg,[18] E. Buckley-Geer,[7] H. S. Budd,[26] K. Burkett,[17] G. Busetto,[21] A. Byon-Wagner,[7] K. L. Byrum,[1] J. Cammerata,[13] C. Campagnari,[7] M. Campbell,[17] A. Caner,[7] W. Carithers,[15] D. Carlsmith,[34] A. Castro,[21] D. Cauz,[23] Y. Cen,[26] F. Cervelli,[23] H. Y. Chao,[29] J. Chapman,[17] M.-T. Cheng,[29] G. Chiarelli,[23] T. Chikamatsu,[32] C. N. Chiou,[29] L. Christofek,[11] S. Cihangir,[7] A. G. Clark,[23] M. Cobal,[23] M. Contreras,[5] J. Conway,[28] J. Cooper,[7] M. Cordelli,[8] C. Couyoumtzelis,[23] D. Crane,[1] D. Cronin-Hennessy,[6] R. Culbertson,[5] J. D. Cunningham,[3] T. Daniels,[16] F. DeJongh,[7] S. Delchamps,[7] S. Dell'Agnello,[23] M. Dell'Orso,[23] L. Demortier,[27] B. Denby,[23] M. Deninno,[2] P. F. Derwent,[17] T. Devlin,[28] M. Dickson,[26] J. R. Dittmann,[6] S. Donati,[23] J. Done,[30] A. Dunn,[17] N. Eddy,[17] K. Einsweiler,[15] J. E. Elias,[7] R. Ely,[15] E. Engels, Jr.,[24] D. Errede,[11] S. Errede,[11] Q. Fan,[26] I. Fiori,[2] B. Flaugher,[7] G. W. Foster,[7] M. Franklin,[9] M. Frautschi,[31] J. Freeman,[7] J. Friedman,[16] H. Frisch,[5] T. A. Fuess,[1] Y. Fukui,[14] S. Funaki,[32] G. Gagliardi,[23] S. Galeotti,[23] M. Gallinaro,[21] M. Garcia-Sciveres,[15] A. F. Garfinkel,[25] C. Gay,[9] S. Geer,[7] D. W. Gerdes,[17] P. Giannetti,[23] N. Giokaris,[27] P. Giromini,[8] L. Gladney,[22] D. Glenzinski,[13] M. Gold,[19] J. Gonzalez,[22] A. Gordon,[9] A. T. Goshaw,[6] K. Goulianos,[27] H. Grassmann,[23] L. Groer,[28] C. Grosso-Pilcher,[5] G. Guillian,[17] R. S. Guo,[29] C. Haber,[15] E. Hafen,[16] S. R. Hahn,[7] R. Hamilton,[9] R. Handler,[34] R. M. Hans,[35] K. Hara,[32] A. D. Hardman,[25]

B. Harral,[22] R. M. Harris,[7] S. A. Hauger,[6] J. Hauser,[4] C. Hawk,[28] E. Hayashi,[32] J. Heinrich,[22] K. D. Hoffman,[25] M. Hohlmann,[1,5] C. Holck,[22] R. Hollebeek,[22] L. Holloway,[11] A. Hölscher,[12] S. Hong,[17] G. Houk,[22] P. Hu,[24] B. T. Huffman,[24] R. Hughes,[26] J. Huston,[18] J. Huth,[9] J. Hylen,[7] H. Ikeda,[32] M. Incagli,[23] J. Incandela,[7] G. Introzzi,[23] J. Iwai,[32] Y. Iwata,[10] H. Jensen,[7] U. Joshi,[7] R. W. Kadel,[15] E. Kajfasz,[7a] T. Kamon,[30] T. Kaneko,[32] K. Karr,[33] H. Kasha,[35] Y. Kato,[20] L. Keeble,[8] K. Kelley,[16] R. D. Kennedy,[28] R. Kephart,[7] P. Kesten,[15] D. Kestenbaum,[9] R. M. Keup,[11] H. Keutelian,[7] F. Keyvan,[4] B. Kharadia,[11] B. J. Kim,[26] D. H. Kim,[7a] H. S. Kim,[12] S. B. Kim,[17] S. H. Kim,[32] Y. K. Kim,[15] L. Kirsch,[3] P. Koehn,[26] K. Kondo,[32] J. Konigsberg,[9] S. Kopp,[5] K. Kordas,[12] W. Koska,[7] E. Kovacs,[7a] W. Kowald,[6] M. Krasberg,[17] J. Kroll,[7] M. Kruse,[25] T. Kuwabara,[32] S. E. Kuhlmann,[1] E. Kuns,[28] A. T. Laasanen,[25] N. Labanca,[23] S. Lammel,[7] J. I. Lamoureux,[3] T. LeCompte,[11] S. Leone,[23] J. D. Lewis,[7] P. Limon,[7] M. Lindgren,[4] T. M. Liss,[11] N. Lockyer,[22] O. Long,[22] C. Loomis,[28] M. Loreti,[21] J. Lu,[30] D. Lucchesi,[23] P. Lukens,[7] S. Lusin,[34] J. Lys,[15] K. Maeshima,[7] A. Maghakian,[27] P. Maksimovic,[16] M. Mangano,[23] J. Mansour,[18] M. Mariotti,[21] J. P. Marriner,[7] A. Martin,[11] J. A. J. Matthews,[19] R. Mattingly,[16] P. McIntyre,[30] P. Melese,[27] A. Menzione,[23] E. Meschi,[23] S. Metzler,[22] C. Miao,[17] G. Michail,[9] R. Miller,[18] H. Minato,[32] S. Miscetti,[8] M. Mishina,[14] H. Mitsushio,[32] T. Miyamoto,[32] S. Miyashita,[32] Y. Morita,[14] J. Mueller,[24] A. Mukherjee,[7] T. Muller,[4] P. Murat,[23] H. Nakada,[32] I. Nakano,[32] C. Nelson,[7] D. Neuberger,[4] C. Newman-Holmes,[7] M. Ninomiya,[32] L. Nodulman,[1] S. H. Oh,[6] K. E. Ohl,[35] T. Ohmoto,[10] T. Ohsugi,[10] R. Oishi,[32] M. Okabe,[32] T. Okusawa,[20] R. Oliver,[22] J. Olsen,[34] C. Pagliarone,[2] R. Paoletti,[23] V. Papadimitriou,[31] S. P. Pappas,[35] S. Park,[7] A. Parri,[8] J. Patrick,[7] G. Pauletta,[23] M. Paulini,[15] A. Perazzo,[23] L. Pescara,[21] M. D. Peters,[15] T. J. Phillips,[6] G. Piacentino,[2] M. Pillai,[26] K. T. Pitts,[7] R. Plunkett,[7] L. Pondrom,[34] J. Proudfoot,[1] F. Ptohos,[9] G. Punzi,[23] K. Ragan,[12] A. Ribon,[21] F. Rimondi,[2] L. Ristori,[23] W. J. Robertson,[6] T. Rodrigo,[7a] J. Romano,[5] L. Rosenson,[16] R. Roser,[11] W. K. Sakumoto,[26] D. Saltzberg,[5] A. Sansoni,[8] L. Santi,[23] H. Sato,[32] V. Scarpine,[30] P. Schlabach,[9] E. E. Schmidt,[7] M. P. Schmidt,[35] A. Scribano,[23] S. Segler,[7] S. Seidel,[19] Y. Seiya,[32] G. Sganos,[12] A. Sgolacchia,[2] M. D. Shapiro,[15] N. M. Shaw,[25] Q. Shen,[25]

P. F. Shepard,[24] M. Shimojima,[32] M. Shochet,[5] J. Siegrist,[15] A. Sill,[31] P. Sinervo,[12] P. Singh,[24] J. Skarha,[13] K. Sliwa,[33] F. D. Snider,[13] T. Song,[17] J. Spalding,[7] P. Sphicas,[16] F. Spinella,[23] M. Spiropulu,[9] L. Spiegel,[7] L. Stanco,[21] J. Steele,[34] A. Stefanini,[23] K. Strahl,[12] J. Strait,[7] R. Ströhmer,[9] D. Stuart,[7] G. Sullivan,[5] A. Soumarokov,[29] K. Sumorok,[16] J. Suzuki,[32] T. Takada,[32] T. Takahashi,[20] T. Takano,[32] K. Takikawa,[32] N. Tamura,[10] F. Tartarelli,[23] W. Taylor,[12] P. K. Teng,[29] Y. Teramoto,[20] S. Tether,[16] D. Theriot,[7] T. L. Thomas,[19] R. Thun,[17] M. Timko,[33] P. Tipton,[26] A. Titov,[27] S. Tkaczyk,[7] D. Toback,[5] K. Tollefson,[26] A. Tollestrup,[7] J. Tonnison,[25] J. F. de Troconiz,[9] S. Truitt,[17] J. Tseng,[13] N. Turini,[20] T. Uchida,[32] N. Uemura,[32] F. Ukegawa,[22] G. Unal,[22] S. C. van den Brink,[24] S. Vejcik, III,[17] G. Velev,[23] R. Vidal,[7] M. Vondracek,[11] D. Vucinic,[16] R. G. Wagner,[1] R. L. Wagner,[7] J. Wahl,[5] C. Wang,[6] C. H. Wang,[29] G. Wang,[23] J. Wang,[5] M. J. Wang,[29] Q. F. Wang,[27] A. Warburton,[12] G. Watts,[26] T. Watts,[28] R. Webb,[30] C. Wei,[6] C. Wendt,[34] H. Wenzel,[15] W. C. Wester, III,[7] A. B. Wicklund,[1] E. Wicklund,[7] R. Wilkinson,[22] H. H. Williams,[22] P. Wilson,[5] B. L. Winer,[26] D. Wolinski,[17] J. Wolinski,[30] X. Wu,[23] J. Wyss,[21] A. Yagil,[7] W. Yao,[15] K. Yasuoka,[32] Y. Ye,[12] G. P. Yeh,[7] P. Yeh,[29] M. Yin,[6] J. Yoh,[7] C. Yosef,[18] T. Yoshida,[20] D. Yovanovitch,[7] I. Yu,[35] J. C. Yun,[7] A. Zanetti,[23] F. Zetti,[23] L. Zhang,[34] W. Zhang,[22] and S. Zucchelli[2]

[1] *Argonne National Laboratory, Argonne, Illinois 60439*

[2] *Istituto Nazionale di Fisica Nucleare, University of Bologna, I-40126 Bologna, Italy*

[3] *Brandeis University, Waltham, Massachusetts 02254*

[4] *University of California at Los Angeles, Los Angeles, California 90024*

[5] *University of Chicago, Chicago, Illinois 60637*

[6] *Duke University, Durham, North Carolina 27708*

[7] *Fermi National Accelerator Laboratory, Batavia, Illinois 60510*

[8] *Laboratori Nazionali di Frascati, Istituto Nazionale di Fisica Nucleare, I-00044 Frascati, Italy*

[9] *Harvard University, Cambridge, Massachusetts 02138*

[10] *Hiroshima University, Higashi-Hiroshima 724, Japan*

[11] *University of Illinois, Urbana, Illinois 61801*

[12] *Institute of Particle Physics, McGill University, Montreal H3A 2T8, and University of Toronto, Toronto M5S 1A7, Canada*

[13] *The Johns Hopkins University, Baltimore, Maryland 21218*

[14] *National Laboratory for High Energy Physics (KEK), Tsukuba, Ibaraki 305, Japan*

[15] *Lawrence Berkeley Laboratory, Berkeley, California 94720*

[16] *Massachusetts Institute of Technology, Cambridge, Massachusetts 02139*

[17] *University of Michigan, Ann Arbor, Michigan 48109*

[18] *Michigan State University, East Lansing, Michigan 48824*

[19] *University of New Mexico, Albuquerque, New Mexico 87131*

[20] *Osaka City University, Osaka 588, Japan*

[21] *Universita di Padova, Istituto Nazionale di Fisica Nucleare, Sezione di Padova, I-35131 Padova, Italy*

[22] *University of Pennsylvania, Philadelphia, Pennsylvania 19104*

[23] *Istituto Nazionale di Fisica Nucleare, University and Scuola Normale Superiore of Pisa, I-56100 Pisa, Italy*

[24] *University of Pittsburgh, Pittsburgh, Pennsylvania 15260*

[25] *Purdue University, West Lafayette, Indiana 47907*

[26] *University of Rochester, Rochester, New York 14627*

[27] *Rockefeller University, New York, New York 10021*

[28] *Rutgers University, Piscataway, New Jersey 08854*

[29] *Academia Sinica, Taipei, Taiwan 11529, Republic of China*

[30] *Texas A&M University, College Station, Texas 77843*

[31] *Texas Tech University, Lubbock, Texas 79409*

[32] *University of Tsukuba, Tsukuba, Ibaraki 305, Japan*

[33] *Tufts University, Medford, Massachusetts 02155*

[34] *University of Wisconsin, Madison, Wisconsin 53706*

[35] *Yale University, New Haven, Connecticut 06511*

Chapter 1

Introduction

Measurements of the coupling strength of the strong interaction, α_s , and of its energy dependence are key issues in experimental studies of high energy particle interactions. The history [1] of α_s starts in 1973, the year of birth of Quantum Chromodynamics (QCD) [2] as an asymptotically free gauge theory of the strong interactions. The existence of gluons, mediators of the force between quarks and antiquarks, was first inferred from the observation of scaling violations in deep inelastic lepton-nucleon scattering (DIS). In 1979, gluons were directly observed in 3-jet final states of e^+e^- annihilations [3]. This process provided the first quantitative measurements of α_s, based on event shape observables which were calculated in leading order perturbative QCD [4]. The first measurement of α_s in complete next-to-leading order QCD was reported in 1982, from a study of 3-jet distributions in e^+e^- annihilations [5]. In 1988 the observed energy dependence of 3-jet event production rates [6] gave the first evidence for running of α_s, i.e. its decrease with increasing energy scale.

1.1 Quantum Chromodynamics (QCD)

The Standard Model of elementary particles and their interactions has two components: the spontaneously broken SU(2)×U(1) electroweak theory and the unbroken SU(3) color gauge theory known as Quantum Chromodynamics (QCD). In the following, we summarize briefly the framework of QCD.

QCD Lagrangian

The Lagrangian density of QCD is

$$\begin{aligned} L(x) &= L_{Gluon} + L_{Fermion} + L_{Gauge-Fixing} + L_{Faddeev-Popov} \\ &= -\frac{1}{4}(F^a_{\mu\nu})^2 + \sum_f \bar{q}_f \left(i\gamma^\mu\partial_\mu - m_f + gT^a\gamma^\mu A^a_\mu\right) q_f \\ &\quad -\frac{1}{2\alpha_G}(\partial^\mu A^a_\mu)^2 + \partial^\mu c^{a\dagger}(\delta^{ac}\partial_\mu + gf^{abc}A^b_\mu)\, c^c, \end{aligned} \tag{1.1}$$

where

$$F^a_{\mu\nu} = \partial_\mu A^a_\nu - \partial_\nu A^a_\mu + gf^{abc}A^b_\mu A^c_\nu \qquad (a = 1, \ldots, 8) \tag{1.2}$$

are the gluon field strength, g is the coupling strength, A^a and q_f are gluon and quark wavefunctions, m_f are the quark masses, c^a are the Faddeev-Popov ghost fields, and α_G is the gauge-fixing parameter.

The generators of the SU(3) gauge group obey the following commutation relations:

$$[T^a, T^b] = if^{abc}T^c, \;\; \{T^a, T^b\} = \frac{1}{N}\delta^{ab} + d^{abc}T^c, \tag{1.3}$$

$$f^{acd}f^{bcd} = C_A\delta^{ab}, \; T^aT^a = C_F\hat{1}, \; tr\, T^aT^b = T_F\delta^{ab}, \tag{1.4}$$

$$C_A = 3, \; C_F = \frac{4}{3}, \text{ and } \; T_F = \frac{1}{2}, \; d^{abc}d^{abc} = \frac{40}{3}, \tag{1.5}$$

where f^{abc} and d^{abc} are the structure constants.

Renormalization-group equation

We consider the scattering process $2 \to N-2$ particles

$$(p_1J_1;\lambda_1) + (p_2J_2;\lambda_2) \to (p_3J_3;\lambda_3) + \cdots + (p_NJ_N;\lambda_N) \tag{1.6}$$

where p_i, J_i, and λ_i are four momenta, spins, and helicities, respectively. The unpolarized total cross section is given by

$$\begin{aligned} \sigma &= \frac{1}{2\sqrt{(s-(m_1+m_2)^2)(s-(m_1-m_2)^2)}}\frac{1}{(2J_1+1)(2J_2+1)} \\ &\times \sum_{\lambda_1\cdots\lambda_N}\int\prod_{j=3}^{N}\frac{d^3p_j}{(2\pi)^3 2p_{j0}}(2\pi)^4\delta^4(\sum_{j=3}^{N}p_j - p_1 - p_2) \end{aligned}$$

$$\times \quad |\langle p_3\lambda_3, \cdots, p_N\lambda_N|T|p_1\lambda_1, p_2\lambda_2\rangle|^2, \quad s = (p_1+p_2)^2, \tag{1.7}$$

where we averaged over helicities of initial particles and summed helicities of final particles.

The transition matrix element $\langle p_3\lambda_3, \cdots, p_N\lambda_N|T|p_1\lambda_1, p_2\lambda_2\rangle$ in the above equation is related to N-point truncated connected Green function $G^{tc}_{\mu_1\cdots\mu_N} \equiv G^{tc}_N$ through

$$\begin{aligned} & \langle p_3\lambda_3, \cdots, p_N\lambda_N|T|p_1\lambda_1, p_2\lambda_2\rangle \\ = \quad & -i\,\bar{u}^{\mu_3}_{\lambda_3}(p_3)\cdots\bar{u}^{\mu_N}_{\lambda_N}(p_N)\,\tilde{G}^{tc}_{\mu_1\cdots\mu_N}(p_1, p_2, -p_3, \cdots, -p_N)\,u^{\mu_1}_{\lambda_1}(p_1)\,u^{\mu_2}_{\lambda_2}(p_2), \end{aligned} \tag{1.8}$$

where

$$\begin{aligned} & (2\pi)^4\delta^4(p_1+\cdots+p_N)\,\tilde{G}^{tc}_N(p_1, \cdots, p_N) \\ = \quad & \int d^4x_1\cdots d^4x_N\, e^{-i(p_1\cdot x_1+\cdots+p_N\cdot x_N)}G^{tc}_N(x_1, \cdots, x_N). \end{aligned} \tag{1.9}$$

Here, G^{tc}_N , truncated connected Green function, is derived from the following relation:

$$\begin{aligned} & (2\pi)^4\delta^4(p_1+\cdots+p_N)\,\tilde{G}_2(p_1)\cdots\tilde{G}_2(p_N)\,\tilde{G}^{tc}_N(p_1, \cdots, p_N) \\ = \quad & (2\pi)^4\delta^4(p_1+\cdots+p_N)\,\tilde{G}^{c}_N(p_1, \cdots, p_N) \\ = \quad & \int d^4x_1\cdots d^4x_N\, e^{-i(p_1\cdot x_1+\cdots+p_N\cdot x_N)}G^{c}_N(x_1, \cdots, x_N), \end{aligned} \tag{1.10}$$

where $\tilde{G}_2(p_i)$ are the 2-point connected Green functions and G^c_N is the connected Green function given by

$$G^c_N(x_1, \cdots, x_N) = \frac{(-i)^N}{Z[0]}\frac{\delta^N Z[J]}{\delta J(x_1)\cdots\delta J(x_n)}\bigg|_{J=0}. \tag{1.11}$$

$Z[J]$ is a functional integral of the Lagrangian density $L(x)$ [Eq.(1.1)]:

$$\begin{aligned} & Z[J_1, J_2, J_3, J_4, J_5] = \int [dA^a][dq_f][d\bar{q}_f][dc^a][dc^{a*}] \\ \times \quad & \exp\left\{i\int d^4x(L + A^a_\mu J^{a\mu}_1 + \bar{q}_f J_2 + J_3 q_f + c^{a*}J^a_4 + J^a_5 c^a)\right\}. \end{aligned} \tag{1.12}$$

We now redefine (so-called "renormalize") the fields A^a, q_f, and c^a by

$$A^a = Z_3^{1/2} A^a_{\rm R},\ q_f = Z_2^{1/2} q_{f\rm R},\ c^a = \tilde{Z}_3^{1/2} c^a_{\rm R}, \tag{1.13}$$

and the parameters g, m_f, and α_G by

$$g = Z_g g_r,\ m_f = Z_m m_{f\rm R},\ \alpha_G = Z_3 \alpha_{G\rm R}, \tag{1.14}$$

where Z_3, Z_2, and $\tilde{Z}_3$ are the gluon-field, quark-field, and ghost-field renormalization constants, while Z_g and Z_m are the coupling-constant and mass renormalization constants. Note that the gauge-fixing term in Eq.(1.1) is kept in the same form under the above redefinition.

Under the dimensional regularization, we introduce an energy scale μ to rewrite the gauge coupling strength g by

$$g = g_0 \mu_0^{\frac{4-D}{2}},\ \ g_r = g_{\rm R} \mu^{\frac{4-D}{2}}, \tag{1.15}$$

where g_0 and $g_{\rm R}$ are dimensionless gauge coupling strengths and D is the number of space-time dimensions introduced for the calculation of the Z_i renormalization constants. Here the energy scale μ_0 for "bare" coupling strength g is a fixed scale while the energy scale μ for the renormalized coupling strength g_r is a variable parameter.

On account of the renormalization (1.13), we find the renormalized truncated connected Green function $G^{tc}_{N\rm R}$ is related to G^{tc}_N by

$$\tilde{G}^{tc}_{N\rm R}(p_1, \ldots, p_N, g_r, m_{f\rm R}, \mu) = Z_3(\mu)^{n_G/2} Z_2(\mu)^{n_F/2} \tilde{G}^{tc}_N(p_1, \ldots, p_N, g, m_f), \tag{1.16}$$

where n_G and n_F are the numbers of gluon legs and quark legs, respectively (we do not consider Green function with ghost external lines).

Because the "bare" truncated connected Green function $\tilde{G}^{tc}_N$ is directly related to observables, therefore we impose a condition on $\tilde{G}^{tc}_N$ not to depend on the renormalization scale μ :

$$\begin{aligned} & \frac{d}{d\mu} \tilde{G}^{tc}_N(p_1, \ldots, p_N, g, m_f)\Big|_{g, m_f, \alpha_G} \\ = \ & \frac{d}{d\mu} \left[Z_3(\mu)^{-\frac{n_G}{2}} Z_2(\mu)^{-\frac{n_F}{2}} \tilde{G}^{tc}_{N\rm R}\left(p, g_{\rm R}(\mu, g, m_f), m_{f\rm R}(\mu, g, m_f), \mu\right) \right]\Big|_{g, m_f, \alpha_G} = 0, \end{aligned} \tag{1.17}$$

where the g, m_f, and α_G affixed to the above equation indicate that g, m_f, and α_G are kept fixed.

From this equation, we derive the renormalization-group equation:

$$\left[\mu^2\frac{\partial}{\partial\mu^2}+\beta(\alpha_{\rm s})\frac{\partial}{\partial\alpha_{\rm s}}+\beta_G(\alpha_{\rm s})\frac{\partial}{\partial\alpha_{G\rm R}}\right.$$
$$\left.-n_G\gamma_G(\alpha_{\rm s})-n_F\gamma_F(\alpha_{\rm s})-\gamma_m(\alpha_{\rm s})m_{f\rm R}\frac{\partial}{\partial m_{f\rm R}}\right]\tilde{G}^{tc}_{N\rm R}=0, \qquad (1.18)$$

with

$$\beta(\alpha_{\rm s})=\mu^2\frac{d\alpha_{\rm s}}{d\mu^2}, \qquad \beta_G(\alpha_{\rm s})=\mu^2\frac{d\alpha_{G\rm R}}{d\mu^2}=-2\alpha_{G\rm R}\gamma_G(\alpha_{\rm s}),$$
$$\gamma_m(\alpha_{\rm s})=-\frac{\mu^2}{m_{f\rm R}}\frac{dm_{f\rm R}}{d\mu^2}, \qquad \gamma_G(\alpha_{\rm s})=\frac{\mu^2}{2Z_3}\frac{dZ_3}{d\mu^2}, \quad \gamma_F(\alpha_{\rm s})=\frac{\mu^2}{2Z_3}\frac{dZ_3}{d\mu^2}, \qquad (1.19)$$

where $\alpha_{\rm s}(\mu)$ is the "strong coupling constant" defined as $g^2_{\rm R}(\mu)/4\pi$.

Running coupling constant $\alpha_{\rm s}(\mu)$

The μ dependence of the strong coupling constant $\alpha_{\rm s}(\mu)$ is given in the first equation of Eq.(1.19). The four-loop β-function has been calculated recently [7] as

$$\beta(\frac{\alpha_{\rm s}}{4\pi})=\frac{\mu^2 d}{d\mu^2}(\frac{\alpha_{\rm s}}{4\pi}) = -\beta_0(\frac{\alpha_{\rm s}}{4\pi})^2-\beta_1(\frac{\alpha_{\rm s}}{4\pi})^3-\beta_2(\frac{\alpha_{\rm s}}{4\pi})^4-\beta_3(\frac{\alpha_{\rm s}}{4\pi})^5+\mathcal{O}(\alpha_{\rm s}^6), \qquad (1.20)$$

with

$$\beta_0 = 11-\frac{2}{3}N_f, \qquad (1.21)$$
$$\beta_1 = 102-\frac{38}{3}N_f, \qquad (1.22)$$
$$\beta_2 = \frac{2857}{2}-\frac{5033}{18}N_f+\frac{325}{54}N_f^2, \qquad (1.23)$$
$$\beta_3 = \left(\frac{149753}{6}+3564\,\zeta_3\right)-\left(\frac{1078361}{162}+\frac{6508}{27}\zeta_3\right)N_f$$
$$+\left(\frac{50065}{162}+\frac{6472}{81}\zeta_3\right)N_f^2+\frac{1093}{729}N_f^3. \qquad (1.24)$$

Here N_f is the number of quark flavors with masses less than the energy scale μ and ζ is the Riemann zeta-function ($\zeta_3=\sum_{n=1}^{\infty}\frac{1}{n^3}=1.202056903\ldots$). The coefficients β_0 and β_1 are independent of the renormalization scheme while β_2 and higher order coefficients depend on the renormalization scheme. In all calculations, equations, and results refer to the 'Modified minimal subtraction scheme' ($\overline{\rm MS}$) [8].

The solution of Eq.(1.20) is often given as an expansion in inverse powers of $\ln(\mu^2)$:

$$\begin{aligned}\frac{\alpha_s(\mu)}{4\pi} &= \frac{1}{\beta_0 L} - \frac{b_1 \ln L}{(\beta_0 L)^2} + \frac{1}{(\beta_0 L)^3}\left[b_1^2\left[(\ln L)^2 - \ln L - 1\right] + b_2\right] \\ &+ \frac{1}{(\beta_0 L)^4}\left[b_1^3\left[-(\ln L)^3 + \frac{5}{2}(\ln L)^2 + 2\ln L - \frac{1}{2}\right] - 3b_1 b_2 \ln L + \frac{b_3}{2}\right] \\ &+ \mathcal{O}\left(\frac{(\ln L)^4}{L^5}\right), \end{aligned} \tag{1.25}$$

where $b_N = \beta_N/\beta_0$ $(N = 1,2,3)$, $L = \ln(\mu^2/\Lambda_{QCD}^2)$, and Λ_{QCD} is the so-called asymptotic scale parameter.

Figure 1.1 shows $\alpha_s(\mu_R)$ for $\alpha_s(M_Z) = 0.118$ summed in Eq.(1.25) to first, second, third, and fourth orders of L^{-1}. It also shows the solution of the beta function Eq.(1.20) exact up to $\mathcal{O}(\alpha_s^3)$, which satisfies the relation:

$$\frac{4\pi}{\alpha_s(\mu)} - b_1 \ln\left[\frac{4\pi}{\alpha_s(\mu)} + b_1\right] = \frac{4\pi}{\alpha_s(\lambda)} - b_1 \ln\left[\frac{4\pi}{\alpha_s(\lambda)} + b_1\right] + \beta_0 \ln\frac{\mu^2}{\lambda^2}. \tag{1.26}$$

Note that the above relation is exact and does not contain any cutoff parameters as in Eq.(1.20). As shown in the figure, the contributions from terms $\mathcal{O}(\alpha_s^4)$ and higher are negligibly small, and hence the solution of Eq.(1.26) is exact to $\sim 0.1\%$ in the energy range we consider. The solution of Eq.(1.26) shows "running" of the strong coupling constant.

1.2 Previous α_s measurements

1.2.1 α_s from e^+e^- collisions

α_s from R ratio

The hadronic production in electron-positron annihilation is usually characterized in terms of the R ratio – the total hadronic cross section normalized by the muon pair-production cross section,

$$R(s) \equiv \frac{\sigma_{tot}(e^+e^- \to \text{hadrons})}{\sigma(e^+e^- \to \mu^+\mu^-)} = 3\sum_f Q_f^2(1 + \delta_{QCD}), \tag{1.27}$$

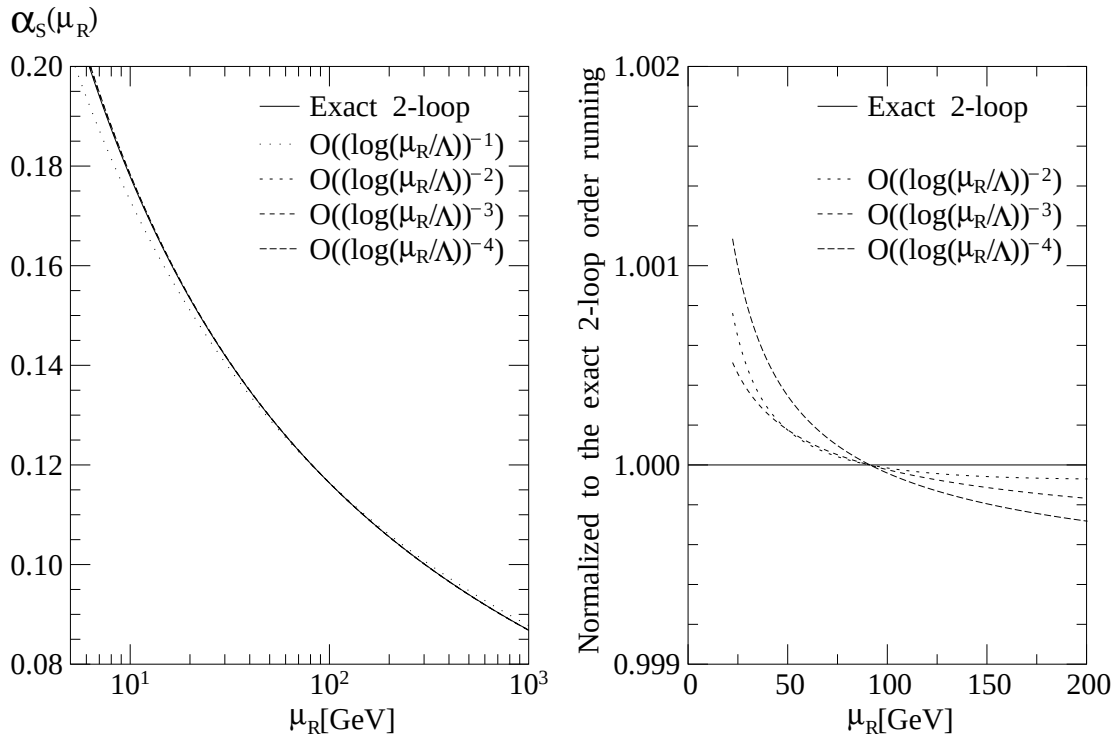

Figure 1.1: Comparison among $\alpha_{\rm s}(\mu_{\rm R})$'s summed to the first, second, third, and fourth orders in $\ln(\mu^2)^{-1}$ [see Eq.(1.25)]. The solid curve is the solution exact to $\mathcal{O}(\alpha_{\rm s}^3)$. $\alpha_{\rm s}(\mathrm{M_Z})$ is fixed to 0.118. The right plot shows the ratio normalized by the solid function. $\alpha_{\rm s}(\mu_{\rm R})$ to the first order is not shown; it reaches out of the range of this plot.

where s is the total center-of-mass energy squared, Q_f is the electric charge of the quark flavor f participating at the given energy, factor 3 stands for the number of color degrees of freedom, and δ_{QCD} stands for the strong interaction contributions. The $\alpha_{\rm s}$ measurement using R ratio values at various energies is given in Ref. [10]. The expression Eq.(1.27) is relevant at energies much less than the Z mass ($s \ll \mathrm{M_Z}$).

At LEP energy the effects of Z boson become important. The corresponding R ratio is defined as a ratio of the hadronic partial width to the electronic one of the Z boson,

$$R_Z \equiv \frac{,(Z \to \text{hadrons})}{,(Z \to e^+e^-)}. \tag{1.28}$$

The relation between R_Z and $\alpha_{\rm s}$ can be represented through a factorized effective formula as proposed in Ref. [11]. Its expression for $m_{Higgs} = 300$ GeV and $m_{top} = 180$ GeV is

$$R_Z = 19.943 \times \left[1 + 1.060\frac{\alpha_{\rm s}}{\pi} + 0.85(\frac{\alpha_{\rm s}}{\pi})^2 - 15(\frac{\alpha_{\rm s}}{\pi})^3\right]. \tag{1.29}$$

Using combined LEP R_Z value of $20.763 \pm 0.049(exp.)$ [9], Eq.(1.29) gives $\alpha_s(M_Z) = 0.120 \pm 0.007(exp.)$ [11].

α_s from τ decay

The quantity R_τ

$$R_\tau \equiv \frac{,(\tau^- \to \nu_\tau \text{hadrons})}{,(\tau^- \to \nu_\tau \bar{\nu}_e e^-)} \tag{1.30}$$

contains the information on the strong coupling constant in the same way as does R_Z.

In the Operator Product Expansion(OPE) [12] approach, the R_τ can be expressed as

$$R_\tau = 3(|V_{ud}|^2 + |V_{us}|^2) S_{EW}(1 + \delta_{EW} + \delta_{QCD} + \delta_m + \delta_{np}), \tag{1.31}$$

where V_{ud} and V_{us} are Kobayashi-Maskawa matrix elements, $|V_{ud}|^2 + |V_{us}|^2 = 0.998 \pm 0.002$. $S_{EW} \simeq 1.0194$ [13] and δ_{EW} are purely electroweak corrections, δ_{QCD} is the perturbative QCD correction [14], and δ_m is a correction for finite quark masses. The non-perturbative corrections are contained in δ_{np}.

R_τ is obtained by measuring the leptonic branching ratios from the relation $R_\tau = (1 - B_e - B_\mu)/B_e$, where B_e and B_μ are the branching ratios $,(\tau^- \to \nu_\tau \bar{\nu}_e e^-)/,(\tau^- \to \text{all})$ and $,(\tau^- \to \nu_\tau \bar{\nu}_\mu \mu^-)/,(\tau^- \to \text{all})$, respectively. From a direct B_e measurement, $R_\tau = 3.605 \pm 0.064$. An independent measurement of the tau lifetime yields $R_\tau = 3.682 \pm 0.048$ using $B_e = (\tau_\tau/\tau_\mu)(m_\tau/m_\mu)^5$.

Combining the two results, we obtain $R_\tau = 3.654 \pm 0.038$ [9]. Using the OPE with the non-perturbative coefficients found in Ref.[15], we obtain

$$\alpha_s(M_Z) = 0.1229^{+0.0016+0.0025}_{-0.0017-0.0021}. \tag{1.32}$$

The first uncertainty is the combined experimental uncertainty and the second is due to unknown higher orders and uncertainties in the non-perturbative contributions.

α_s from J/ψ decay

In Non-Relativistic Quantum Chromodynamics (NRQCD) [16], partial decay widths of J/ψ and η_c can be expressed as

$$
\begin{aligned}
,(\eta_c \to \gamma\gamma) &= \frac{256\pi\alpha^2}{27M_{\eta_c}^2}|\overline{R_{\eta_c}}|^2\left[1-3.4\frac{\alpha_s}{\pi}-\frac{r}{3}\right], && (1.33)\\
,(\eta_c \to gg) &= \frac{32\pi\alpha_s^2}{3M_{\eta_c}^2}|\overline{R_{\eta_c}}|^2\left[1+4.8\frac{\alpha_s}{\pi}-\frac{r}{3}\right], && (1.34)\\
,(J/\psi \to \gamma e^+e^-) &= \frac{64\pi\alpha^2(M_{J/\psi})}{9M_{J/\psi}^2}|\overline{R_{J/\psi}}|^2\left[1-\frac{16\alpha_s}{3\pi}-\frac{r}{3}\right], && (1.35)\\
,(J/\psi \to ggg) &= \frac{160\alpha_s^3(\pi^2-9)}{81M_{J/\psi}^2}|\overline{R_{J/\psi}}|^2\left[1-3.7\frac{\alpha_s}{\pi}-4.32\,r\right], && (1.36)
\end{aligned}
$$

where R_{η_c} and $R_{J/\psi}$ are radial wavefunctions and

$$
r = -\frac{4}{m_c^2|\overline{R_S}|^2}Re(\overline{R_S} * \cdot\overline{\nabla^2 R_S}), \qquad (1.37)
$$

where $R_S = (R_{\eta_c} + 3R_{J/\psi})/4$ and m_c is the mass of c-quark.

For a fit to Eqs. (1.33)-(1.36), we use the following measured decay widths [17]:

$$
\begin{aligned}
,(\eta_c \to \gamma\gamma) &= 8.1 \pm 2.0 \text{ keV}, && (1.38)\\
,(\eta_c \to gg) &= 10.3 \pm 3.6 \text{ MeV}, && (1.39)\\
,(J/\psi \to e^+e^-) &= 5.36 \pm 0.28 \text{ keV}, && (1.40)\\
,(J/\psi \to ggg) &= 54.1 \pm 5.4 \text{ keV}. && (1.41)
\end{aligned}
$$

By introducing a "effective gluon mass" M_g (0.66 ± 0.08 GeV, obtained from $J/\psi \to \gamma + X$ processes [18]) which corrects for the contribution of the non-perturbative structure of the QCD ground state, the four parameter fit of Eqs. (1.33)-(1.36) to the above decay widths leads to

$$
\alpha_s(m_c) = 0.302 \pm 0.008^{+0.038}_{-0.050}, \qquad (1.42)
$$

where the first uncertainty is purely experimental and the second takes into account the uncertainties due to r, M_g and the uncalculated $O(\alpha_s)$ corrections.

α_s from Υ decay

The partial decay widths of Υ can be expressed as

$$
\begin{aligned}
,(\Upsilon \to e^+e^-) &= \frac{16\pi\alpha^2(M_\Upsilon)}{9M_\Upsilon^2}|\overline{R_\Upsilon}|^2\left[1-\frac{16\alpha_s}{3\pi}-\frac{r}{3}\right], && (1.43)\\
,(\Upsilon \to ggg) &= \frac{160\alpha_s^3(\pi^2-9)}{81M_\Upsilon^2}|\overline{R_\Upsilon}|^2\left[1-4.9\frac{\alpha_s}{\pi}-4.32\,r\right], && (1.44)\\
,(\Upsilon \to \gamma gg) &= \frac{160\alpha_s^2\alpha(\pi^2-9)}{81M_\Upsilon^2}|\overline{R_\Upsilon}|^2\left[1-7.4\frac{\alpha_s}{\pi}-4.32\,r\right]. && (1.45)
\end{aligned}
$$

To perform a fit to Eqs. (1.43)-(1.45), we use the following measured decay widths [17]:

$$
\begin{aligned}
,(\Upsilon \to e^+e^-) &= 1.34 \pm 0.04 \text{ keV}, && (1.46)\\
,(\Upsilon \to ggg) &= 43.7 \pm 1.7 \text{ keV}, && (1.47)\\
,(\Upsilon \to \gamma gg) &= 1.28 \pm 0.10 \text{ keV}. && (1.48)
\end{aligned}
$$

With the "effective gluon mass" of $M_g = 1.17 \pm 0.08$ GeV the fit leads to

$$\alpha_s(m_b) = 0.200 \pm 0.002(exp.)^{+0.010}_{-0.006}(theor.). \qquad (1.49)$$

α_s from hadronic event observables in e^+e^- collision

Various observables have been introduced to characterize event shapes in the process $e^+e^- \to$ hadrons. These include six event shape variables 1) – 6), differential 2-jet rates D_2 defined by six different jet resolution/recombination schemes 7) – 12), two particle energy-energy correlations 13) – 14), and a jet cone energy fraction 15) as described below.

The six event shape variables 1) – 6) are:

1) Thrust (T) [1]

[1] Thrust T is defined by

$$T \equiv \max \frac{\sum_i |\vec{p_i}\cdot\vec{n}_T|}{\sum_i |\vec{p_i}|}, \qquad (1.50)$$

where $\vec{p_i}$ is the momentum vector of particle i, and $\vec{n}_T$ is the thrust axis to be determined. For back-to-back two parton final states T is one, while for planer three parton final states $2/3 < T < 1$. Spherical events have $T = 1/2$.

2) Scaled heavy jet mass (ρ) [2]

3), 4) Total jet broadening ($B_{\rm T}$) and wide jet broadening ($B_{\rm W}$) [3]

5) Oblateness (O) [5]

6) C-parameter (C) [6]

Jets are reconstructed using iterative clustering algorithms in which a measure y_{ij} is calculated for all pairs of particles i and j, and the pair with the smallest y_{ij} is

---

[2]Events can be divided into two hemispheres, a and b, by a plane perpendicular to the thrust axis $\vec{n}_{\rm T}$. The heavy jet mass M_H is then defined as

$$M_H = \max(M_a, M_b), \tag{1.51}$$

where M_a and M_b are invariant masses of the two hemispheres. Here, the normalized quantity, ρ is defined by

$$\rho \equiv \frac{M_H^2}{E_{vis}^2}, \tag{1.52}$$

where E_{vis} is the total visible energy measured in hadronic events.

[3]In each hemisphere a, b,

$$B_{a,b} = \frac{\sum_{i\in a,b} |\vec{p_i} \times \vec{n}_{\rm T}|}{2\sum_i |\vec{p_i}|} \tag{1.53}$$

is calculated. The $B_{\rm T}$ and $B_{\rm W}$ are defined by

$$B_{\rm T} \equiv B_a + B_b \ \text{ and } \ B_{\rm W} \equiv \max(B_a, B_b), \tag{1.54}$$

respectively. Both $B_{\rm T}$ and $B_{\rm W}$ are identically zero in two parton final states and are sensitive to the transverse structure of jets.

[5]$\vec{n}_{maj}$ is an axis transverse to $\vec{n}_{\rm T}$ can be determined to maximize the momentum sum by replacing $\vec{n}_{\rm T}$ in Eq.(1.50) by one. An axis $\vec{n}_{min}$ is defined to be perpendicular to the two axes $\vec{n}_{\rm T}$ and $\vec{n}_{maj}$. The oblateness O is then defined by

$$O \equiv T_{maj} - T_{min}, \tag{1.55}$$

where the thrust major T_{maj} and thrust minor T_{min} are obtained by replacing $\vec{n}_{\rm T}$ in Eq.(1.50) by $\vec{n}_{maj}$ or $\vec{n}_{min}$, respectively.

[6]The C parameter is derived from the eigenvalues of the momentum tensor:

$$\theta_{\rho\sigma} \equiv \frac{\sum_i p_i^\rho p_i^\sigma / |\vec{p_i}|}{\sum_i |\vec{p_i}|}, \tag{1.56}$$

where p_i^ρ is the ρ-th component of the three momentum of particle i, and i runs over all the final state particles. The tensor $\theta_{\rho\sigma}$ is normalized to have unit trace, and the C parameter is defined by

$$C \equiv 3(\lambda_1\lambda_2 + \lambda_2\lambda_3 + \lambda_3\lambda_1), \tag{1.57}$$

where λ_i $(i = 1, 2, 3)$ are the eigenvalues of the tensor $\theta_{\rho\sigma}$. For back-to-back two parton final states C is zero, while for planer three parton final states $0 < C < 2/3$. For spherical events $C = 1$.

combined into a single particle k. This procedure is repeated until all pairs have y_{ij} exceeding a value y_{cut}, and the jet multiplicity of the event is defined as the number of particles remaining. The n-jet rate $R_n(y_{cut})$ is the fraction of events classified as n-jet. The differential two jet rate $D_2(y_{cut})$ is defined as

$$D_2(y_{cut}) \equiv \frac{R_2(y_{cut}) - R_2(y_{cut} - \Delta y_{cut})}{\Delta y_{cut}}. \tag{1.58}$$

Several schemes have been proposed comprising different y_{ij} definitions and recombination procedures. They applied the $E, E0, P$, and $P0$ variations of the JADE algorithm [19] as well as the Durham (D) and Geneva (G) schemes. The six definitions of the jet resolution parameter y_{ij} and recombination procedures are:

7) E scheme [7]

8) $E0$ scheme [8]

9) P scheme [9]

10) $P0$ scheme [10]

---

[7] In the E scheme y_{ij} is defined as the square of the invariant mass of the pair of particles i and j scaled by visible energy in the event,

$$y_{ij} \equiv \frac{(p_i + p_j)^2}{E_{vis}^2}, \tag{1.59}$$

with the recombination performed as

$$p_k = p_i + p_j, \tag{1.60}$$

where p_i and p_j are the four-momenta of the particles, and pion masses are assumed in calculating particle energies. Energy and momentum are explicitly conserved in this scheme.

[8] In the $E0$ scheme y_{ij} is defined by Eq.(1.59), while the recombination is defined by

$$E_k = E_i + E_j, \;\; \vec{p_k} \equiv \frac{E_k}{|\vec{p_i} + \vec{p_j}|}(\vec{p_i} + \vec{p_j}), \tag{1.61}$$

where E_i and E_j are energies and $\vec{p_k}$ and $\vec{p_j}$ are the three-momenta of the particles. In this scheme the three-momentum $\vec{p_k}$ is rescaled so that particle k has zero invariant mass.

[9] In the P scheme y_{ij} is defined by Eq.(1.59), while the recombination is defined by

$$\vec{p_k} = \vec{p_i} + \vec{p_j}, \;\; E_k = |\vec{p_k}|. \tag{1.62}$$

This scheme conserves the total momentum of an event, but does not conserve the total energy.

[10] The $P0$ scheme is similar to the P scheme, but the total energy E_{vis} in Eq.(1.59) is recalculated at each iteration according to

$$E_{vis} \equiv \sum_k E_k. \tag{1.63}$$

11) Durham (D) scheme [11]

12) Geneva (G) scheme [12]

The other hadronic observables are:

13) Energy-energy correlations (EEC) [13]

14) Asymmetry of the EEC (AEEC) [14]

15) Jet cone energy fraction (JCEF) [15]

---

[11] In the D scheme y_{ij} is defined by

$$y_{ij} \equiv \frac{2\min(E_i^2, E_j^2)(1-\cos\theta_{ij})}{E_{vis}^2}, \tag{1.64}$$

where θ_{ij} is the angle between the pair of particles i and j. The recombination is defined by Eq.(1.60). With the D scheme a soft particle will be combined with another soft particle, instead of being combined with high-energy particle, only if the angle it makes with the other soft particle is smaller than the angle that it makes with the high-energy particle.

[12] The definition of y_{ij} for the G scheme is

$$y_{ij} \equiv \frac{8E_iE_j(1-\cos\theta_{ij})}{9(E_i+E_j)^2}, \tag{1.65}$$

and the recombination is defined by Eq.(1.60). In this scheme y_{ij} depends only on the energy of the particles to be combined, and not on E_{vis} of the event.

[13] The energy-energy correlations (EEC) is the normalized energy-weighted cross section defined in terms of the angle χ_{ij} between two particles i and j in an event:

$$\mathrm{EEC}(\chi) \equiv \frac{1}{N_{events}\Delta\chi}\sum_{events}\int_{\chi-\Delta\chi/2}^{\chi+\Delta\chi/2}\sum_{ij}\frac{E_iE_j}{E_{vis}^2}\delta(\chi'-\chi_{ij})d\chi', \tag{1.66}$$

where χ is an opening angle to be studied for the correlations; $\Delta\chi$ is the angular bin width; and E_i and E_j are the energies of particles i and j. The angle is taken from $\chi = 0°$ to $180°$.

[14] The asymmetry of the EEC (AEEC) is defined as

$$\mathrm{AEEC}(\chi) \equiv \mathrm{EEC}(180° - \chi) - \mathrm{EEC}(\chi). \tag{1.67}$$

[15] The cone energy fraction (JCEF) is defined as

$$\mathrm{JCEF}(\chi) \equiv \frac{1}{N_{events}\Delta\chi}\sum_{events}\int_{\chi-\Delta\chi/2}^{\chi+\Delta\chi/2}\sum_{i}\frac{E_i}{E_{vis}}\delta(\chi'-\chi_i)d\chi', \tag{1.68}$$

where

$$\chi' \equiv \arccos\left(\frac{\vec{p_i}\cdot\vec{n}_{\mathrm{T}}}{|\vec{p_i}|}\right) \tag{1.69}$$

is the opening angle between a particle and the thrust axis vector, $\vec{n}_{\mathrm{T}}$, whose direction is defined to point from the heavy jet mass hemisphere to the light jet mass hemisphere, and $0° \leq \chi \leq 180°$.

The QCD predictions up to $O(\alpha_s^2)$ for all observables defined as above have the general form

$$\frac{1}{\sigma_t}\frac{d\sigma(y)}{dy} = A(y)\frac{\alpha_s}{2\pi} + [B(y) + A(y)\beta_0 \ln f]\,(\frac{\alpha_s}{2\pi})^2, \tag{1.70}$$

where y is the observable in question; σ_t is the total hadronic cross section; $f = \mu/\sqrt{s}$; $\beta_0 = (11 - \frac{2}{3}N_f)$; and N_f is the number of active quark flavors; $N_f = 5$ at $\sqrt{s} = \mathrm{M_Z}$.

The strong coupling α_s can be derived by fitting the $O(\alpha_s^2)$ QCD calculations of $A(y)$ and $B(y)$ to the measured distributions. They applied bin-by-bin correction factors to the experimental distribution to account for detector effects and hadronization. Each corrected distribution was fitted by minimizing χ^2 with f range such that $\chi^2_{dof} < 5$ and $f \leq 4$. For each observable the central value of α_s was defined as the midpoint between the extrema in this f range, and the scale uncertainty was defined as the difference between the central value and the extrema. They combined the results from all fifteen observables using an unweighted average of α_s values, experimental systematic, and theoretical uncertainties to obtain [20]:

$$\alpha_s(\mathrm{M_Z}) = 0.1226 \pm 0.0026(exp.) \pm 0.0109(theor.). \tag{1.71}$$

The theoretical uncertainty is dominated by the scale ambiguity (± 0.0106).

They also determined α_s by comparing matched resummed+$O(\alpha_s^2)$ calculations with data. These calculations, which combined a resummation [21] of the leading and next-to-leading logarithmic terms to all orders in α_s with the second order calculations using an exponentiation technique, have been performed for T, ρ, B_T, B_W, D_2 (D scheme), and EEC. They applied the same analysis as for $O(\alpha_s^2)$ calculations to each combination out of four matching schemes and six observables [20]. By averaging over the six α_s values they obtained

$$\alpha_s(\mathrm{M_Z}) = 0.1192 \pm 0.0025(exp.) \pm 0.0070(theor.), \tag{1.72}$$

where the theoretical uncertainty is the sum in quadrature of the hadronization (± 0.0016) and scale and matching ambiguity (± 0.0065). This uncertainty, which

reflects missing higher order terms in the calculations, is reduced by a factor 1.5 relative to the $O(\alpha_s^2)$ analysis.

They combined the results from the $O(\alpha_s^2)$ and resummed+$O(\alpha_s^2)$ calculations by taking an unweighted average of the α_s values and experimental and theoretical uncertainties, obtaining [20]:

$$\alpha_s(\mathrm{M_Z}) = 0.1200 \pm 0.0025(exp.) \pm 0.0078(theor.). \tag{1.73}$$

Recently, L3 collaboration at LEP performed an α_s measurement at the center of mass energies of 133, 161, and 172 GeV using four event shape variables – T, ρ, B_T, and B_W. The combined results [22] are

$$\alpha_s(\mathrm{M_Z}) = 0.122 \pm 0.002(exp.) \pm 0.007(theor.), \tag{1.74}$$

$$\alpha_s(133\ \mathrm{GeV}) = 0.107 \pm 0.005(exp.) \pm 0.006(theor.), \tag{1.75}$$

$$\alpha_s(161\ \mathrm{GeV}) = 0.103 \pm 0.005(exp.) \pm 0.005(theor.), \tag{1.76}$$

$$\alpha_s(172\ \mathrm{GeV}) = 0.104 \pm 0.006(exp.) \pm 0.005(theor.). \tag{1.77}$$

The value of $\alpha_s(\mathrm{M_Z})$ is derived from a study in hadronic Z decays at $\sqrt{s} = \mathrm{M_Z}$ using the same analysis.

1.2.2 α_s from lepton-hadron collisions

A deeply inelastic lepton-hadron scattering(DIS) process is in general represented by

$$l(k) + h(p) \rightarrow l'(k') + X, \tag{1.78}$$

where $l(k)$ represents an incoming lepton with momentum k^μ, $h(p)$ a hadron with momentum p^μ, $l'(k')$ an outgoing lepton with momentum k'^μ, and X an arbitrary hadronic state.

In DIS, the momentum transfer between lepton and hadron, q, is spacelike,

$$q^\mu = k^\mu - k'^\mu, \quad -q^2 = Q^2. \tag{1.79}$$

This is normally parameterized in terms of the "Bjorken scaling variable" x,

$$x = \frac{-q^2}{2p \cdot q} = \frac{Q^2}{2m_h \nu}, \tag{1.80}$$

where m_h is a mass of the hadron and ν is the energy transferred from the lepton to the hadron in the hadron (target) rest frame,

$$\nu = \frac{p \cdot q}{m_h} = E_k - E_{k'}. \tag{1.81}$$

ν is naturally related to the dimensionless variable y,

$$y = \frac{p \cdot q}{p \cdot k} = \frac{E_k - E_{k'}}{E_k}, \tag{1.82}$$

which measures the ratio of the energy transferred to the hadronic system to the total leptonic energy available in the target rest frame.

The incoming lepton may be an electron, a muon, or an (anti)neutrino, and the exchanged vector boson: a photon, $W^{\pm}$, or Z^0. At lowest order in the electroweak interactions, the cross section may be split into leptonic and hadronic parts,

$$d\sigma = \frac{d^3k'}{2s|\vec{k'}|} \frac{c_V^4}{4\pi^2(q^2 - m_V^2)^2} L_{lV}^{\mu\nu}(k,q) W_{\mu\nu}^{Vh}(p,q), \tag{1.83}$$

where V labels the exchanged vector boson, with a mass m_V and c_V is the electroweak interaction coupling strength.

The hadronic tensor $W_{\mu\nu}^{Vh}$ can be expanded in terms of "scalar structure functions" W_i^{Vh} :

$$\begin{aligned} W_{\mu\nu}^{Vh} &= -\left[g_{\mu\nu} - \frac{q_\mu q_\nu}{q^2}\right] W_1^{Vh}(x,Q^2) \\ &\quad + \left[p_\mu - q_\mu \frac{p \cdot q}{q^2}\right]\left[p_\nu - q_\nu \frac{p \cdot q}{q^2}\right] \frac{1}{m_h^2} W_2^{Vh}(x,Q^2) \\ &\quad - i\epsilon_{\mu\nu\lambda\sigma} p^\lambda q^\sigma \frac{1}{m_h^2} W_3^{Vh}(x,Q^2). \end{aligned} \tag{1.84}$$

The structure functions are generally parameterized in terms of x and Q^2. Note that for photon exchange only parity invariance of strong interactions implies

$$W_3^{\gamma h}(x,Q^2) = 0. \tag{1.85}$$

The functions W_i in Eq.(1.84) are usually replaced by F_i as follows:

$$\begin{aligned} F_1(x,Q^2) &= W_1(x,Q^2), \\ F_2(x,Q^2) &= \frac{\nu}{m_h} W_2(x,Q^2), \\ F_3(x,Q^2) &= \frac{\nu}{m_h} W_3(x,Q^2). \end{aligned} \tag{1.86}$$

α_s from e-p collision

α_s is determined from the proton structure function $F_2^p(x,Q^2)$ at small x and $Q^2 < 100$ GeV^2. F_2^p is computed in next-to-leading order in α_s, including summations of all leading and subleading logarithms of Q^2 and $1/x$. In that study it is demonstrated that the structure function data of H1 and ZEUS exhibit double logarithmic scaling in both x and Q^2, which is regarded as the direct evidence for the running α_s [23]. A QCD fit to these data yields $\alpha_s(\mathrm{M_Z}) = 0.120 \pm 0.005(exp.) \pm 0.009(theor.)$.

α_s from GLS sum rule

The Gross-Llewellyn Smith (GLS) sum rule is

$$GLS = \int_0^1 dx F_3^{\bar{\nu}p+\nu p} \approx 3. \tag{1.87}$$

The deviation from the number of valence quarks, 3, is the QCD corrections calculated to NNLO. The best measurement is performed by the CCFR collaboration [24] in νN collisions, which gives

$$\alpha_s(\mathrm{M_Z}) = 0.119 \pm 0.002(exp.) \pm 0.004(theor.). \tag{1.88}$$

1.2.3 α_s from hadron-hadron collisions

α_s from $\bar{b}b$ production in $\bar{p}p$ collisions

The comparison of the $\bar{b}b$ production cross section for 2-body final states with NLO QCD prediction yields

$$\alpha_s(\mathrm{M_Z}) = 0.113^{+0.007}_{-0.006}(exp.)^{+0.008}_{-0.009}(theor.), \tag{1.89}$$

where the energy scale μ was varied in $\mu_0/4 < \mu < \mu_0$ for $\mu_0 = \sqrt{(k \times m_b)^2 + p_{\rm T}^2}$ with the uncertainty factor of $k = 1.0^{+0.50}_{-0.33}$ [25]. Three-body final states were excluded since the final results depends strongly on the choice of the energy scale.

$\alpha_{\rm s}$ from photon production in $\bar{p}p$ and pp collisions

From the difference of cross sections $\sigma(\bar{p}p \to \gamma X) - \sigma(pp \to \gamma X)$, $\alpha_{\rm s}$ is measured to be

$$\alpha_{\rm s}({\rm M_Z}) = 0.112 \pm 0.006(stat.) \pm 0.005(syst.)^{+0.009}_{-0.001}(theor.), \qquad (1.90)$$

where the theoretical error is quoted for a variation of the scales from $p_{\rm T}^2/8$ to $3p_{\rm T}^2/4$. The central value of $\alpha_{\rm s}({\rm M_Z})$ that describes the data of Ref. [26] is then taken to be that characterizing the theoretical prediction which yields the minimum χ^2.

$\alpha_{\rm s}$ from W production in $\bar{p}p$ collisions

By measuring of the ratio of the production rate of W events with one jet to that with no jets, $\alpha_{\rm s}$ is extracted to second order in the $\overline{\rm MS}$ scheme: $\alpha_{\rm s}(M_W) = 0.123 \pm 0.018(stat.) \pm 0.017(syst.)$ [27].

1.3 Outline of the Thesis

This thesis describes the measurement of the strong coupling constant $\alpha_{\rm s}$ which we obtained from two jet production cross sections. Chapter 2 describes the Tevatron accelerator and the Collider Detector at Fermilab (CDF), the apparatus we performed the present measurement. In Chapter 3 we describe the jet reconstruction, two jet event selection, and the results of the two jet production cross sections. The cross sections are unsmeared to correct the distorted distributions due to finite detector performance so that the obtained distributions can be compared directly with the theoretical expectations. The measured results of the $\alpha_{\rm s}$ are given in Chapter 4. Chapter 5 concludes the present measurements.

Chapter 2

Apparatus

With the Collider Detector at Fermilab (CDF) we studied 1.8 TeV proton-antiproton collisions at the Fermi National Accelerator Laboratory (Fermilab) in Batavia, Illinois, U.S.A. In this chapter we describe the Tevatron accelerator and the CDF detector.

2.1 Tevatron

The Tevatron accelerator has provided the highest energy protons (900 GeV) and antiprotons (900 GeV) colliding at a center-of-mass energy of 1.8 TeV since 1985. The Tevatron accelerator collider complex consists of five stages of accelerators as illustrated in Fig. 2.1. By the Cockcroft-Walton electrostatic accelerator (C-W), negatively charged hydrogen ions are accelerated to 750 keV. After leaving the C-W, the H^- ions are accelerated to 400 MeV in the 500 feet long linear accelerator (LINAC). Then the H^- ions pass through a carbon foil where two electrons are stripped off, leaving only the bare protons, which are injected into the booster ring. The booster is a synchrotron of 500 feet in diameter, which accelerates the protons up to 8 GeV. The Main Ring, a synchrotron with a diameter of two kilometers, is composed of about 1000 water-cooled conventional copper-coiled magnets. After being accelerated to 150 GeV in the Main Ring, the protons are injected to the Tevatron ring which is housed in the same tunnel as for the Main Ring. The Tevatron ring is composed of superconducting magnets and can accelerate protons to 900 GeV.

To produce antiprotons, protons are first accelerated to an energy of 120 GeV in the Main Ring, extracted, transported, and focused on the tungsten target. Of the many particles and antiparticles of different types produced in collisions which the protons make in the target, about ten million antiprotons are collected in a debuncher ring. The captured beam of antiprotons is then reduced in size by a process known as stochastic cooling while circulating in the debuncher ring. The antiprotons are then transferred to the accumulator ring where the antiprotons merged into a single beam, cooled further and stored. The debuncher and accumulator rings operate at 8 GeV. When a sufficient number of antiprotons has been produced, the antiprotons are re-injected to the Main Ring accelerated up to 150 GeV, and passed down into the Tevatron ring. In the Tevatron ring the antiprotons are accelerated from 150 GeV to 900 GeV simultaneously with a counterrotating beam of protons.

Some of the Tevatron parameters relevant to the luminosity are given below:

		Parameter	Typical value
N_p	:	number of protons per bunch	1-2 $\times 10^{11}$
$N_{\bar{p}}$	:	number of antiprotons per bunch	4-7 $\times 10^{10}$
f	:	revolution frequency (kHz)	50
B	:	number of bunches	6
ϵ	:	emittance (mm mrad)	2.6×10^{-3}
β	:	betatron oscillation length (m)	0.5

From these parameters the luminosity $\mathcal{L}$ can be calculated by

$$\mathcal{L} = \frac{N_p \, N_{\bar{p}} \, f \, B}{4\pi \, \epsilon \, \beta} \tag{2.1}$$

Protons and antiprotons are accelerated in 6 bunches each, as listed above, making collisions at every 3.5 μsec. The transverse profile of the Tevatron beam is circular and has an rms spread of $\sim 35\,\mu$m.

The 1994-95 run (RUN-Ib) started in November 1993 and ended in July 1995. The Tevatron provided a peak instantaneous luminosity of $\mathcal{L} \sim 2.5 \times 10^{31}\,\mathrm{cm}^{-2}\mathrm{s}^{-1}$, and the CDF has collected an integrated luminosity of $\int \mathcal{L}\, dt = 86\,\mathrm{pb}^{-1}$ during this period.

Once the luminosity is given, the events with a cross section of σ are produced in proton-antiproton collisions at a rate of N :

$$N = \mathcal{L} \cdot \sigma. \tag{2.2}$$

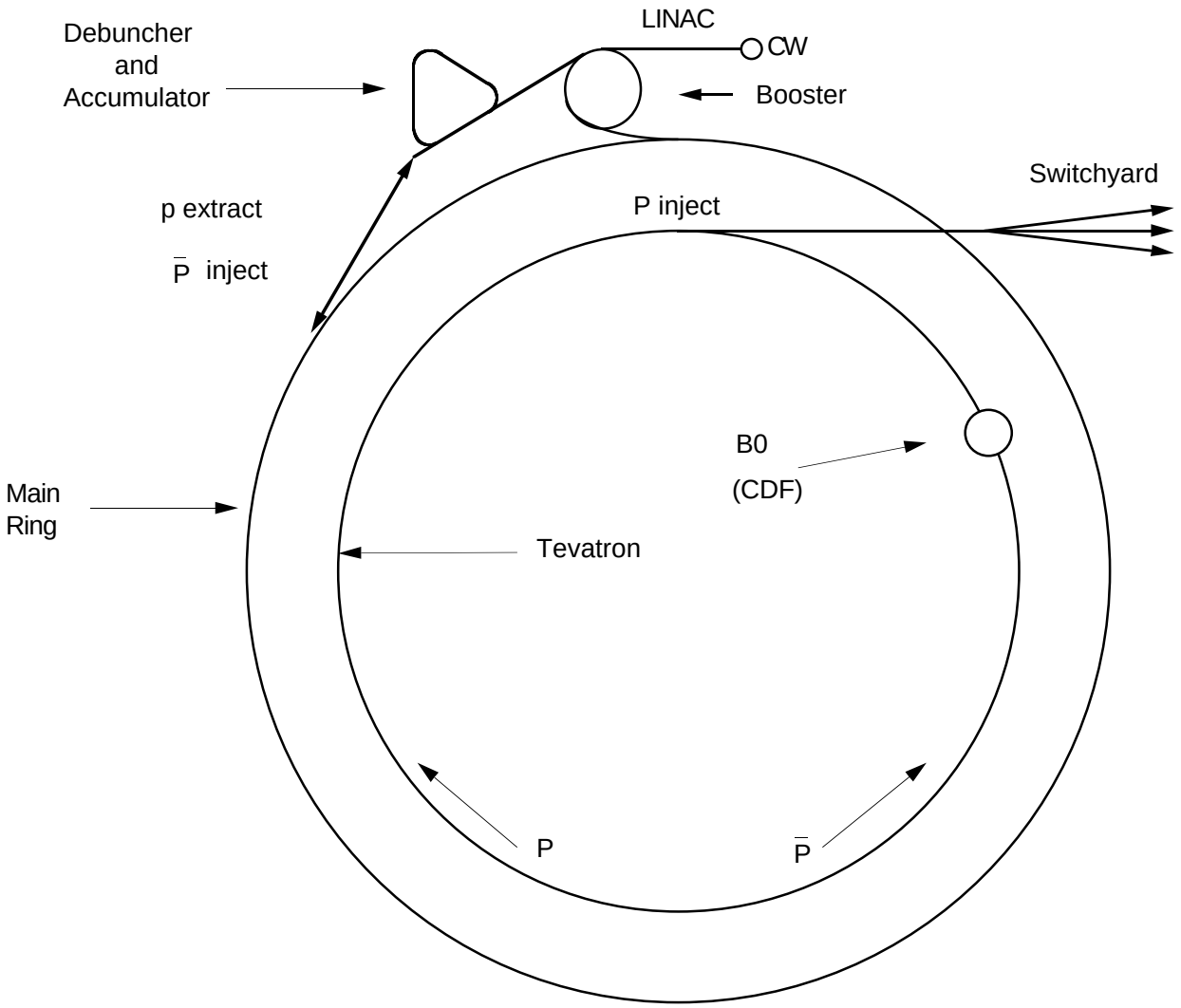

Figure 2.1: Diagram of the Tevatron accelerator complex at Fermilab.

2.2 Collider Detector at Fermilab

The Collider Detector at Fermilab (CDF) is a general purpose detector located at the B0 interaction region of the Tevatron ring. A perspective view of the CDF detector is shown in Fig. 2.2. The detector is divided into three parts with different coverage in the polar angle θ: the central detector ($10^\circ < \theta < 170^\circ$), the forward detector ($\theta < 10^\circ$), and the backward detector ($\theta > 170^\circ$), respectively.

Figure 2.3 shows the central and forward detectors where the location of each detector component is indicated. The superconducting solenoidal magnet which is 4.8 m long and 1.5 m in radius generates a uniform magnetic field of 1.4 T along the z axis. Inside, a system of tracking chambers is equipped to measure the momentum and sign of charged particles. The tracking system consists of a silicon microstrip vertex detector (SVX), a vertex drift chamber (VTX), and a central tracking drift chamber (CTC). The solenoid and tracking volume is surrounded by calorimeters which measure the electromagnetic and hadronic energy of jets and electrons/photons. The calorimeters are separated in three regions in pseudorapidity η, the central, end-plug, and forward regions. Each region consists of electromagnetic and hadronic parts. Outside the calorimeters, there are sets of drift chambers to detect the trajectory of muons, the central muon detection system (CMU), the central muon upgrade (CMP), the central muon extension (CMX), and the forward muon system (FMU). The beam-beam counters (BBC) consisting of scintillation counters are located in front of the forward and backward electromagnetic calorimeters for luminosity monitor and trigger.

CDF uses a conventional right-handed coordinate system with x out of the Tevatron ring in the horizontal plane, y vertically upward, and z in the proton direction. The pseudorapidity η is defined as $\eta \equiv -\ln[\tan(\theta/2)]$, where the polar angle θ is measured from the proton direction. The azimuthal angle ϕ is an angle in x-y plane measured from the positive x-axis toward the positive y-axis. The radius r is the radial distance from the beam in x-y plane.

2.2.1 Tracking detectors

Silicon microstrip vertex detector (SVX) [28]

The silicon microstrip vertex detector (SVX) is designed to detect the decay vertex of long lifetime particles containing heavy flavors. The SVX consists of two cylindrical barrel modules placed end-to-end with their axes coincident with the beamline. The total longitudinal coverage in z is 51 cm (2×25.5 cm with a 2.15 cm gap). Because $\bar{p}p$ interactions spread along the beamline with a standard deviation $\sigma \sim 30$ cm, the geometrical acceptance of the SVX is about 60% for $\bar{p}p$ interactions.

Each barrel consists of four concentric cylindrical (twelve sided barrel, to be exact) layers of DC-coupled silicon microstrips. Surrounding the 1.9 cm radius beryllium beam pipe, the SVX layers are located at 2.846, 4.256, 5.687, and 7.866 cm from the beam line. The silicon detectors are 300 μm thick with 8.5 cm long microstrips along the beam line. The strip pitches are 60 μm for the inner three layers and 55 μm for the fourth layer. The SVX single-track impact parameter resolution is measured in data to be $(13 + 40/p_{\mathrm{T}})\mu$m in the r-ϕ plane, where p_{T} has units of GeV/c.

The charged tracks are primarily reconstructed by the CTC. All tracks reconstructed only with CTC are extrapolated to each SVX layers. If at least 2 hits are found out of the four SVX layers, the track parameters are re-calculated using both CTC and SVX information. The impact parameter resolution at high momentum ($p_{\mathrm{T}} \geq 10$ GeV) is measured in data to be $\sigma = 17\,\mu$m.

Vertex drift chamber (VTX) [29]

The vertex drift chamber (VTX), surrounding the SVX, is designed primarily to determine the event vertex position in the z direction. After the 1988-89 CDF collider run, the VTX was installed replacing the vertex time projection chamber (VTPC) [30]. Most of the characteristics of the modules of the VTX is similar to those of the VTPC.

The VTX consists of 28 modules of time projection chambers along the beam direction (z), with each individual cell (one module consists of two cells) being azimuthally divided into octants. Alternate VTX modules are rotated by 11.3° in ϕ.

The individual chamber octants have sense wires arranged tangentially to the beam, providing track hit information mainly in (r, z) coordinates. In all there are 18 modules with 16 sense wires per octant per cell, and 10 modules on the ends with 24 sense wires per octant per cell. The VTX measures the track up to a radius of 22 cm and in $|\eta| < 3.25$. The typical resolution of the vertex point turned out to be about 1 mm in the z direction.

Central Tracking Chamber (CTC) [31]

The central tracking chamber (CTC) is a 3.2 m long drift chamber with an outer radius of 132 cm, which measures precisely the momentum of charged particles in the polar angle region $40° < \theta < 140°$ ($|\eta| < 1$). The CTC contains 84 cylindrical layers of sense wires which are organized into nine "superlayers" to provide axial and stereo views of the track: five axial superlayers, each consisting of 12 sense wires parallel to the z direction, and four stereo superlayers, each consisting of 6 sense wires titled at $+3°$ or $-3°$ with respect to the z direction. Figure 2.5 shows the end view of the chamber. The direction of the superlayer is tilted by approximately 45° with respect to the radial direction. This tilt angle is determined to minimize the dead space and to linearize the time-to-position relationship of drift electrons under the electric field (1.35 kV/cm) and the magnetic field (1.4 T).

The electrons drift nearly parallel to the particle trajectory with a maximum drift distance of less than 40 mm, corresponding to about 800 ns of drift time. The CTC drift-distance resolution in axial wires is 170 μm for outer layers and 220 μm for inner layers. The spatial resolution of stereo wires in the z direction is 4 mm in cooperation with the axial superlayer signals.

The overall momentum resolution of the SVX - CTC system is $\Delta p_{\mathrm{T}}/p_{\mathrm{T}} = [(0.0009 p_{\mathrm{T}})^2 + (0.0066)^2]^{\frac{1}{2}}$, where p_{T} has units of GeV/c.

2.2.2 Calorimeters

The solenoid and tracking volume of CDF is surrounded by calorimeters, which cover 2π in azimuth, and from -4.2 to 4.2 in η. The calorimeters are segmented in azimuth and pseudorapidity to form a projective tower geometry, which points back to the nominal interaction point. There are three separate η regions of calorimeters, the central, end-plug, and forward. Each region has an electromagnetic calorimeter [central electromagnetic (CEM), plug electromagnetic (PEM), or forward electromagnetic (FEM)] and behind it a hadronic calorimeter. The hadronic calorimeter overlapping the CEM is split into two parts, central (CHA) and wall (WHA), while single systems overlap PEM and FEM (PHA and FHA). In all cases, the absorber in the electromagnetic calorimeter is lead, and in hadronic calorimeter, iron. The locations of calorimeters are indicated in Fig. 2.4.

The η coverages, energy resolutions, and thicknesses of absorbers in the calorimeter components are summarized in Table 2.1 [32]. The absorption thicknesses in the table are given in radiation lengths, X_0, for the electromagnetic calorimeters and in interaction lengths, λ_0, for the hadron calorimeters.

Table 2.1: Summary of CDF calorimeter properties. The symbol $\oplus$ signifies that the constant term is added in quadrature in the resolution. Energy resolutions for the electromagnetic calorimeters are for incident electrons and photons, and for the hadronic calorimeters are for incident isolated pions. Energy is given in GeV. Thicknesses are given in radiation lengths (X_0) and interaction lengths (λ) for the electromagnetic and hadronic calorimeters, respectively.

System	η coverage	Energy resolution	Thickness
CEM	$\lvert\eta\rvert < 1.1$	$13.7\%/\sqrt{E_{\mathrm{T}}} \oplus 2\,\%$	$18\,X_0$
PEM	$1.1 < \lvert\eta\rvert < 2.4$	$22\,\%/\sqrt{E} \oplus 2\,\%$	18-21 X_0
FEM	$2.2 < \lvert\eta\rvert < 4.2$	$26\,\%/\sqrt{E} \oplus 2\,\%$	$25\,X_0$
CHA	$\lvert\eta\rvert < 0.9$	$50\%/\sqrt{E_{\mathrm{T}}} \oplus 3\,\%$	$4.7\lambda_0$
WHA	$0.7 < \lvert\eta\rvert < 1.3$	$75\,\%/\sqrt{E} \oplus 4\,\%$	$4.5\lambda_0$
PHA	$1.3 < \lvert\eta\rvert < 2.4$	$106\,\%/\sqrt{E} \oplus 6\,\%$	$5.7\lambda_0$
FHA	$2.4 < \lvert\eta\rvert < 4.2$	$137\,\%/\sqrt{E} \oplus 3\,\%$	$7.7\lambda_0$

Central electromagnetic calorimeter (CEM) [33]

A perspective view of one central calorimeter wedge is shown in Fig. 2.7. There are 48 wedges in all, 24 on each side of the $z = 0$ plane, covering a polar angle region of $39° < \theta < 141°$ ($|\eta| < 1.1$). Each wedge has an electromagnetic and a hadronic calorimeter part, and is subdivided along the z-axis into ten projective towers, numbered from 0 to 9, where tower 0 is at 90° polar angle. The central towers are 15° wide in ϕ and 0.1 units wide in η.

The CEM consists of 21-31 layers of 5 mm thick polystyrene scintillator (SCSN-38) interleaved with 20-30 layers of 1/8 inch thick lead sheet, corresponding to a total amount of materials of 18 radiation lengths (X_0) including the solenoidal magnet coil of 0.9 radiation lengths. A typical size of a CEM tower cell is 46 cm in the ϕ direction and 24 cm along the beam direction z.

The light from the scintillator is redirected by two wavelength shifter plates on each side located at ϕ-boundaries up through lightguides into two photomultiplier tubes (PMTs) per tower. For the wavelength shifter we used 3 mm thick UVA acrylic plate doped with 30 ppm Y7. The CEM has a total of 956 PMTs.

The energy resolution of the CEM was measured in an electron test beam in the energy range of 15-100 GeV. The energy dependence when electrons are centered in towers is described as

$$\left(\frac{\Delta E}{E}\right)^2 = \left(\frac{13.7\,\%}{\sqrt{E\sin\theta}}\right)^2 + (2\,\%)^2 \qquad (E \text{ in GeV}), \tag{2.3}$$

where the factor $\sin\theta$ reflects the change of the sampling thickness seen by the electron entering the calorimeter at an angle θ.

Calibration of each module was performed using 50 GeV/c electrons, at the center of each tower. The calibration is maintained using ^{137}Cs radioactive sources for the overall calorimeter response, and using Xenon and LED flasher systems for the lightguides and phototubes, respectively.

Located six radiation length deep in the CEM calorimeter, approximately at shower maximum for electromagnetic showers, are the central proportional chambers with strip and wire readout [the central electromagnetic strip chamber (CES)].

Proportional chambers located between the solenoid and the CEM comprise [the central preradiator detector (CPR)].

Central electromagnetic strip chamber (CES)

The central electromagnetic strip chamber (CES) is placed approximately at the CEM shower maximum, 5.9 radiation lengths, and provides shower-position measurements in both the z and ϕ views. Each of the CES modules contains 128 cathode strips aligned in ϕ and 64 anode wires along the z-axis. The wires are ganged in pair, giving a readout pitch of 1.453 cm. The strip width is either 1.67 cm or 2.01 cm depending on $|\eta|$. Such a fine segmentation enables us to measure shower position and transverse profile more precisely than with CEM towers. The position resolution is 2.2 mm in the wire (ϕ) view and 1.4 mm in the strip (z) view for 50 GeV/c electrons.

Central preradiator detector (CPR)

The central preradiator detector (CPR) samples the early development of electromagnetic showers in the material (mainly coil and cryostat of the solenoid magnet) placed in front. The CPR consists of multi-wire proportional gas chambers. There are two MWPC modules located in front of each CEM wedge. In each CPR module there are 32 sense wires along the z axis, providing ϕ information only. The total amount of the material in front of the CPR is about 1.07 radiation lengths at 90° incident.

Since the interactions in the preshower materials depend on the traversing particle (electron, photon, $\pi^0 \to \gamma\gamma$ and hadron), the CPR can distinguish these particles on a statistical basis by applying a certain threshold to the output signal.

Central hadron calorimeter(CHA); endwall hadron calorimeter(WHA)[34]

The CHA consists of 32 layers of 10 mm plastic scintillator interleaved with 32 layers of 25 mm iron. The WHA consists of 15 layers of 10 mm plastic scintillator interleaved with 15 layers of 50 mm iron. The CHA has 9 projective towers numbered from 0 to 8 along the z-axis. The WHA has 6 projective towers numbered from 6

to 11 along the z-axis. The CHA towers 6 to 8 are followed by the WHA towers with the same number to complete towers so that they can contain hadron showers sufficiently. The material thickness of the CHA alone is 4.7 interaction lengths and that of the WHA is 4.5. The energy resolution of the CHA is given by

$$\left(\frac{\Delta E}{E}\right)^2 = \left(\frac{50\,\%}{\sqrt{E\sin\theta}}\right)^2 + (3\,\%)^2 \qquad (E \text{ in GeV}), \tag{2.4}$$

which is derived from test beam pions in the energy range of 10-150 GeV. The energy resolution of the WHA is given similarly by

$$\left(\frac{\Delta E}{E}\right)^2 = \left(\frac{75\,\%}{\sqrt{E}}\right)^2 + (4\,\%)^2 \qquad (E \text{ in GeV}). \tag{2.5}$$

Plug electromagnetic calorimeter (PEM) [35]

The plug electromagnetic calorimeters cover the polar angle regions $10° < \theta < 36°$ and $144° < \theta < 170°$ ($1.1 < |\eta| < 2.4$), enclosing the ends of the CTC. The sensitive part of the PEM consists of arrays of conductive plastic proportional tubes (7×7 mm^2) interleaved with 34 layers of 2.69 mm thick lead absorber panels. Signals are read out by cathode pads which are arranged to construct the tower geometry. The tower segmentation is $\Delta\eta \sim 0.09$ and $\Delta\phi \sim 5°$. The PEM has a total of 1152 towers per end, each tower being segmented into three longitudinally. The energy resolution was measured in an electron test beam in the energy range of 20-200 GeV:

$$\left(\frac{\Delta E}{E}\right)^2 = \left(\frac{22\,\%}{\sqrt{E}}\right)^2 + (2\,\%)^2 \qquad (E \text{ in GeV}). \tag{2.6}$$

Electromagnetic shower positions are measured in the PEM with θ- and ϕ-oriented strips located at the shower maximum, giving a position resolution of approximately 0.2 cm by 0.2 cm.

Plug hadronic calorimeter (PHA) [36]

Each of the plug hadronic calorimeters, located behind the PEMs, consists of 20 layers of gas proportional tubes interleaved with 20 layers of 51 mm thick steel absorber. The PHA has a total of 864 towers per end. The material thickness of

the PHA only is 5.7 interaction lengths. The energy resolution for the PHA was measured as

$$\left(\frac{\Delta E}{E}\right)^2 = \left(\frac{106\,\%}{\sqrt{E}}\right)^2 + (6\,\%)^2 \qquad (E \text{ in GeV}). \tag{2.7}$$

Forward electromagnetic calorimeter (FEM) [37]

The forward electromagnetic calorimeters are located approximately 6.5 m from the interaction point in both the proton and the antiproton beam directions. The FEMs cover the polar angle regions $2^\circ < \theta < 13^\circ$ and $167^\circ < \theta < 178^\circ$ ($2.2 < |\eta| < 4.2$). The FEM calorimeter module constructs the projective towers segmented into 5° in ϕ and 0.1 units in η. Each FEM module consists of 30 sampling layers, each of which is composed of a 0.48 cm thick lead absorber panel and a chamber of gas proportional tubes with cathode readout. The FEM module is segmented into two longitudinally, giving a total readout channels of 5760 for the both ends. The FEM position resolution for single electrons varies between 1 and 4 mm depending on the location in the calorimeter. The energy resolution is given by

$$\left(\frac{\Delta E}{E}\right)^2 = \left(\frac{26\,\%}{\sqrt{E}}\right)^2 + (2\,\%)^2 \qquad (E \text{ in GeV}). \tag{2.8}$$

Forward hadron calorimeter (FHA) [38]

The FHA covers the forward region from 2.3 to 4.2 in η with an additional 7.7 interaction lengths behind the FEM. The FHA consists of 27 sampling layers of proportional tube chambers alternated with 51 mm thick iron plates. The FHA has a total of 2880 readout channels for both ends. The energy resolution is given by

$$\left(\frac{\Delta E}{E}\right)^2 = \left(\frac{137\,\%}{\sqrt{E}}\right)^2 + (3\,\%)^2 \qquad (E \text{ in GeV}). \tag{2.9}$$

2.2.3 Muon detectors

Central muon detection system (CMU) [39]

The central muon detection system (CMU) is located around the outside of the central hadronic calorimeter. Muons with p_{T} larger than 1.4 GeV/c can reach the CMU. The CMU system extends to $|\eta| = 0.6$ with the azimuthal coverage of approximately 84%. The CMU is segmented in ϕ into 24, which fit into the top of each central calorimeter wedge, giving 48 wedges in total. Each CMU wedge is further segmented in ϕ into three modules. A module consists of 16 drift tubes with 2.26 m length in z which are arranged in four layers along the muon trajectory. Two of the four sense wires, from alternating layers, lie on a radial line which passes through the interaction point. The remaining two wires lie on a radial line which is offset from the first by 2 mm. The known offsets in the drift times can resolve the left-right ambiguity of the track. The chambers use stainless steel resistive sense wires and operate in the limited streamer mode in order to obtain the z position by charge division.

Central muon upgrade (CMP) [40]

An additional system of muon chambers, the central muon upgrade (CMP), is located behind the CMU system. As the absorber of 0.6 m thick steel ($\sim$ 3 absorption lengths) between the two systems, we have added two steel walls on both sides while we utilize the solenoid return yokes on the top and bottom of the detector. The chambers of fixed length in z form a four-sided box around the central detector, hence the pseudorapidity coverage varies with azimuth as shown in Fig. 2.8. Approximately 63% of the solid angle is covered by the CMP for $|\eta| < 0.6$.

The CMP consists of in total 864 drift tubes with dimensions of $2.5 \times 15 \times 640$ cm^3. The CMP drift tubes are stacked in four layers along the trajectory with half a cell staggered. The position resolution in a single tube is about 300 μm.

Central muon extension (CMX)

The central muon extension (CMX) consists of four free-standing conical arches (Fig. 2.2) located at each end of the central detector, extending the muon coverage to $0.6 < |\eta| < 1.0$. The CMX covers approximately 71% of the solid angle for this η range. The CMX drift tubes with 1.8 m length are arrayed as a logical extension of CMP. There are four logical layers of twelve tubes in each sector which covers $\Delta\phi = 15°$. Each logical layers consists of two physical layers of drift tubes which partially overlap with each other, creating a stereo angle of 3.6 mrad between adjacent tubes. Thus the CMX can resolve left-right ambiguities and measure the track in the azimuth and polar angle views. There are 16 CMX sectors installed for each side, giving in total 1728 readout channels.

2.2.4 Beam-beam counter

The beam-beam counter (BBC) [41] is a plane of 16 scintillation counters located on the front face of each of the forward and the backward calorimeters. Fig. 2.9 shows a beam's-eye view of one of the BBCs. They provide a minimum-bias trigger for the detector, and are also used as the primary luminosity monitor. The timing properties of the BBCs are excellent ($\sigma < 200$ psec) to measure the time of the interaction. They cover the angle region from 0.32° to 4.47° measured along either the x or y axis, corresponding to the pseudo-rapidity range from 3.24 to 5.90.

2.2.5 Trigger system

The CDF trigger is a four-level system of level 0, 1, 2, and 3. Each level is a logical OR of a number of triggers designed to select events such as electrons, muons, and jets.

The level-0 trigger requires the signature of an inelastic collision, which is defined by the coincidence of the beam-beam counter (BBC) system.

Preamplifiers on detector channels provide two outputs: one, the "fast output," for immediate use by the trigger system, and the other for temporary front-end data storage until the trigger decision is made. The level-1 uses fast outputs from the

central muon detectors for muon triggers and fast outputs from all the calorimeters for electron and jet triggers. The calorimeter information is summed into logical towers of $(\Delta\eta = 0.2) \times (\Delta\phi = 15°)$, a 42×24 array, for both the electromagnetic and hadronic calorimeters. The level-1 trigger requires that transverse energy in these towers exceeds a certain threshold energy. The rate of level-1 triggers is maintained not to exceed ~ 5 kHz by adjusting the threshold energy and the prescale factors.

The level-2 uses the calorimeter trigger information with greater sophistication. A list of calorimeter clusters is provided by a nearest-neighbor hardware cluster finder. For each cluster, the transverse energy E_{T}, average ϕ, and average η are determined. For electron and muon triggers this information is combined with a list of r-ϕ tracks provided by the central fast tracker (CFT) [42], a hardware track processor, which uses fast timing information from the CTC as input. For example, the level-2 trigger requires for electron candidates that an electromagnetic cluster with E_{T} larger than the threshold matches to a CFT track with p_{T} above the threshold. The CFT momentum resolution is $\delta p_{\mathrm{T}}/p_{\mathrm{T}} \approx 0.035 \times p_{\mathrm{T}}$. The level-2 output rate is approximately 50 Hz at a typical luminosity.

The level-3 trigger is made up of 48 Silicon Graphics computers, each containing two event buffers, plus an array of service hardware to push the data into and out of 96 buffers. Each event is sent to a single buffer, and so that level-3 triggers can be processed up to 48 separate events in parallel, with another 48 events meanwhile being loaded to the secondary buffers. The algorithms used in this "online" system are identical to those used in subsequent "offline" reconstruction of the events. The offline clustering algorithm is described in detail in Chapter 3. Most of the execution time is used for three-dimentional track reconstruction in the CTC. The output rate of the level-3 trigger was approximately 10 Hz, and the events were stored on 8 mm magnetic tape for offline processing. A subset of the events flagged in the level-3 trigger is written on a disk as a separate file for immediate offline processing.

2.2.6 Data acquisition system

The CDF data acquisition system (DAQ) [43] employs a multilevel FASTBUS network. The DAQ system is designed to allow partitioning into semi-independent

sections for parallel development and calibration studies of different detector components.

When an event is accepted by both level-1 and level-2, the data from front end crates are digitized and read by scanner modules. There are two major types of front end electronics. All the calorimeters and central muon system use RABBIT (redundant analog bus-based information transfer) systems which are read by MX scanners. Most tracking detectors use FASTBUS front end systems which are read by SSP scanners. A few CAMAC modules are included in the event data stream and are read by an SSP scanner using a FASTBUS to CAMAC interface. Each scanner can buffer four events. This step in the DAQ pipeline is managed by the trigger supervisor (TS) FASTBUS module. The TS uses a combination of FASTBUS messages and dedicated control lines to provide flexible and efficient control of front end systems. Each partition is allocated a unique set of scanners and a trigger supervisor.

When all MX and SSP scanners have finished reading and buffering data for one event, the TS module sends a FASTBUS message to the buffer manager (BFM) indicating that an event is available in a specified buffer. The BFM supervises dataflow from the scanner modules to the host VAX computers. The BFM initiates this dataflow by sending a FASTBUS message to the event builder (EVB) instructing it to "Pull" an event from the same buffer in all scanners of a specified detector partition. The EVB is a group of FASTBUS modules which can read, buffer and reformat complete events from any allowed partition of detector components. When the EVB has finished reading data from scanner buffer N, it sends a "Pull OK" message to the BFM which in turn notifies the TS that buffer N is available for a new level-1 and level-2 trigger.

Under direction of the BFM, the EVB writes a complete event into a specified node in the level-3 processor farm (Silicon Graphics computers). Events accepted by the level-3 trigger are read by the buffer multiplexer executing on one or more computers in the VAX cluster. Event data can be logged to disk or tape.

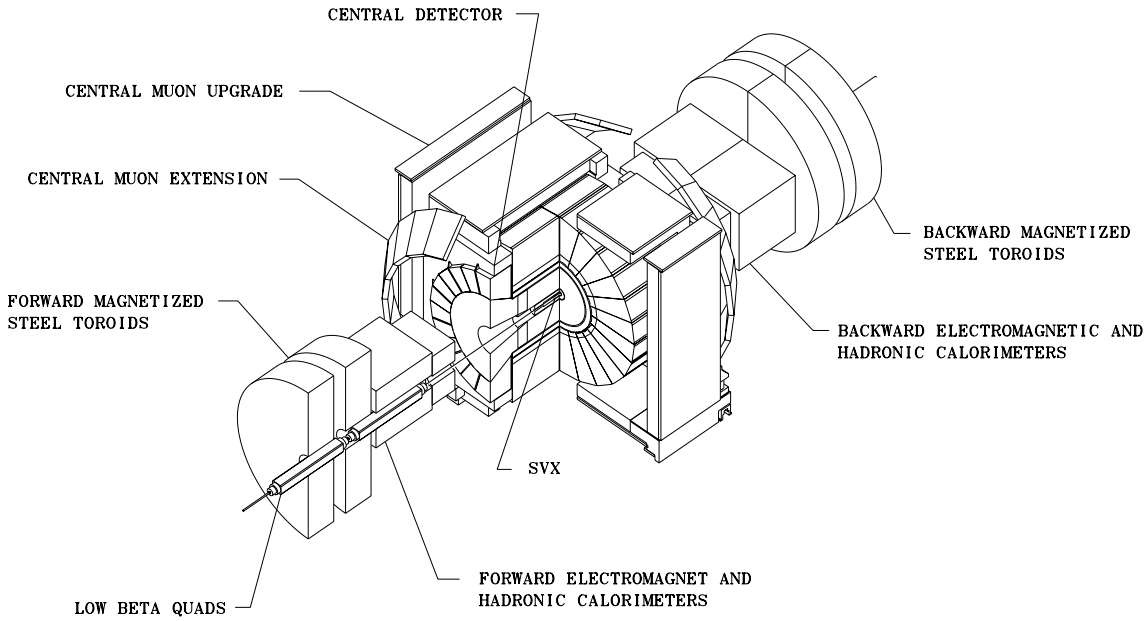

Figure 2.2: A perspective view of the CDF detector showing the central detector, the forward and the backward detectors.

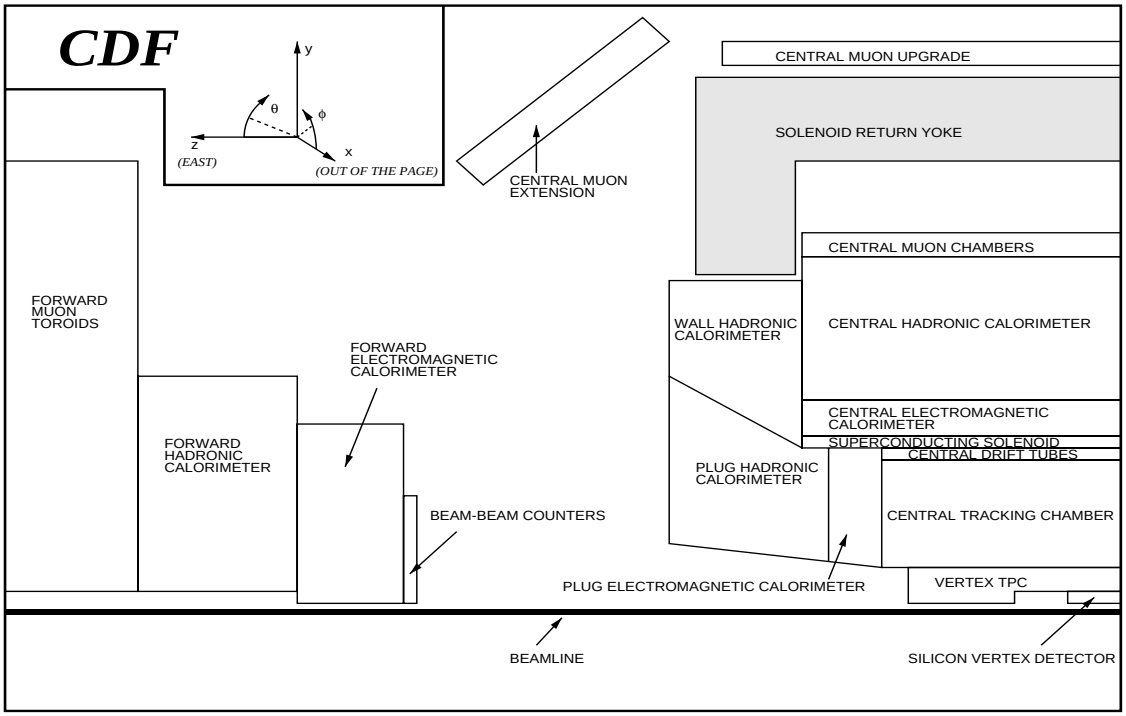

Figure 2.3: A side-view cross section of the CDF detector. The detector is forward-backward symmetric about the interaction point.

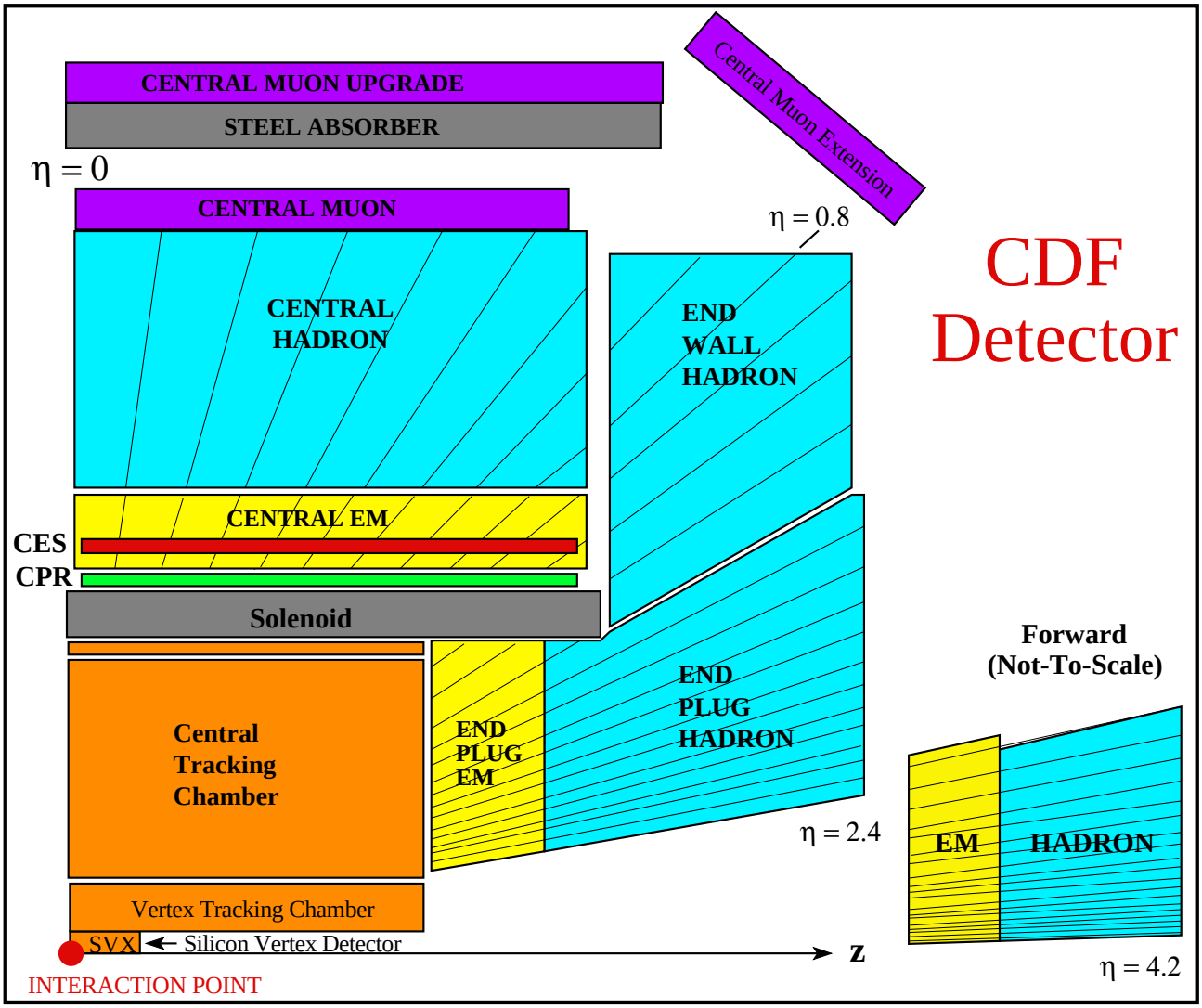

Figure 2.4: Cross-sectional view of the central detectors.

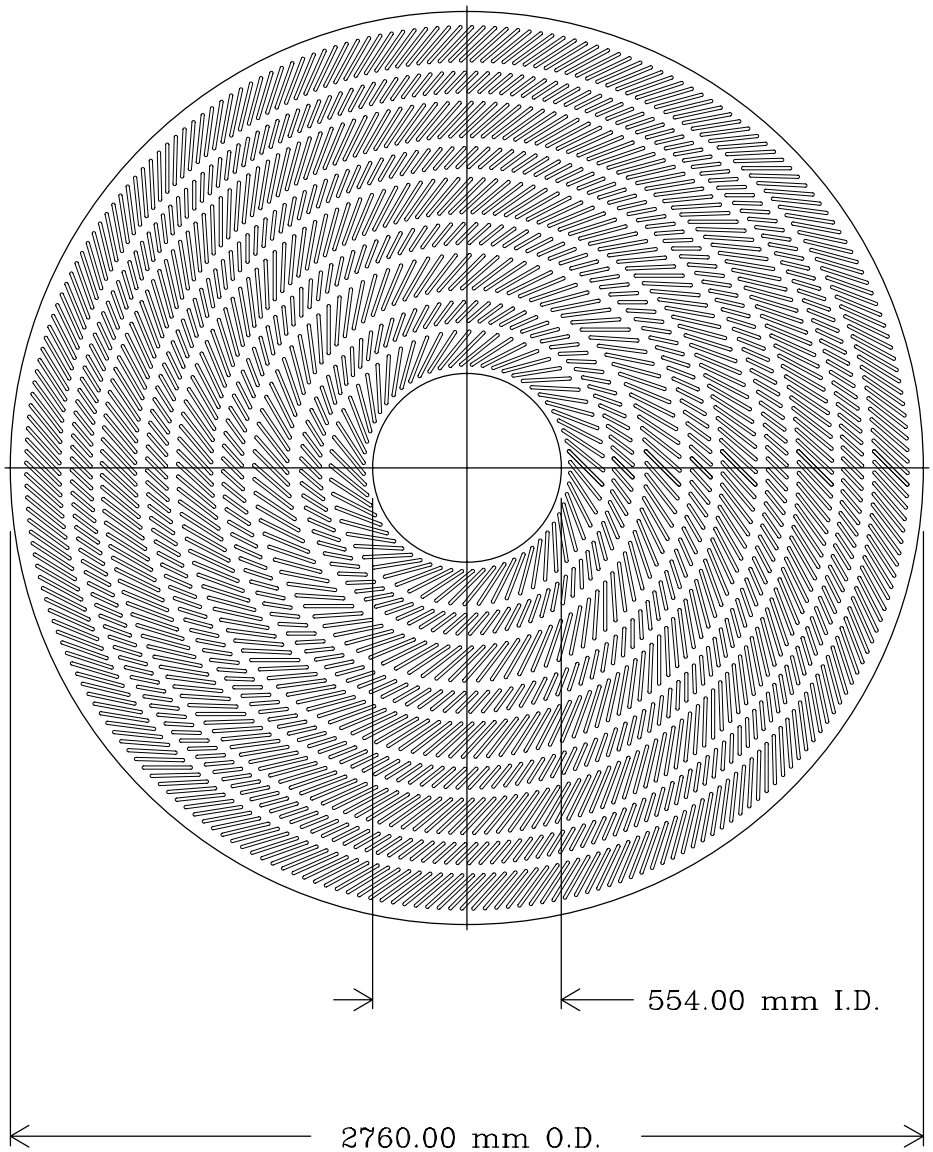

Figure 2.5: Endplate of the CTC showing the arrangement of the slots which hold in total 36,504 wires.

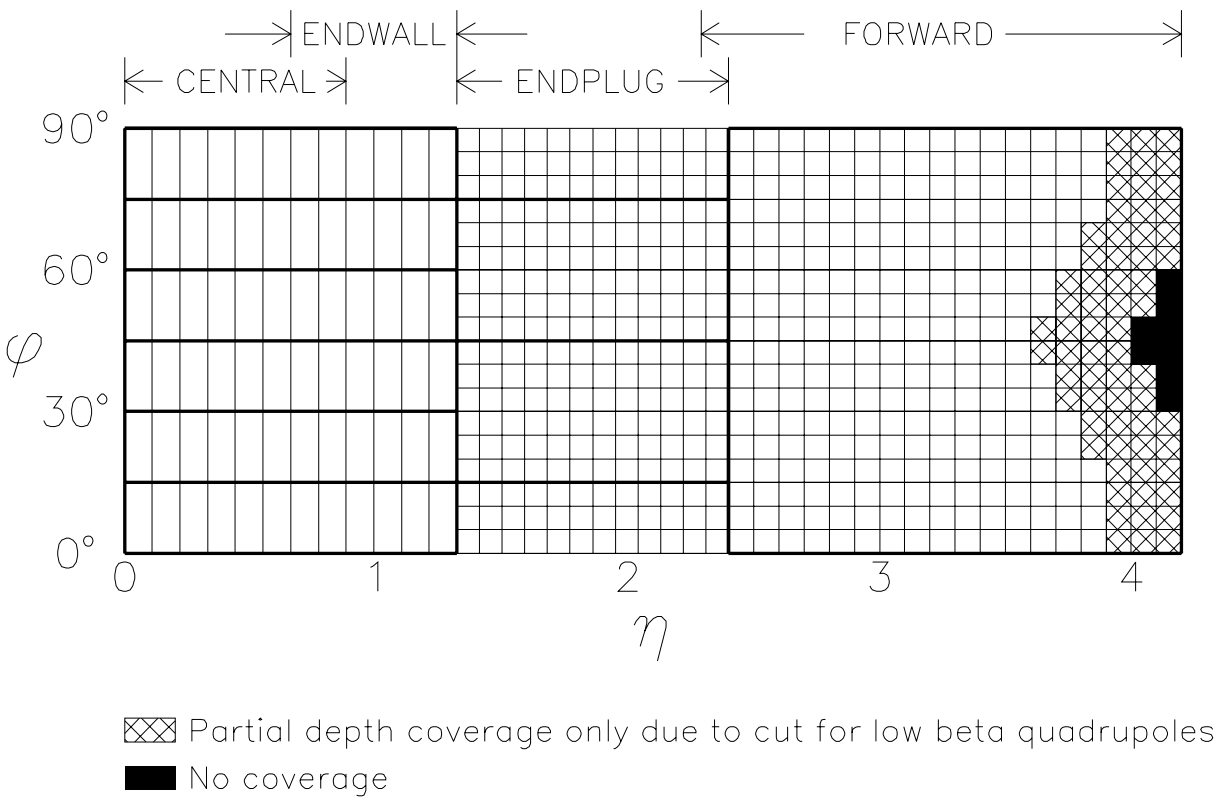

Figure 2.6: Hadron calorimeter towers in one of eight identical η-ϕ quadrants ($\Delta\phi = 90^\circ, \eta > 0$). The heavy lines indicate module or chamber boundaries. The EM calorimeters have complete ϕ coverage out to $\eta = 4.2$.

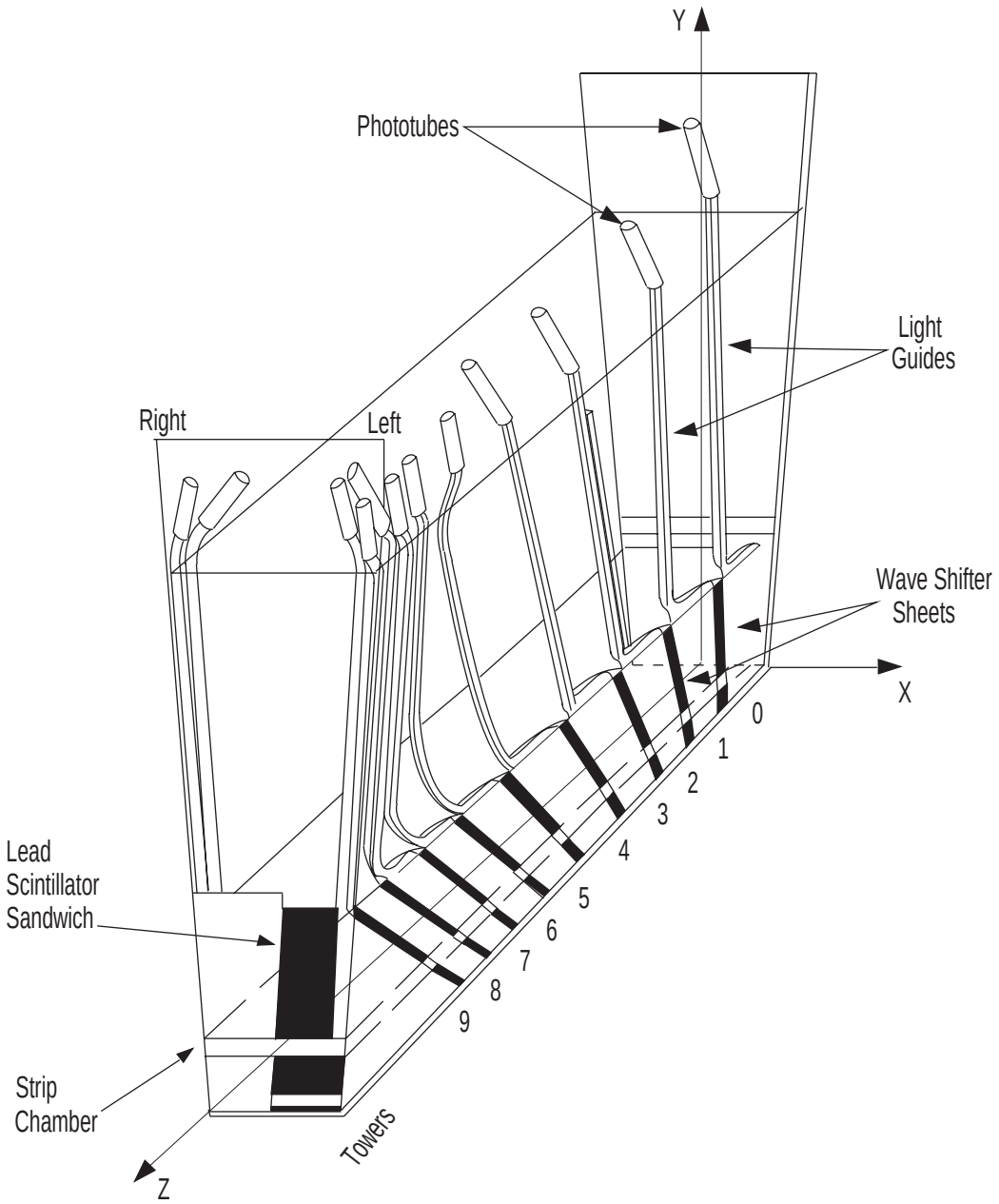

Figure 2.7: Schematic of a wedge module of the central calorimeter showing the layout of the light-gathering system.

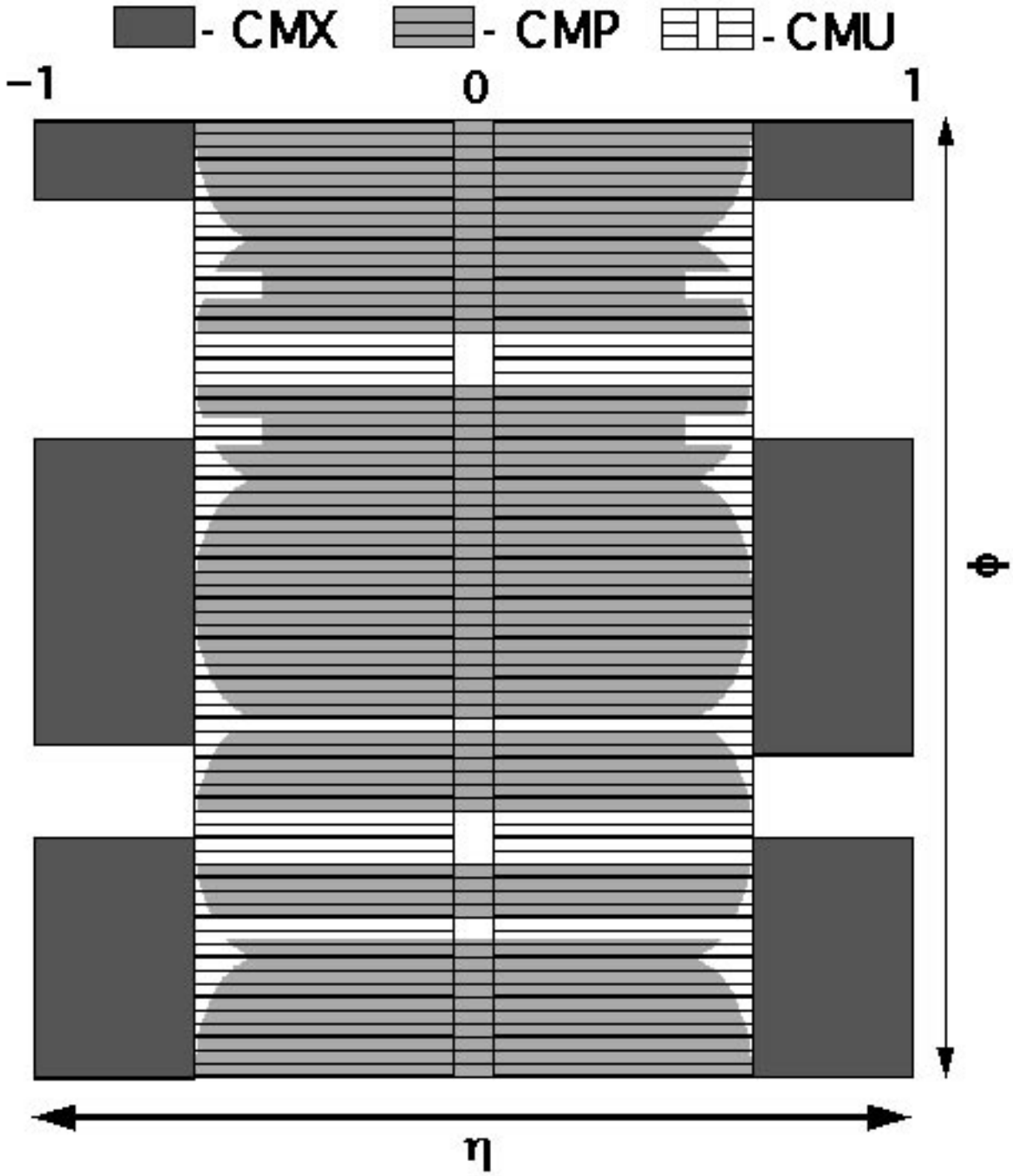

Figure 2.8: Map of central muon detector coverage in η-ϕ.

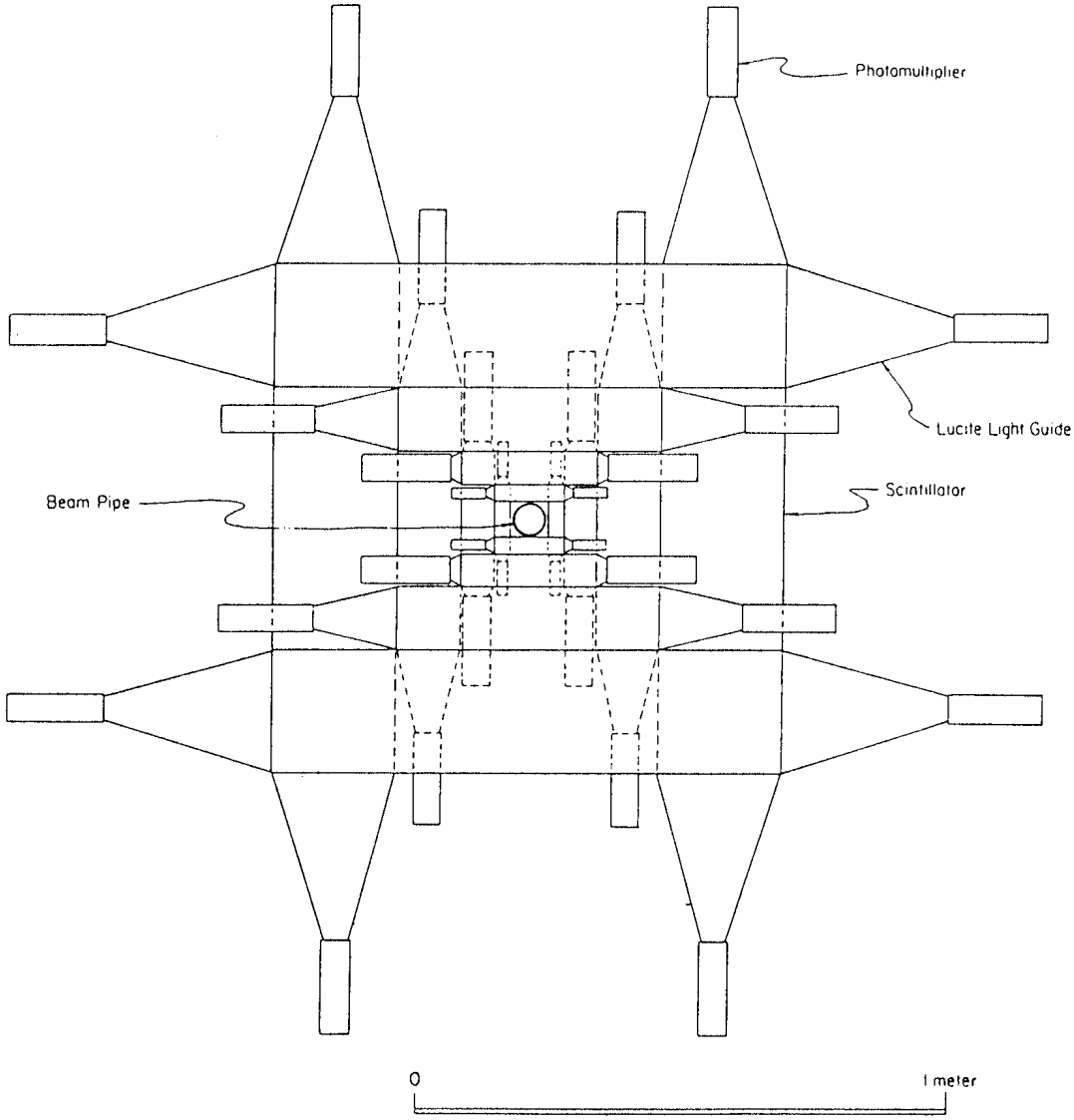

Figure 2.9: A beam's eye view of one of the beam-beam counter planes.

2.2.7 Luminosity measurement

The CDF luminosity is measured with the beam-beam counters. The counters see most of the inelastic scattering events, with small contributions from diffractive scattering events. The coincidence rate of the two sets of counters is related to the luminosity, with the mean number of interaction per beam-beam crossing (μ) given by

$$\mu = \frac{\sigma_{BBC} \cdot \mathcal{L}}{f}. \tag{2.10}$$

Here σ_{BBC} is the BBC cross section, which is explained below in detail, f = 286.278 kHz is the crossing frequency, and $\mathcal{L}$ is the instantaneous luminosity. The number of interactions per crossing (n) follows Poisson statistics:

$$P(n) = \frac{\mu^n e^{-\mu}}{n!} \tag{2.11}$$

with the probability of having one or more BBC coincidences per crossing given by:

$$\sum_{n=1}^{\infty} P(n) = 1 - P(0) = 1 - e^{-\frac{\sigma_{BBC}}{f} \cdot \mathcal{L}}. \tag{2.12}$$

The rate of BBC triggered events R_{BBC} is given by $\mu \times f$. We can extract the true luminosity $\mathcal{L}$ from the BBC rate:

$$\mathcal{L} = -\frac{\ln(1 - \frac{R_{BBC}}{f})}{\frac{\sigma_{BBC}}{f}}. \tag{2.13}$$

The value of σ_{BBC} can be expressed as

$$\sigma_{BBC} = \sigma_{tot} \cdot \mathrm{Acc} = \sigma_{tot} \cdot \frac{R_{BBC}}{R_{el} + R_{inel}}, \tag{2.14}$$

where Acc refers to the BBC acceptance, and R_{el} and R_{inel} are the rates of elastic and inelastic events.

The proton-antiproton total cross section σ_{tot} is the sum of the elastic and inelastic rates divided by the luminosity $\mathcal{L}$:

$$\sigma_{tot} = \frac{1}{\mathcal{L}}(R_{el} + R_{inel}). \tag{2.15}$$

The optical theorem relates the total cross section to the imaginary part of the elastic scattering rate at low four-momentum transfer squared (t) :

$$\sigma_{tot}^2 = \frac{16\pi(\hbar c)^2}{1+\rho^2}\frac{1}{\mathcal{L}}\left.\frac{dR_{el}}{dt}\right|_{t=0}, \tag{2.16}$$

where ρ is the ratio of the real to imaginary part of the forward elastic scattering amplitude. Dividing (2.16) by (2.15) yields

$$\sigma_{tot} = \frac{16\pi(\hbar c)^2}{1+\rho^2}\frac{\left.\frac{dR_{el}}{dt}\right|_{t=0}}{(R_{el}+R_{inel})}. \tag{2.17}$$

The elastic and inelastic event rates R_{el}, R_{inel} and $\frac{dR_{el}}{dt}$ were measured by CDF [46, 47]. In brief $\frac{dR_{el}}{dt}$ is determined by extrapolating the measured $\frac{dR_{el}}{dt}$ distribution with Monte Carlo corrections for the acceptance, R_{inel} is a sum of the event rates with a two-sided coincidence of either the BBC or the forward telescopes which cover $3.8 < |\eta| < 5.5$, and R_{el} is $\frac{dR_{el}}{dt}$ divided by the inelastic slope parameter. The value $\rho = 0.140 \pm 0.069$ at $\sqrt{s} = 1.8$ TeV is due to E-710 collaboration [48]. By substituting these values into Eq.(2.17), we calculate $\sigma_{BBC} = 51.15 \pm 1.60$ mb from Eq.(2.14). [1] Then we get the luminosity using Eq.(2.13). Combining the measurement uncertainty with the acceptance and correction uncertainties gives a total uncertainty of 8% in the integrated luminosity [49].

[1] In previous publications, CDF normalized the BBC cross section ($\sigma_{BBC} = 46.8 \pm 3.2$ mb) to UA4 [44] and accelerator measurements at $\sqrt{s} = 546$ GeV, which was extrapolated to $\sqrt{s} = 1.8$ TeV [45].

Chapter 3

Two jet production cross section

3.1 Event selection

3.1.1 Jet triggers

The CDF has inclusive jet triggers Jet20, Jet50, Jet70 and Jet100 where the numbers originate in jet E_{T} thresholds at level-2. Table 3.1 shows the jet E_{T} thresholds, prescale factors, and the E_{T} ranges used in this analysis [see Section 3.2.3 for E_{T} ranges]. The prescale factor (PF) is implemented for the purpose of reducing the trigger rate to an acceptable level, where only a fraction (1/PF) of events are allowed to pass the trigger. At level-1 Jet20 and Jet50 require that at least one logical tower has E_{T} greater than 4 GeV in electromagnetic or hadronic calorimeters. Jet70 and Jet100 require that any one of level-1 triggers is satisfied. At level-2 the threshold is applied to level-2 calorimeter cluster energies for Jet20, Jet50, and Jet70. The level-3 threshold is looser than the level-2 threshold for these triggers, and it is 80 GeV for Jet100 where no prerequisite is applied at level-2. The integrated luminosity is a sum of those from good quality runs where no instrumental problem was found. The integrated luminosity differs slightly among triggers, 86.1–86.4 pb^{-1} as shown in the table.

Table 3.1: Integrated luminosity, prescale factors (PF), threshold transverse energies (in GeV), and E_{T} range used in this analysis. The numbers are given for jet triggers, Jet20 to Jet100 and for level-1 to level-3. No level-1 prerequisite is made at level-2 for Jet70 and Jet100, and no level-2 prerequisite at level-3 for Jet100.

Jet trigger	Luminosity (pb^{-1})	Level-1 threshold	L-1 PF	Level-2 threshold	L-2 PF	Level-3 threshold	Offline range
Jet20	86.4	4	40	20	25	10	40-80
Jet50	86.4	4	40	50	1	35	80-100
Jet70	86.4	any L-1	1	70	8	55	100-125
Jet100	86.1	any L-1	1	any L-2	1	80	125-450

3.1.2 Jet reconstruction

Jets are reconstructed using an algorithm which forms clusters from the recorded energies deposited in the calorimeter towers. The CDF jet algorithm starts by searching for calorimeter towers with $E_{\mathrm{T}} > 1$ GeV. In the plug and forward calorimeter regions, towers are grouped together in sets of three in ϕ, spanning 15° to correspond to the central segmentation. Preclusters are formed from an unbroken chain of contiguous seed towers with a continuously decreasing E_{T}. If a tower is outside a window of 7×7 towers surrounding the seed, it is used to form a new precluster. These preclusters are used as a starting point for cone clustering.

The preclusters then are grown into clusters. First, the E_{T} weighted centroid of the precluster is found and a cone with a radius R in η-ϕ space is formed around the centroid, where R is $\sqrt{\Delta\eta^2 + \Delta\phi^2}$ with $\Delta\eta$ and $\Delta\phi$ being η and ϕ differences from the centroid. Then, all towers with an E_{T} of at least 0.1 GeV are incorporated into the cluster if the tower centroid is inside the cone of $R = 0.7$. The cluster directions in η-ϕ space are computed from the E_{T} weighted center of gravities of the constituent tower energy depositions. The cluster directions are then recomputed and the lists of additional towers are recalculated using the new cluster directions. The process of recomputing the additional tower lists and the resulting cluster directions is repeated until the list of towers associated with each cluster remains unchanged in two consecutive passes. At the end of this process towers can in principle be assigned to more than one cluster. If this happens then the two overlapping clusters are merged if more than 75% of the E_{T} of the lowest-E_{T} cluster is in the overlapping

region. If this is not the case then the towers in overlapping region are assigned to the nearest cluster in η-ϕ space. After the towers are uniquely assigned to the clusters, the centroids are recomputed. As with the original cluster finding, the process of centroid computation and tower reshuffling is iterative, and ends when the tower lists remain fixed.

From the towers associated with the cluster, the quantities (p_x, p_y, p_z, E) are calculated. The electromagnetic and hadronic compartments of each tower are assigned massless four-vectors with magnitude equal to the energy deposited in the tower and with the direction defined by a unit vector pointing from the event origin to the center of the calorimeter tower (calculated at the depth that corresponds to shower maximum). E is the scalar sum of tower energies; p_x is the sum of $p_{x,i}$ where i is the tower index. The transverse energy E_{T} is then determined as $E_{\mathrm{T}} \equiv E \sin\theta = E\sqrt{p_x^2 + p_y^2} \,/\sqrt{p_x^2 + p_y^2 + p_z^2}$.

3.1.3 Two jet event selection

We define the two jets in two different η regions, $0.1 < |\eta_1| < 0.7$ (*central* jet) and $0.1 < |\eta_2| < 3.0$ (*second* jet). The two jet cross section is expressed as a function of E_{T} of the central jet with requiring the second jet in one of the four η_2 bins, $0.1 < |\eta_2| < 0.7$, $0.7 < |\eta_2| < 1.4$, $1.4 < |\eta_2| < 2.1$, and $2.1 < |\eta_2| < 3.0$. Note that if two jets are in $0.1 < |\eta| < 0.7$, this event has two entries where we assign either one of the jets as the central jet.

The jets should satisfy:

- Event vertex cut: $|Z_{\mathrm{vertex}}| < 60\,\mathrm{cm}$
- Missing E_{T} significance: $\frac{\not{E}_{\mathrm{T}}}{\sqrt{\Sigma E_{\mathrm{T}}}} < 6$
- Corrected $E_{\mathrm{T}1} > 40$ GeV for central jets
- Corrected $E_{\mathrm{T}2} > 10$ GeV for *second* jets

Here "Corrected" E_{T} refers to the transverse energy corrected by taking into account of calorimeter nonuniformity. The details of calorimeter response nonuniformity is described in section 3.3. The vertex and $\not{E}_{\mathrm{T}}$ significance cuts are described below.

3.2 Detection efficiency

3.2.1 Event vertex cut

In order to ensure that particles from an event are well detected with the calorimeter, the z position of event vertex, Z_{vertex}, is required to be near the nominal event vertex. The Z_{vertex} cut efficiency is calculated as the number of events within $|Z_{\mathrm{vertex}}| < 60\,\mathrm{cm}$ divided by that within $|Z_{\mathrm{vertex}}| < 150\,\mathrm{cm}$. It depends on the trigger as shown in Fig. 3.1, which ranges from 92.8% (Jet20) to 91.0% (Jet100). In this analysis, Z_{vertex} cut efficiency of 92.5% is taken.

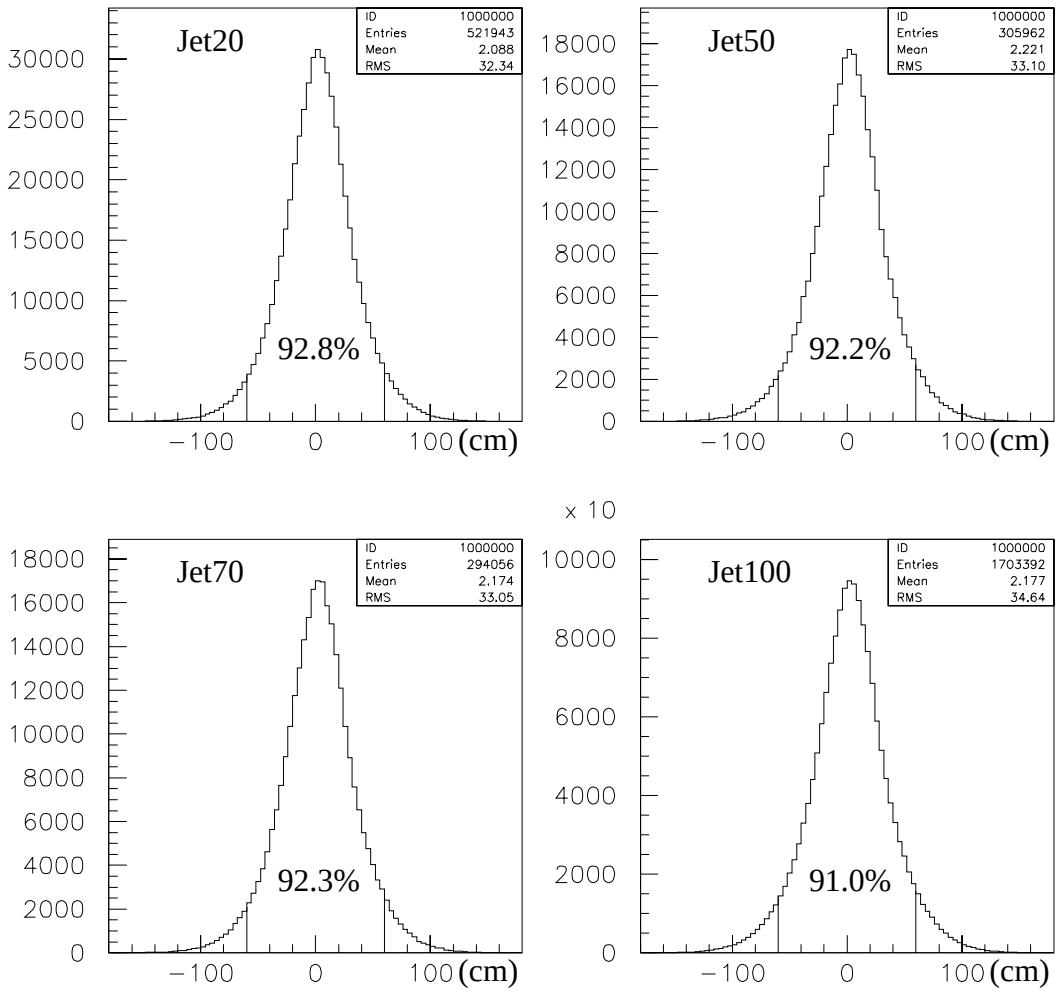

Figure 3.1: Z_{vertex} distribution of four inclusive jet triggers. The percentage in each histogram is the number of events within $|Z_{\mathrm{vertex}}| < 60\,\mathrm{cm}$ divided by that within $|Z_{\mathrm{vertex}}| < 150\,\mathrm{cm}$.

3.2.2 $\not\!\!E_{\rm T}$ significance cut

Missing transverse energy ($\not\!\!E_{\rm T}$) is defined to be the negative of the vector sum of transverse energy in all calorimeter towers in $|\eta| < 3.6$:

$$\not\!\!E_{\rm T} \equiv | - \sum_{tower} \vec{E_{\rm T}}^{tower} |, \tag{3.1}$$

where $\vec{E_{\rm T}}^{tower}$ is a two-dimensional vector pointing from the event vertex to the tower centroid. The η range is restricted by the final focusing magnets of Tevatron inside of the forward hadronic calorimeter. To be included in the sum, individual tower energies (E, not $E_{\rm T}$) must exceed detector-dependent energy thresholds. The thresholds are 0.1 GeV in the CEM, CHA, and WHA, 0.3 GeV in the PEM, 0.5 GeV in the PHA and FEM, and 0.8 GeV in the FHA. The uncertainty on $\not\!\!E_{\rm T}$ is proportional to $\sqrt{\sum E_{\rm T}}$, where $\sum E_{\rm T}$ is a scalar sum of the transverse energy in all calorimeter towers. We therefore define the $\not\!\!E_{\rm T}$ significance as the ratio of $\not\!\!E_{\rm T}$ to $\sqrt{\sum E_{\rm T}}$, and require the ratio to be smaller than 6 (see Fig. 3.2) to ensure that no significant missing energy is detected.

3.2.3 Trigger efficiency

The trigger efficiencies are shown as a function of corrected jet $E_{\rm T}$ in Fig. 3.3 for Jet20, Jet50, Jet70, and Jet100 triggers. The trigger efficiency for Jet50 is derived using the Jet20 data sample as the ratio of the number of events which satisfied the Jet50 level-2 and level-3 requirements to that in Jet20. The Jet70 and Jet100 trigger efficiency is measured using the Jet50 data sample. To measure the Jet20 trigger efficiency, we select the sample where the second jet passes the Jet20 level-2 and level-3 requirements. We evaluate the Jet20 trigger efficiency as the event fraction where the central jet satisfies the Jet20 level-2 and level-3 requirements in this sample.

In order to suppress the trigger biases, the data in specific $E_{\rm T}$ ranges are used: $40 < E_{\rm T} < 80$ GeV for Jet20, $80 < E_{\rm T} < 100$ GeV for Jet50, $100 < E_{\rm T} < 125$ GeV for Jet70, and $E_{\rm T} > 125$ GeV for Jet100.

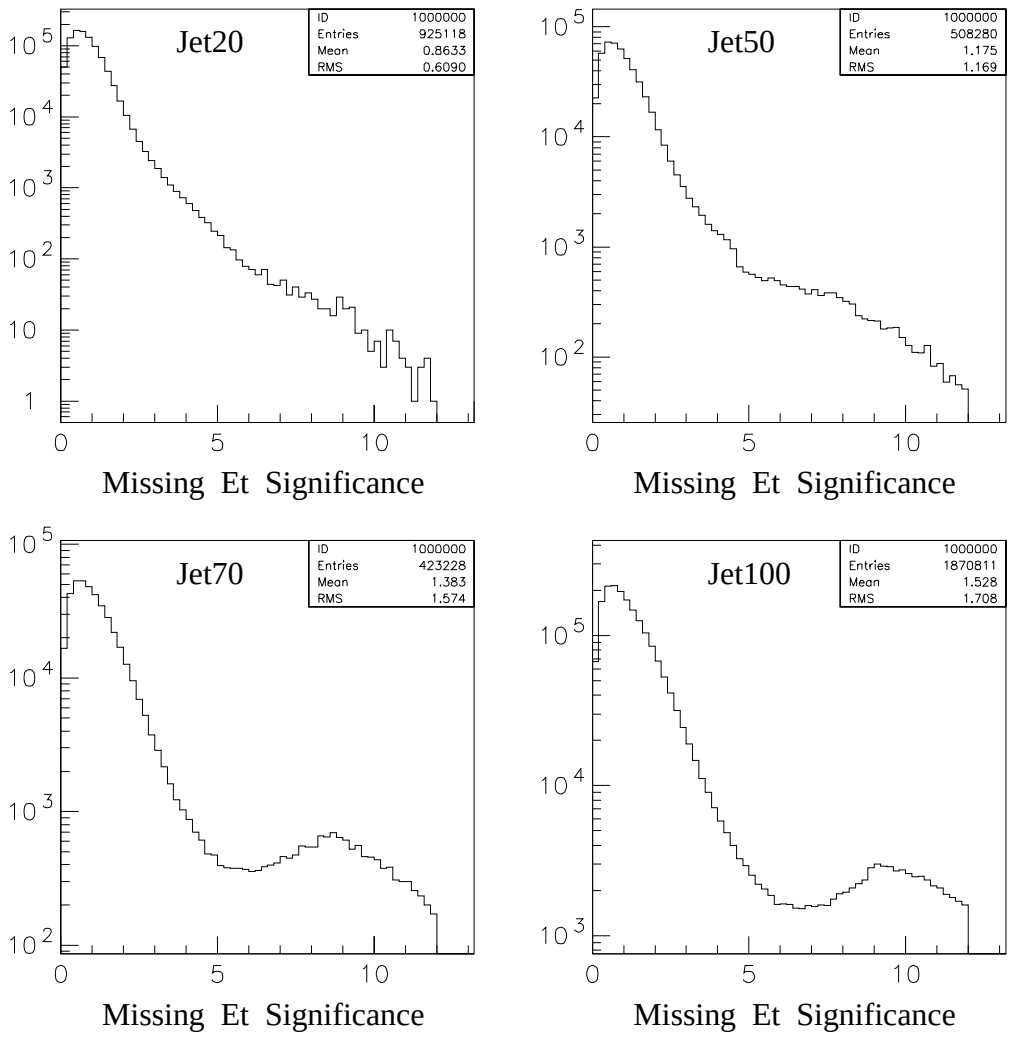

Figure 3.2: Missing E_{T} significance distributions for the Jet20, Jet50, Jet70, and Jet100 triggers. The distributions are truncated at 12.

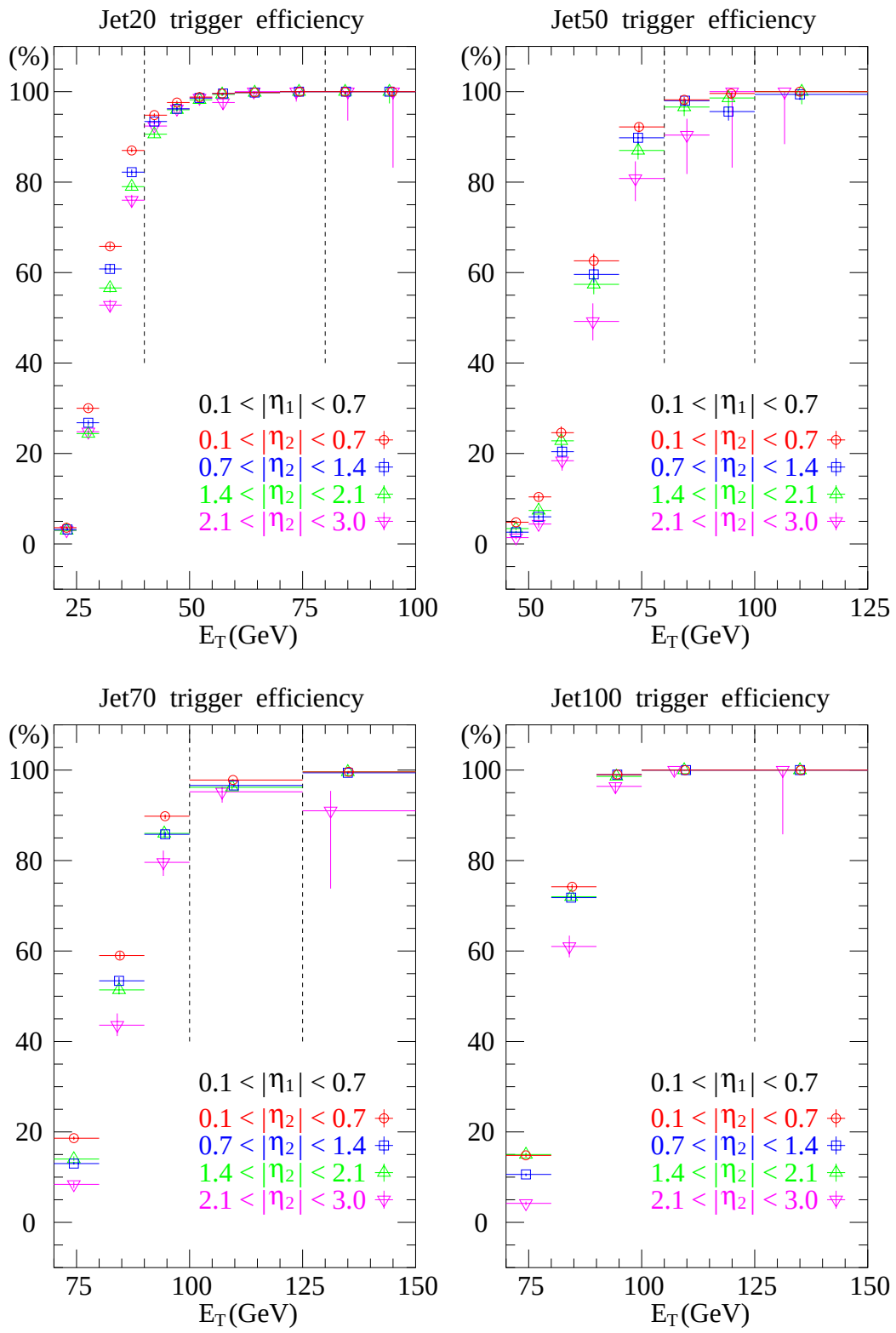

Figure 3.3: Trigger efficiency for the Jet20, Jet50, Jet70, and Jet100 triggers. The vertical dashed lines show the range of E_T used in this analysis.

3.3 Two Jet Cross Section

We have obtained a measured differential cross section $d^3\sigma/dE_{\rm T}d\eta_1 d\eta_2$ given by

$$\frac{d^3\sigma}{dE_{\rm T}d\eta_1 d\eta_2} = \frac{\Delta N}{\epsilon\,\mathcal{L}\,\Delta E_{\rm T}^{measured}\Delta\eta_1\Delta\eta_2}, \tag{3.2}$$

where ϵ is the detection efficiency, $\mathcal{L}$ is the integrated luminosity, ΔN is the number of events in each measured $E_{\rm T}$ (pre-unsmearing) and η_2 bin, and $\Delta\eta_1$ is the eta_1 bin width being $2\times(0.7-0.1) = 1.2$. It is shown for $0.1 < |\eta_1| < 0.7$ and $0.1 < |\eta_2| < 0.7$ in Fig. 3.4. The "raw" two jet cross section in the Figure does not correct the trigger inefficiency, which indicates that "Offline range"s in Table 3.1 are reasonable.

To obtain a true differential two jet cross section, we have to account for $E_{\rm T}$ smearing effect as described below.

3.3.1 $E_{\rm T}$ smearing due to finite calorimeter response

The jet transverse energy $E_{\rm T}$ differs from the true parton $E_{\rm T}$ for a variety of reasons. Some of these are the result of limitations in detector performance.

1) The calorimeter response to low-energy charged pions exhibits a nonlinearity for momenta below 10 GeV.

2) Charged particles with transverse momenta below $\sim$ 400 MeV bend sufficiently in the magnetic field so that they do not reach the calorimeter. At slightly higher transverse momenta, the magnetic field can bend particles outside the clustering cone.

3) Particles that shower in boundary regions of the calorimeter (the ϕ boundaries between modules in the central calorimeter and η boundaries between the central and plug calorimeters and between the plug and forward calorimeters) have a smaller observed energy than for regions of uniform response.

4) Energy not associated with hard-scattering process (the so-called "underlying event") is collected within the clustering cone.

5) Transverse spreading of the jet due to fragmentation effects causes particles to be lost outside the cluster cone.

6) Neutrinos and muons in a jet deposit either zero or some small fraction of their energy in the calorimeter.

The calorimeter response function is a map of the calorimeter uniformity for the jet energy and the calorimeter pseudorapidity η_d which is calculated taking the geometric center of the detector as the origin.

The response map of the central calorimeter to jets is determined first, which is described in the following subsection. The central response map is then extended into other regions of the detector, where charged-particle momentum determination with CTC is not available, using a technique where the E_{T} of jets in the central calorimeter is required to balance the E_{T} of jets in the plug and forward calorimeters. Figure 3.5 shows the jet response map as a function of η_d. Since the response uniformity at the η boundaries between calorimeters is significantly degraded as shown in the figure, we measure the two jet cross section as a function of E_{T} of the central jet ($0.1 < \eta < 0.7$) while another jet is binned in four η regions in $0.1 < \eta < 3.0$, as described in Section 3.1.3.

In the following subsection we describe the determination of the response function of the central calorimeter only, which is used to correct the cross section smeared by finite calorimeter E_{T} resolution.

3.3.2 Central jet response function

The response to single particles in the central calorimeter has been determined from test beam measurements ($7 < p_{\mathrm{T}} < 227$ GeV/c), and CTC measurements for isolated tracks in low-energy region ($0.4 < p_{\mathrm{T}} < 12$ GeV/c). A Monte Carlo simulation SIMJET+SETPRT, based on the ISAJET program and Field-Feynman [50] jet fragmentation tuned to the CDF data [51], is used to determine detector response functions. A trial true ("unsmeared") spectrum is smeared with detector effects and compared to the real data. The simulated data have been processed through the jet clustering algorithm in the same way as for the real data.

True jet $E_{\rm T}$ is defined as the sum of the $E_{\rm T}$'s of the final state particles at production given by the SIMJET+SETPRT program. The distribution of $E_{\rm T}$ with the detector smearing, $E_{\rm T}^{measured}$, is parameterized as a function of true jet $E_{\rm T}$, $E_{\rm T}^{true}$, with 4 parameters: offset of the average measured $E_{\rm T}$ $(MEAN)$, gaussian resolution $(SIGMA)$, and downward- and upward-going exponential tails $(SLP1, SLP2)$, respectively. Here the offset $Mean$ accounts for degradation of the calorimeter response including the energy escaping the jet cone and that added by the underlying event (events associated with soft interactions of spectator partons, see Section 3.4 for details).

The $E_{\rm T}^{ture}[GeV]$ dependence of the four parameters is modeled by (Fig. 3.6):

$$
\begin{aligned}
Mean &= 0.240 + 0.788E_{\rm T}^{true} + (9.831\times10^{-4})(E_{\rm T}^{true})^2 - (3.573\times10^{-6})(E_{\rm T}^{true})^3 \\
&\quad +(4.103\times10^{-9})(E_{\rm T}^{true})^4 \qquad (E_{\rm T}^{true} > 14.5\text{GeV}), \quad (3.3)\\
&= 1.802 + 0.597E_{\rm T}^{true} + (6.69\times10^{-3})(E_{\rm T}^{true})^2 \quad (E_{\rm T}^{true} < 14.5\text{GeV}), \quad (3.4)\\
Sigma &= 1.039 + 0.320\sqrt{E_{\rm T}^{true}} + 0.0264E_{\rm T}^{true} - 3.934/E_{\rm T}^{true}, \quad (3.5)\\
SLP1 &= 1.435 + 0.01576E_{\rm T}^{true} - (1.611\times10^{-5})(E_{\rm T}^{true})^2, \quad (3.6)\\
SLP2 &= 0.605 - 0.05046E_{\rm T}^{true} - (6.378\times10^{-5})(E_{\rm T}^{true})^2. \quad (3.7)
\end{aligned}
$$

For presentational purposes the ratio of measured to true $E_{\rm T}$ is plotted in Fig. 3.7 for $E_{\rm T}^{ture}$'s of 10, 50, and 150 GeV. The gaussian part of the resolution improves with increasing $E_{\rm T}$. Energy lost into uninstrumented regions of the detector generates the downward tail. The underlying event energy in the jet cone produces the upward tail. At low $E_{\rm T}$ the upward tail is prominent, as the contribution from the underlying event is large. At high $E_{\rm T}$ the downward tail is clearly distinguishable from the gaussian part of the resolution. At 50 GeV the two tails are of approximately equal size.

Technically, the response distribution is constructed by convoluting a gaussian with upward and downward exponentials, originating at $-(SLP1 + SLP2)/2$. The probability of measuring any particular $E_{\rm T}$, $E_{\rm T}^{measured}$, is given by:

$$
\begin{aligned}
& Res(E_{\mathrm{T}}^{true}, E_{\mathrm{T}}^{measured}) \\
= \; & \frac{1}{2\sqrt{2\pi} \cdot Sigma \cdot SLP1} \int_{-\frac{SLP1+SLP2}{2}}^{\infty} e^{-\frac{X+\frac{SLP1+SLP2}{2}}{SLP1}} e^{-\frac{1}{2}(\frac{E_{\mathrm{T}}^{measured}-Mean-X}{Sigma})^2} dX \\
- \; & \frac{1}{2\sqrt{2\pi} \cdot Sigma \cdot SLP2} \int_{-\infty}^{-\frac{SLP1+SLP2}{2}} e^{-\frac{X+\frac{SLP1+SLP2}{2}}{SLP2}} e^{-\frac{1}{2}(\frac{E_{\mathrm{T}}^{measured}-Mean-X}{Sigma})^2} dX
\end{aligned}
\tag{3.8}
$$

The expectation value of $E_{\mathrm{T}}^{measured}$ with the above distribution is $Mean$ which is a function of E_{T}^{true}. In deriving the unsmeared cross section, the jet finding efficiency has to be included in addition, which rises monotonically from 75% at true E_{T} of 5 GeV through 90% at 10 GeV, and reaches 100% at 20 GeV.

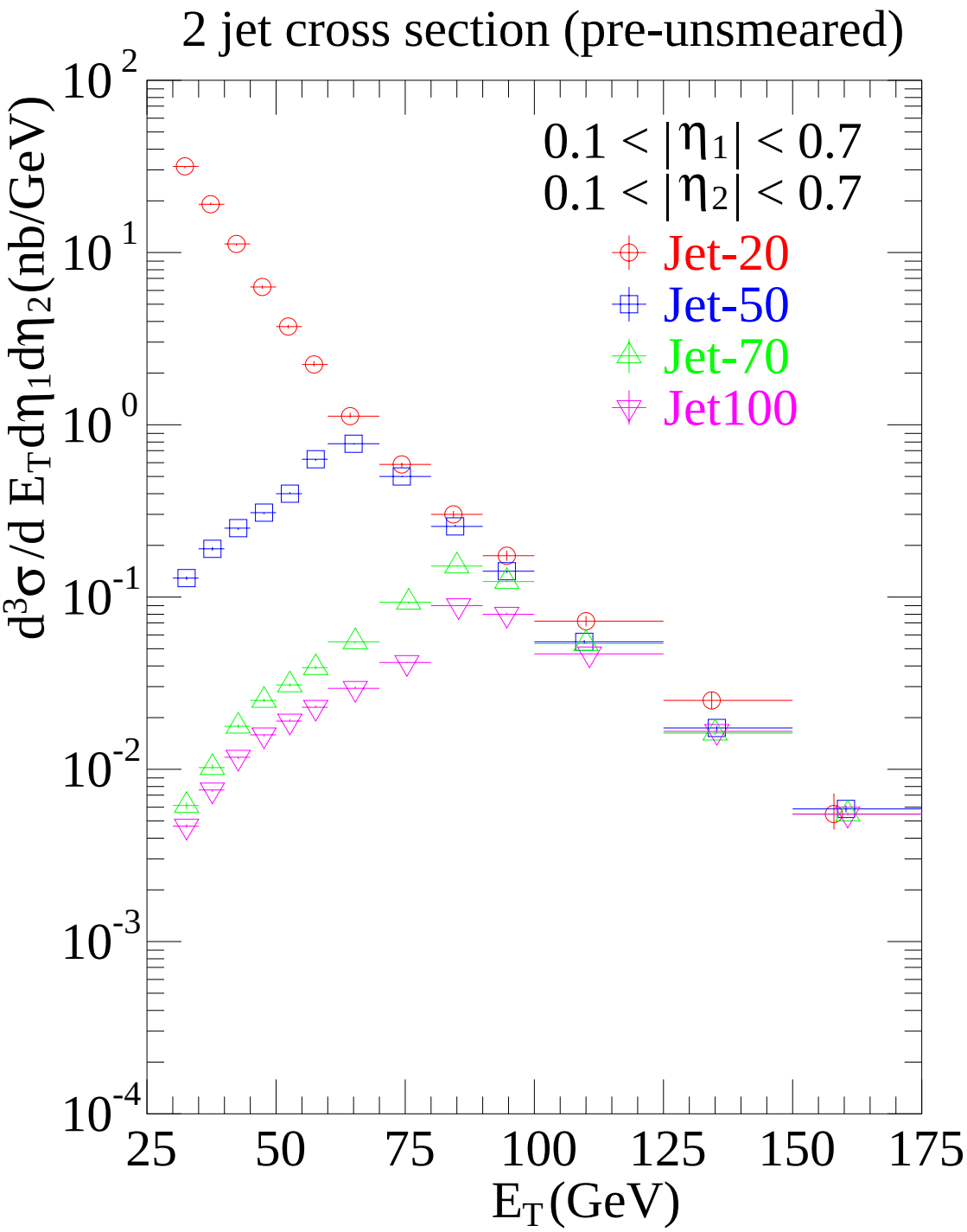

Figure 3.4: Measured two jet cross section for $0.1 < |\eta_1| < 0.7$ and $0.1 < |\eta_2| < 0.7$ as a function of the measured E_{T} (pre-unsmearing) taken from either Jet20, Jet50, Jet70, or Jet100 trigger. The cross section does not correct the trigger inefficiency.

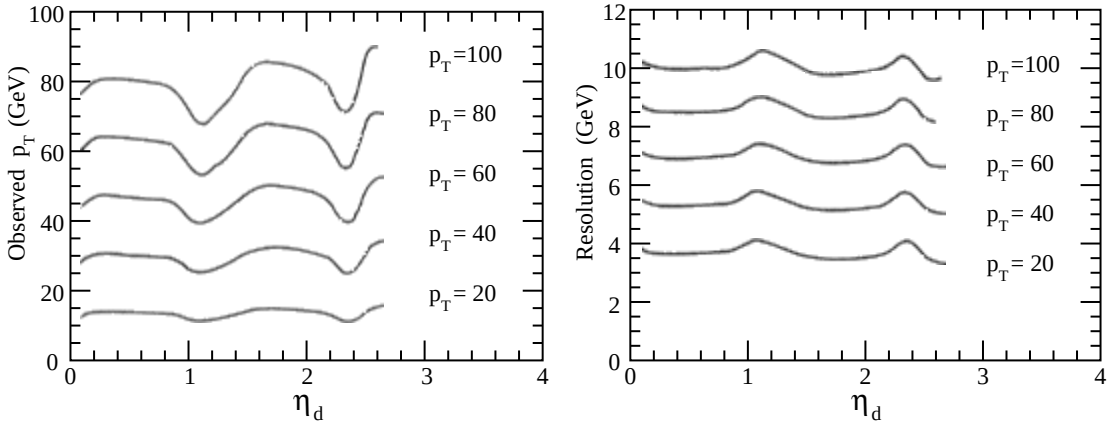

Figure 3.5: Parameterization of the jet response map as a function of the detector pseudorapidity η_d for different slices of jet p_{T}.

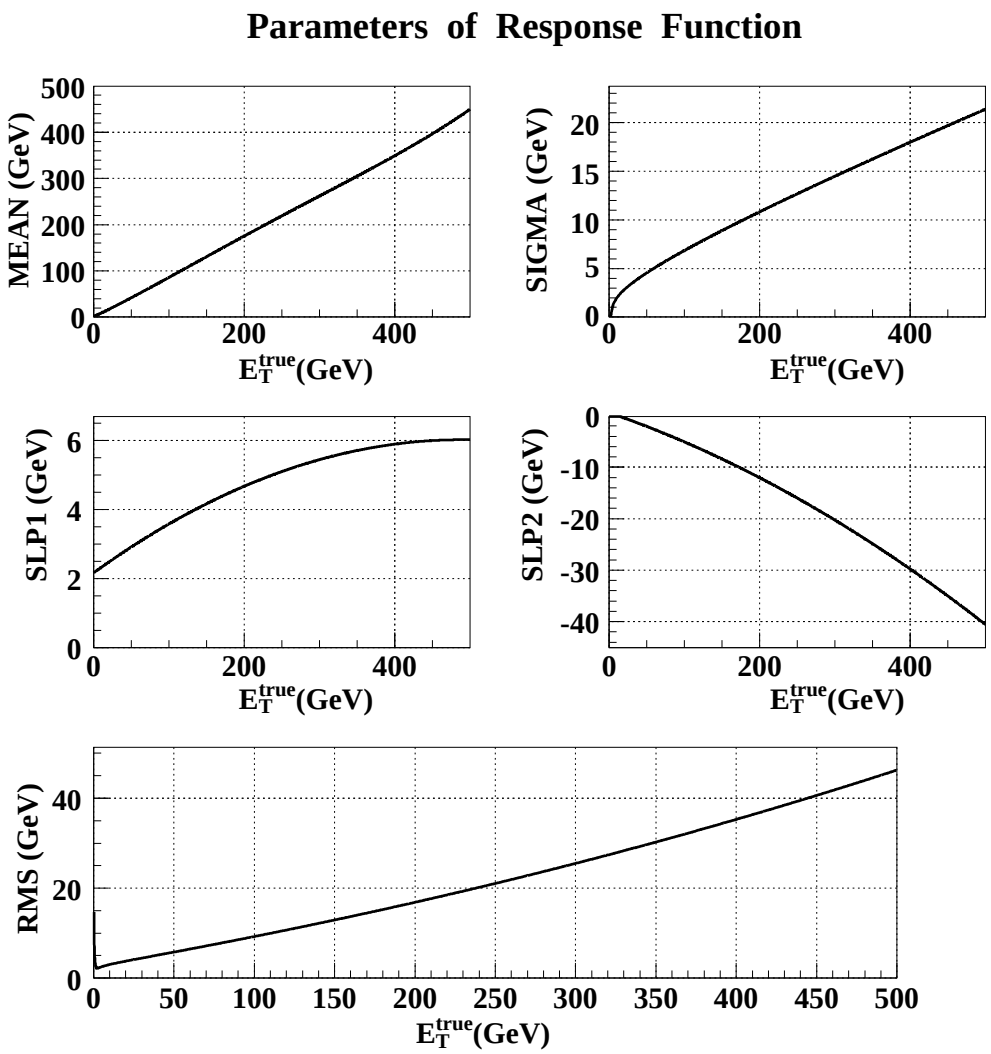

Figure 3.6: The Parameters of the jet response function. The RMS is defined as $(SIGMA^2 + SLP1^2 + SLP2^2)^{1/2}$.

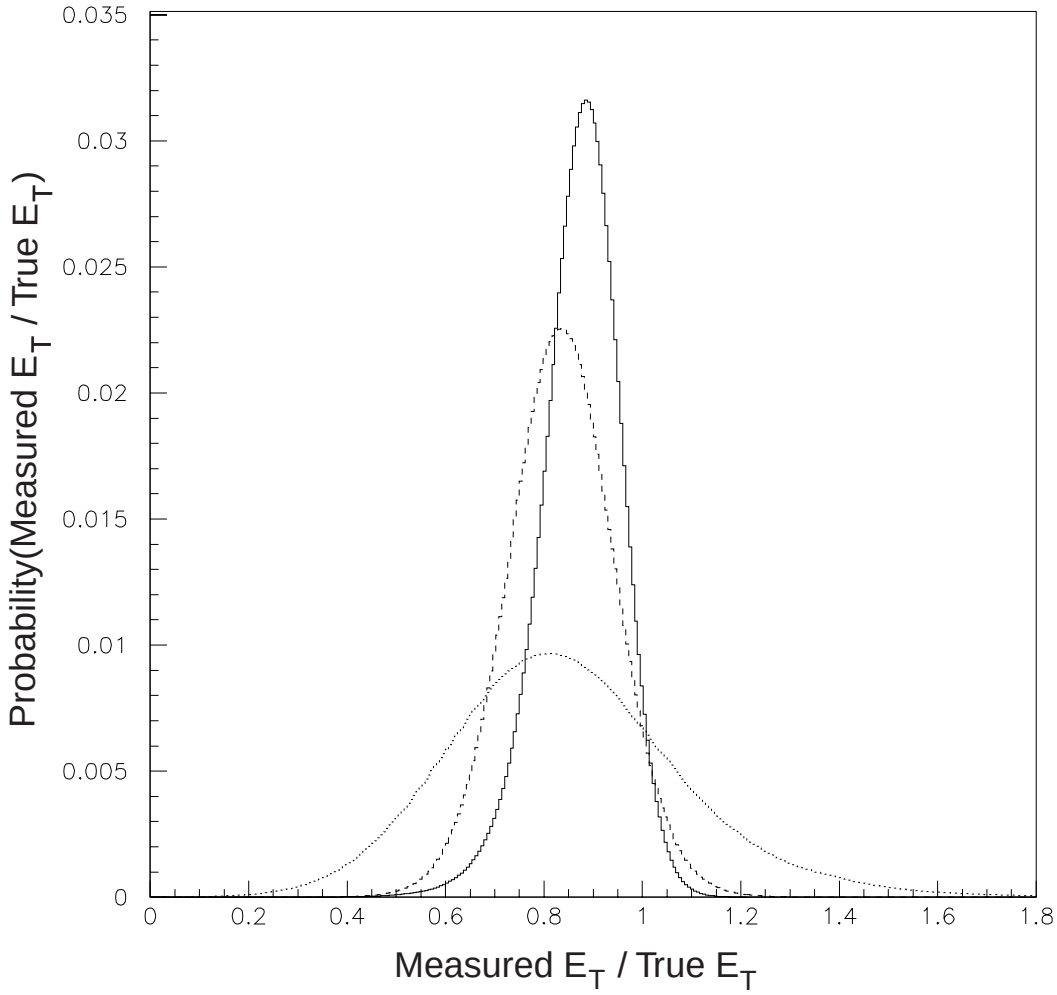

Figure 3.7: The ratio of measured to true jet E_{T} for jets with a true E_{T} of 10 GeV (dotted), 50 GeV (dashed), and 200 GeV (solid). The measured E_{T} is smeared by a parameterization of the detector response.

3.3.3 Two jet production cross section

The measured differential cross section, $\Delta\sigma^{measured}/\Delta E_{\rm T}$, is related to the unsmeared cross section, $d\sigma(E_{\rm T}^{true})/dE_{\rm T}^{true}$, by the following function:

$$\int_{E_{\rm T}^{Low}}^{E_{\rm T}^{High}} dE_{\rm T} \int_{5}^{600} dE_{\rm T}^{true} \frac{d\sigma(E_{\rm T}^{true})}{dE_{\rm T}^{true}} Res(E_{\rm T}^{true}, E_{\rm T}). \tag{3.9}$$

Here the first integration runs over measured $E_{\rm T}$ in the corresponding bin $\Delta E_{\rm T} = E_{\rm T}^{High} - E_{\rm T}^{Low}$, and the second runs over true $E_{\rm T}$ in the range from 5 GeV to 600 GeV which is wide enough to cover the jet $E_{\rm T}$ we are measuring. The true inclusive jet spectrum is parameterized with a functional form:

$$\frac{d\sigma(dE_{\rm T}^{true})}{dE_{\rm T}^{true}} = P_0(1 - x_{\rm T})^{P_6} \times 10^{F(E_{\rm T}^{true})}, \tag{3.10}$$

where

$$x_{\rm T} = \frac{2E_{\rm T}^{true}}{\sqrt{s}} \quad \text{and} \quad F(x) = \sum_{i=1}^{5} P_i \left[log_{10}(x)\right]^i \tag{3.11}$$

with $P_0, \ldots, P_6$ to be determined from a χ^2 minimization using Eq.(3.9). By this χ^2 minimization, we obtain the best match between the smeared trial spectrum and the measured one in the $E_{\rm T}$ range from 40 to 450 GeV.

The fit results in the two jet production cross sections are listed in Table 3.2. The $E_{\rm T}$ in the first column of the table is the smeared value, and the true $E_{\rm T}$ values corresponding to this smeared $E_{\rm T}$ range are given in the same table. The true $E_{\rm T}$ values are the $E_{\rm T}$ range actually used in integrating the true cross section function. Here, only the statistical uncertainties determined from the number of events are quoted. They are plotted in Fig. 3.8 where smooth curves are functions given in Eq.(3.10). The best-fit set of parameters for Eq.(3.10) are listed in Table 3.3 for four different η_2 bins. Also shown in the table are the parameters when one of the systematic uncertainty sources is changed by one standard deviation. The origins of the systematic uncertainties on the response function are explained in the following Section.

Table 3.2: Two jet cross sections as a function of the central jet E_{T}. Cross sections are listed for four η regions of the *second* jet with the central jet in $0.1 < |\eta| < 0.7$. $E_{\mathrm{T}}^{measured}$ is the measured E_{T} (pre-unsmearing). E_{T}^{*Low}, $<E_{\mathrm{T}}^{*}>$, and E_{T}^{*High} are the unsmeared values. The cross sections are divided by the $E_{\mathrm{T}}^{measured}$ bin width and η_1 and η_2 bin widths.

$E_{\mathrm{T}}^{measured}$	Nevts	Trig eff.	E_{T}^{*Low}	$<E_{\mathrm{T}}^{*}>$	E_{T}^{*High}	nb/GeV	stat.unc.
$0.1<\|\eta_2\|<0.7$							
40-45	6416	0.9487	41.43	44.09	47.40	13.5342	1.6897E-1
45-50	3638	0.9768	47.40	50.04	53.26	7.2244	1.1978E-1
50-55	2153	0.9879	53.26	55.88	59.03	4.1399	8.9221E-2
55-60	1302	0.9954	59.03	61.64	64.73	2.4380	6.7567E-2
60-70	1307	0.9983	64.73	69.57	75.99	1.2305	3.4036E-2
70-80	673	1.0000	75.99	80.85	87.10	6.2334E-1	2.4028E-2
80-90	7450	0.9827	87.10	92.00	98.12	2.7504E-1	3.1865E-3
90-100	4015	0.9950	98.12	103.03	109.06	1.4721E-1	2.3233E-3
100-125	19407	0.9777	109.06	119.74	136.20	5.9407E-2	4.2644E-4
125-150	46304	1.0000	136.20	147.23	163.20	1.7673E-2	8.2130E-5
150-175	15537	1.0000	163.20	174.48	190.15	5.8725E-3	4.7113E-5
175-225	8675	1.0000	190.15	209.54	244.08	1.7776E-3	1.9086E-5
225-275	1618	1.0000	244.08	263.98	297.80	3.3677E-4	8.3724E-6
275-325	300	1.0000	297.80	317.52	350.51	6.6527E-5	3.8409E-6
325-450	86	1.0000	350.51	379.36	470.50	1.2998E-5	1.4016E-6
$0.7<\|\eta_2\|<1.4$							
40-45	6376	0.9337	41.88	44.45	47.63	11.4438	1.4332E-1
45-50	3672	0.9624	47.63	50.21	53.35	6.3004	1.0397E-1
50-55	2190	0.9869	53.35	55.93	59.03	3.6215	7.7386E-3
55-60	1309	0.9957	59.03	61.61	64.67	2.1263	5.8769E-2
60-70	1359	0.9982	64.67	69.44	75.83	1.1132	3.0197E-2
70-80	599	1.0000	75.83	80.64	86.87	4.8369E-1	1.9763E-2
80-90	6928	0.9794	86.87	91.71	97.82	2.3430E-1	2.8150E-3
90-100	3681	0.9559	97.82	102.68	108.69	1.2014E-1	1.9801E-3
100-125	16608	0.9652	108.69	119.11	135.64	4.7659E-2	3.6981E-4
125-150	36689	1.0000	135.64	146.35	162.37	1.2504E-2	6.5280E-5
150-175	11588	1.0000	162.37	173.26	188.98	3.9479E-3	3.6674E-5
175-225	5274	1.0000	188.98	207.02	241.98	1.0190E-3	1.4032E-5
225-275	698	1.0000	241.98	260.13	294.51	1.4244E-4	5.3914E-6
275-325	95	1.0000	294.51	312.16	345.92	2.1733E-5	2.2297E-6
325-450	22	1.0000	345.92	368.34	463.61	4.2423E-6	9.0446E-7

Table 3.2: (Continued).

$E_{\mathrm{T}}^{measured}$	Nevts	Trig eff.	E_{T}^{*Low}	$<E_{\mathrm{T}}^{*}>$	E_{T}^{*High}	nb/GeV	stat.unc.
$1.4<\|\eta_2\|<2.1$							
40-45	5366	0.9050	40.93	43.54	46.86	10.8552	1.4819E-1
45-50	2941	0.9608	46.86	49.45	52.68	5.4248	1.0003E-1
50-55	1658	0.9815	52.68	55.25	58.40	2.9315	7.1993E-2
55-60	999	0.9947	58.40	60.95	64.04	1.7106	5.4122E-2
60-70	974	0.9988	64.04	68.71	75.14	8.4664E-1	2.7128E-2
70-80	393	1.0000	75.14	79.82	86.06	3.3824E-1	1.7062E-2
80-90	3984	0.9665	86.06	90.74	96.85	1.3779E-1	2.1830E-3
90-100	1887	0.9857	96.85	101.54	107.54	6.5433E-2	1.5063E-3
100-125	7660	0.9618	107.54	117.18	133.91	2.3402E-2	2.6739E-4
125-150	11636	1.0000	133.91	143.70	159.95	4.5785E-3	4.2445E-5
150-175	2521	1.0000	159.95	169.81	185.77	1.0210E-3	2.0335E-5
175-225	779	1.0000	185.77	200.62	237.03	2.0320E-4	7.2804E-6
225-275	40	1.0000	237.03	251.69	287.80	1.1965E-5	1.8919E-6
275-325	2	1.0000	287.80	301.94	337.70	7.3376E-7	5.1884E-7
$2.1<\|\eta_2\|<3.0$							
40-45	2689	0.9233	40.17	42.62	45.84	4.7624	9.1838E-2
45-50	1367	0.9617	45.84	48.28	51.45	2.2866	6.1845E-2
50-55	651	0.9856	51.45	53.88	56.99	1.0519	4.1228E-2
55-60	365	0.9762	56.99	59.41	62.46	5.7854E-1	3.0282E-2
60-70	281	1.0000	62.46	66.78	73.24	2.3223E-1	1.3854E-2
70-80	104	1.0000	73.24	77.56	83.85	8.6263E-2	8.4588E-3
80-90	708	0.9032	83.85	88.16	94.32	2.3931E-2	8.9939E-4
90-100	275	1.0000	94.32	98.63	104.68	9.4580E-3	5.7034E-4
100-125	692	0.9515	104.68	112.79	130.20	2.3212E-3	8.8238E-5
125-150	549	1.0000	130.20	138.40	155.33	2.4732E-4	1.0555E-5
150-175	48	1.0000	155.33	163.56	180.19	2.3399E-5	3.3773E-6
175-225	10	1.0000	180.19	190.97	229.36	3.9080E-6	1.2358E-6

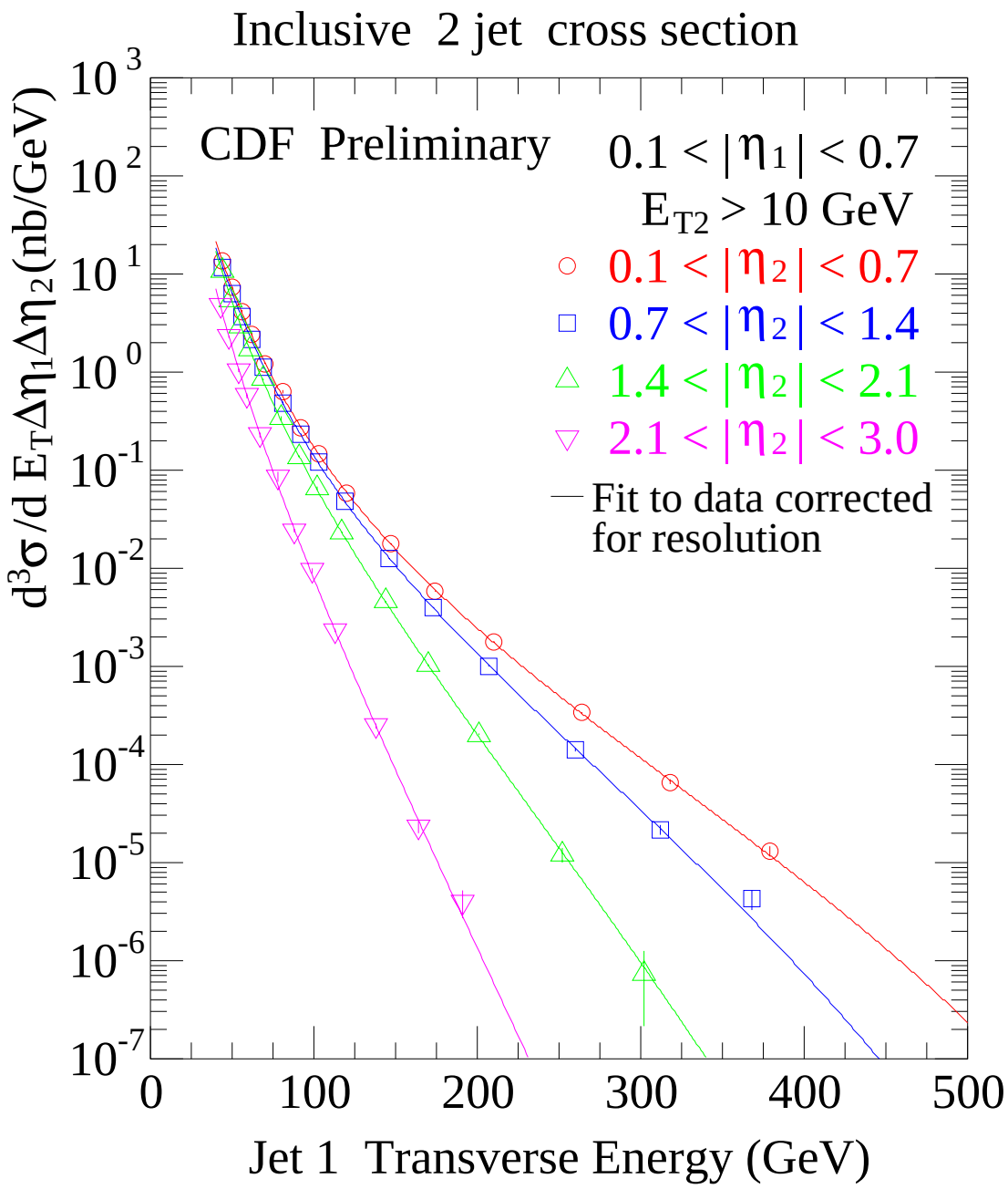

Figure 3.8: Cross section for two jet production as a function of the central ($0.1 < |\eta_1| < 0.7$) jet E_{T} (unsmeared). The unsmeared data (listed in column 7 in Table 3.2) are shown for four different η bins of the other most energetic jets. The uncertainties are statistical only. The unsmeared physics functions fitted to the data are given in text.

3.4 Systematic Uncertainties

Systematic uncertainties of the cross sections originating from the unsmearing procedure are listed as follows:

1) Electron/photon response uncertainty.

   The response calibration to electrons was performed using the 1990 test beam data in the energy range from 5 to 150 GeV. The energy scale calibration of the CEM and CHA calorimeter towers was made at 50 GeV electrons and pions. The response ratio of electrons to pions E/P exhibits a deviation of -2% at $\sim$ 10 GeV and $+2\%$ at $\sim$ 5 GeV [52]. Note that the CEM response is assumed to be linear in this energy range since the absolute momentum calibration of the test beam is not well understood. The *in situ* studies using the CTC information are available. The study for W mass measurements in the energy 25 GeV and above, for example, shows a smaller uncertainty [53]. We conservatively assign $\pm 2\%$ for this uncertainty in the whole energy range and assume the response to photons is identical with that to electrons.

2) Uncertainty in underlying event energy.

   The term "underlying event" refers to a collection of relatively low p_{T} particles arising from interactions between spectator partons. These particles can contribute a small amount of additional energy to the jet cone. Underlying event energy density has been studied in dijet events at angles near perpendicular to the thrust axis. For the 1994-95 collider run the E_{T} density of the underlying event has been measured to be 2.06 GeV per pseudorapidity (η) per azimuth (ϕ). The systematic uncertainty is evaluated by changing the angle window ($\Delta\phi = 10^\circ$ and 20°) for calculating the E_{T} flow and the E_{T} cut (0, 5, and 15 GeV) for the third jet. We assign $\pm 30\%$ [54] for this systematic uncertainty.

3) Parton fragmentation function uncertainty.

   The uncertainty [51] in jet fragmentation properties (the ratio between electromagnetic and hadronic components, and the energy spectra) introduces the

uncertainty in the parton energy evaluation because of the different energy resolutions for the two components and of the response nonlinearity for the hadronic component. It is important to tune the SIMJET+SETPRT Monte Carlo programs to reproduce the observed fragmentation properties. The uncertainty in track finding efficiency affects the uncertainty on the fragmentation tuning. The uncertainty in the efficiency of finding tracks in jets is found to be $\pm 7\%$.

4) Uncertainty in jet energy resolution.

The uncertainty in jet energy resolution is evaluated by comparing E_{T} balance for Monte Carlo calculations and real data in dijet events and in γ-jet events. We define k_{T} as the vector sum of the transverse momentum in dijet events or in γ-jet events. The resolution of the k_{T} vector projected along the bisector of the two E_{T}'s, $k_{\mathrm{T}\|}$, is primarily determined by the angular resolution of the jet direction. The resolution of the k_{T} vector perpendicular to the bisector, $k_{\mathrm{T}\perp}$, is determined by the jet energy resolution in addition. Hence the jet E_{T} resolution $\sigma(E_{\mathrm{T}})$ can be derived from the distributions of these two quantities: $\sigma(E_{\mathrm{T}}) = \sqrt{\sigma^2(k_{\mathrm{T}\|}) - \sigma^2(k_{\mathrm{T}\perp})}/\sqrt{2}$. The jet E_{T} resolution is studied in the energy range from 40 to 180 GeV in dijet events and from 27 to 60 GeV in γ-jet events. The jet E_{T} resolution is typically 10% and its uncertainty, difference between Monte Carlo calculations and real data, is $\pm 10\%$ [55].

5) Uncertainty on Calorimeter response to low p_{T} pions.

The response to pions has been measured in test beams and *in situ* using the CTC information in the energy $\sim$ 10 GeV and below. Figure 3.9 shows the measured calorimeter response to charged hadrons as a function of incident momentum for particles hitting the center of a calorimeter tower. The figure also indicates the size of the systematic uncertainty associated with this measurement. Note that the measured response deviates substantially from linearity for low incident energy. The uncertainty is typically $\sim \pm 5\%$.

6) Pion response uncertainty at high p_{T} .

The response to high p_{T} pions was determined using the test beam calibration in p_{T} below 227 GeV, as shown in Fig. 3.9. The uncertainty to pion response above 15 GeV is dominated by understanding the ϕ response near the tower boundaries and the energy scale of the test beam. We assign $\pm^{4.5}_{0}\%$ for the ϕ response uncertainty, which represents the difference between the single-track face-averaged response for the tuned ϕ response and a flat response. For the energy scale of the test beam we assign a $\pm 3\%$ uncertainty to pions of 25 GeV and above, accounting for the possible non-linearity of the CEM electron response. The validity of and uncertainty in the extrapolation to the energy beyond the test beam energy are studied by comparing the CDF jet data with the SIMJET+SETPRT Monte Carlo distributions.

7) Calorimeter energy scale instability.

The energy scale instability has been derived from the CTC information utilizing the momentum-to-energy matching. The whole 1992-93 run were divided into seven periods and the response to single particles in the momentum range from 1 to 3 GeV was traced. The response of the CEM and of CHA was found to be stable within 1%. The mass peak of Z^0 particles was also used to check the instability of the CEM.

8) Functional form of response function.

The response function we used is a gaussian distribution (with an sigma of $SIGMA$) convoluted with two exponential tails (with slope parameters of $SLP1$ and $SLP2$) on either side [see Eq.(3.8)]. This uncertainty is estimated by simplifying it to a single gaussian distribution with an sigma of $(SIGMA^2 + SLP1^2 + SLP2^2)^{1/2}$.

9) Normalization uncertainty.

It is derived from the luminosity measurement uncertainty [49] and Z_{vertex} cut efficiency uncertainty. We conservatively estimate the normalization uncertainty as $\pm 8.0\%$.

Items 1) through 7) can exhibit "negative" and "positive" contributions. The percentage changes of the cross section are listed in Table 3.4 and 3.5, and shown in Fig. 3.10 and 3.11; item 8) is given in Table 3.5. As the overall systematic uncertainty we added the above, including item 9), in quadrature, which is shown in Fig. 3.12.

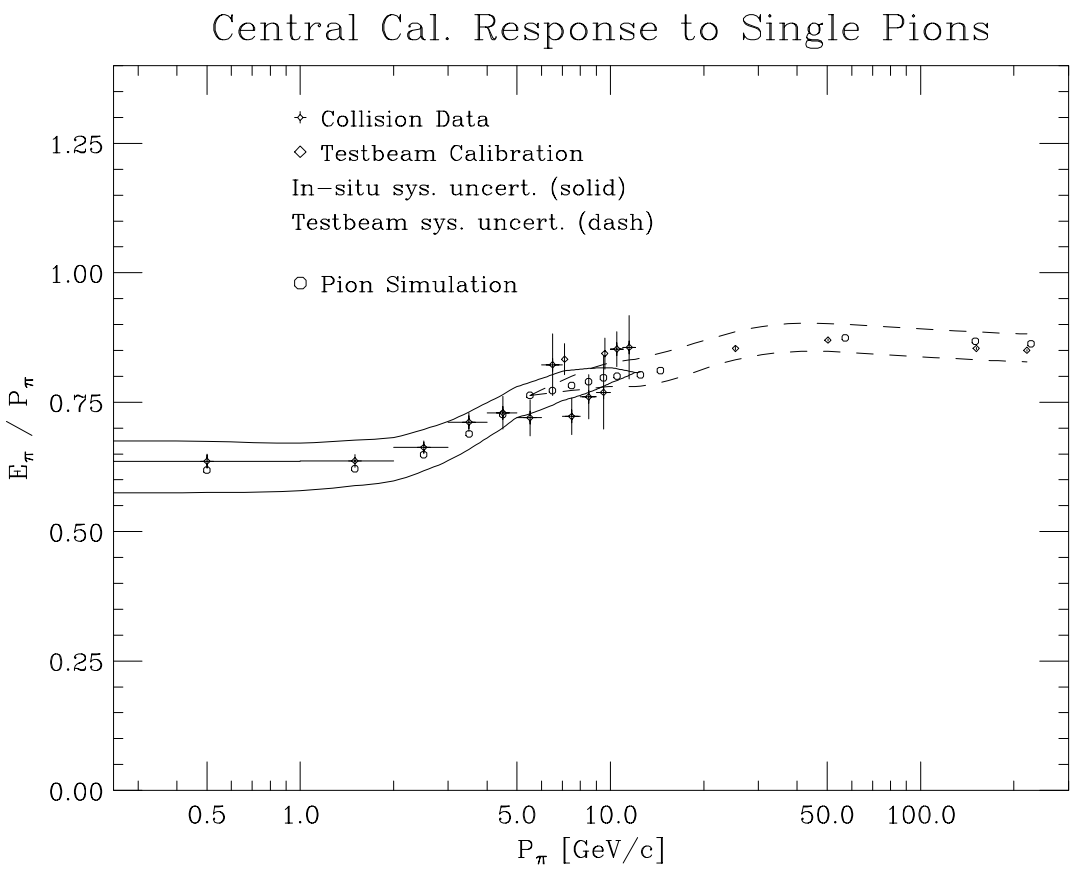

Figure 3.9: CDF central calorimeter response (E/p) to pions as a function of incident momentum. The high energy data are obtained from test beam measurements, and low energy data ($\leq$ 12 GeV) are obtained from isolated tracks in minimum bias events.

Table 3.3: Fitted parameters for the true cross section curves in the region $0.1 < |\eta_1| < 0.7$ and $0.1 < |\eta_2| < 0.7$. Also shown are the parameters when one of the sources of systematic uncertainties is changed by ± 1 standard deviation.

	P_0	P_1	P_2	P_3	P_4	P_5	P_6
$0.1 < \|\eta_2\| < 0.7$							
Standard	6.7533E+5	−2.102	1.538	−1.680	0.287	0.0416	17.037
Electron/γ (+)	6.5744E+5	−2.088	1.539	−1.681	0.287	0.0414	16.823
Electron/γ (−)	6.9811E+5	−2.121	1.538	−1.679	0.288	0.0418	17.305
Underlying (+)	2.9226E+5	−1.916	1.555	−1.683	0.284	0.0398	16.320
Underlying (−)	7.7760E+7	−4.238	1.840	−1.499	0.312	0.0099	13.362
Fragmentation (+)	1.1311E+7	−3.493	1.742	−1.555	0.306	0.0198	15.064
Fragmentation (−)	5.4213E+5	−2.006	1.541	−1.685	0.284	0.0402	15.891
Resolution (+)	5.1478E+5	−2.048	1.544	−1.680	0.287	0.0412	17.033
Resolution (−)	8.4614E+5	−2.146	1.533	−1.680	0.288	0.0419	16.995
Low p_{T} pion (+)	7.5588E+5	−2.167	1.537	−1.676	0.290	0.0426	17.830
Low p_{T} pion (−)	6.0568E+5	−2.041	1.539	−1.683	0.285	0.0406	16.288
High p_{T} pion (+)	6.5782E+5	−2.089	1.537	−1.682	0.286	0.0411	17.008
High p_{T} pion (−)	6.6982E+5	−2.097	1.539	−1.680	0.287	0.0416	16.898
1.0% E scale (+)	7.4455E+5	−2.121	1.537	−1.679	0.288	0.0417	17.050
1.0% E scale (−)	6.7094E+5	−2.111	1.538	−1.680	0.288	0.0417	17.195
Gaussian response	2.5214E+7	−3.786	1.783	−1.534	0.308	0.0164	14.483
$0.7 < \|\eta_2\| < 1.4$							
Standard	7.9423E+1	3.501	−0.651	−1.735	0.443	0.0392	27.069
Electron/γ (+)	7.5377E+1	3.524	−0.651	−1.736	0.442	0.0389	26.741
Electron/γ (−)	8.4949E+1	3.473	−0.652	−1.734	0.444	0.0396	27.489
Underlying (+)	4.2849E+1	3.629	−0.638	−1.737	0.441	0.0381	26.716
Underlying (−)	1.4100E+2	3.383	−0.663	−1.734	0.445	0.0402	27.384
Fragmentation (+)	1.1335E+2	3.364	−0.654	−1.728	0.447	0.0411	28.706
Fragmentation (−)	5.4706E+1	3.645	−0.648	−1.742	0.438	0.0373	25.397
Resolution (+)	7.1334E+1	3.510	−0.647	−1.734	0.443	0.0393	27.481
Resolution (−)	8.7159E+1	3.495	−0.654	−1.736	0.442	0.0391	26.682
Low p_{T} pion (+)	9.7595E+1	3.408	−0.653	−1.730	0.446	0.0405	28.106
Low p_{T} pion (−)	6.5268E+1	3.590	−0.650	−1.740	0.440	0.0380	26.108
High p_{T} pion (+)	7.8626E+1	3.511	−0.652	−1.736	0.442	0.0389	27.368
High p_{T} pion (−)	7.7002E+1	3.513	−0.650	−1.736	0.442	0.0391	26.730
1.0% E scale (+)	8.8124E+1	3.482	−0.652	−1.735	0.443	0.0393	26.967
1.0% E scale (−)	8.7131E+1	3.458	−0.651	−1.733	0.444	0.0398	27.892
Gaussian response	1.1092E+2	3.409	−0.655	−1.731	0.445	0.0403	28.044

Table 3.3: (Continued).

	P_0	P_1	P_2	P_3	P_4	P_5	P_6
$1.4 < \lvert\eta_2\rvert < 2.1$							
Standard	1.7660E+3	3.792	−2.515	−1.281	0.852	−0.1091	30.882
Electron/γ (+)	1.7147E+3	3.810	−2.515	−1.282	0.851	−0.1093	30.492
Electron/γ (−)	1.8327E+3	3.771	−2.514	−1.279	0.853	−0.1089	31.376
Underlying (+)	6.0017E+2	4.056	−2.498	−1.288	0.847	−0.1116	29.500
Underlying (−)	4.5914E+3	3.562	−2.530	−1.275	0.857	−0.1070	32.049
Fragmentation (+)	2.2579E+3	3.686	−2.516	−1.275	0.856	−0.1077	32.413
Fragmentation (−)	1.3275E+3	3.912	−2.513	−1.287	0.848	−0.1107	29.198
Resolution (+)	1.2411E+3	3.868	−2.507	−1.281	0.851	−0.1097	31.087
Resolution (−)	2.3959E+3	3.728	−2.522	−1.281	0.853	−0.1087	30.638
Low p_{T} pion (+)	1.9956E+3	3.723	−2.516	−1.277	0.854	−0.1082	31.744
Low p_{T} pion (−)	1.5527E+3	3.862	−2.514	−1.285	0.850	−0.1101	30.076
High p_{T} pion (+)	1.6974E+3	3.805	−2.512	−1.280	0.852	−0.1096	31.794
High p_{T} pion (−)	1.7735E+3	3.797	−2.516	−1.282	0.852	−0.1091	30.293
1.0% E scale (+)	1.6695E+3	3.820	−2.514	−1.282	0.851	−0.1094	30.406
1.0% E scale (−)	3.6786E+3	3.534	−2.516	−1.266	0.861	−0.1058	34.590
Gaussian response	4.5428E+3	3.506	−2.521	−1.267	0.861	−0.1056	34.355
$2.1 < \eta_2 < 3.0$							
Standard	4.1545E+2	3.719	−1.883	−1.402	0.792	−0.1116	42.894
Electron/γ (+)	4.0415E+2	3.734	−1.883	−1.403	0.792	−0.1117	42.470
Electron/γ (−)	4.3304E+2	3.700	−1.883	−1.401	0.793	−0.1113	43.534
Underlying (+)	1.7984E+2	3.895	−1.866	−1.405	0.789	−0.1131	42.412
Underlying (−)	1.0965E+3	3.483	−1.895	−1.394	0.798	−0.1095	44.324
Fragmentation (+)	4.4957E+2	3.679	−1.888	−1.402	0.793	−0.1111	43.267
Fragmentation (−)	3.7869E+2	3.766	−1.878	−1.402	0.792	−0.1121	42.505
Resolution (+)	3.3483E+2	3.748	−1.874	−1.399	0.793	−0.1117	43.961
Resolution (−)	5.4428E+2	3.665	−1.889	−1.402	0.793	−0.1114	42.228
Low p_{T} pion (+)	4.8135E+2	3.647	−1.886	−1.399	0.794	−0.1109	43.411
Low p_{T} pion (−)	3.6436E+2	3.785	−1.880	−1.404	0.791	−0.1123	42.538
High p_{T} pion (+)	4.1377E+2	3.720	−1.876	−1.399	0.793	−0.1119	44.909
High p_{T} pion (−)	4.1276E+2	3.725	−1.884	−1.403	0.792	−0.1116	41.852
1.0% E scale (+)	6.9171E-13	23.536	−6.329	−3.296	0.764	0.3655	173.640
1.0% E scale (−)	1.7157E-10	20.496	−5.734	−3.003	0.782	0.2971	158.253
Gaussian response	1.0258E+3	3.424	−1.876	−1.381	0.802	−0.1086	47.612

Table 3.4: The percentage change in the cross section from various "negative" systematic contributions. The "All" values are systematic uncertainties of all contributions (see text) added in quadrature.

$E_{\mathrm{T}}^{measured}$	e/γ	UE	Frag.	Estab.	Res'n	π_{low}	π^{TB}	All
$0.1<\|\eta_2\|<0.7$								
40-45	−2.74	−11.98	−7.77	−3.83	−5.20	−7.37	−2.55	−19.44
45-50	−2.83	−10.57	−8.36	−3.92	−4.68	−7.37	−3.01	−18.82
50-55	−2.89	−9.41	−8.62	−4.00	−4.25	−7.32	−3.46	−18.30
55-60	−2.95	−8.45	−8.68	−4.08	−3.90	−7.24	−3.89	−17.85
60-70	−3.01	−7.38	−8.57	−4.17	−3.50	−7.08	−4.48	−17.34
70-80	−3.08	−6.18	−8.26	−4.29	−3.06	−6.82	−5.30	−16.80
80-90	−3.14	−5.29	−7.90	−4.41	−2.74	−6.53	−6.08	−16.45
90-100	−3.19	−4.63	−7.56	−4.52	−2.50	−6.23	−6.83	−16.27
100-125	−3.27	−3.95	−7.17	−4.68	−2.28	−5.81	−7.91	−16.28
125-150	−3.42	−3.28	−6.88	−4.96	−2.12	−5.19	−9.58	−16.78
150-175	−3.61	−2.96	−6.99	−5.25	−2.15	−4.74	−11.12	−17.69
175-225	−3.94	−2.78	−7.55	−5.67	−2.36	−4.46	−12.93	−19.22
225-275	−4.62	−2.53	−8.71	−6.39	−2.89	−4.67	−15.47	−21.94
275-325	−5.54	−1.98	−9.58	−7.21	−3.57	−5.73	−17.69	−24.60
325-450	−6.97	−0.55	−9.31	−8.36	−4.46	−8.18	−19.99	−27.49
$0.7<\|\eta_2\|<1.4$								
40-45	−2.68	−10.83	−7.39	−3.99	−4.46	−7.21	−2.51	−18.36
45-50	−2.81	−9.77	−7.72	−4.12	−4.18	−7.32	−3.00	−18.00
50-55	−2.91	−8.89	−7.94	−4.23	−3.94	−7.36	−3.48	−17.72
55-60	−2.99	−8.14	−8.07	−4.31	−3.73	−7.34	−3.96	−17.50
60-70	−3.09	−7.28	−8.16	−4.41	−3.47	−7.26	−4.61	−17.28
70-80	−3.20	−6.29	−8.17	−4.53	−3.18	−7.07	−5.52	−17.08
80-90	−3.30	−5.54	−8.10	−4.65	−2.96	−6.83	−6.41	−17.01
90-100	−3.38	−4.97	−7.99	−4.77	−2.79	−6.58	−7.28	−17.05
100-125	−3.52	−4.35	−7.84	−4.99	−2.64	−6.21	−8.55	−17.33
125-150	−3.77	−3.69	−7.69	−5.45	−2.57	−5.67	−10.60	−18.21
150-175	−4.09	−3.34	−7.78	−6.06	−2.70	−5.31	−12.56	−19.55
175-225	−4.59	−3.14	−8.36	−7.09	−3.11	−5.20	−14.94	−21.81
225-275	−5.65	−3.04	−10.32	−9.22	−4.18	−5.78	−18.56	−26.42
275-325	−7.04	−2.94	−13.60	−11.96	−5.71	−7.33	−22.00	−32.32
325-450	−9.00	−2.62	−18.77	−15.73	−7.91	−10.26	−25.71	−40.67

Table 3.4: (Continued)

$E_{\mathrm{T}}^{measured}$	e/γ	UE	Frag.	Estab.	Res'n	π_{low}	π^{TB}	All
$1.4<\|\eta_2\|<2.1$								
40-45	−2.97	−13.27	−8.18	−4.24	−6.09	−7.96	−2.80	−21.02
45-50	−3.10	−11.71	−8.49	−4.84	−5.51	−8.05	−3.32	−20.30
50-55	−3.21	−10.46	−8.71	−5.22	−5.05	−8.08	−3.86	−19.82
55-60	−3.31	−9.46	−8.86	−5.47	−4.69	−8.08	−4.42	−19.49
60-70	−3.44	−8.39	−9.01	−5.65	−4.33	−8.03	−5.20	−19.22
70-80	−3.62	−7.24	−9.15	−5.75	−3.98	−7.91	−6.37	−19.12
80-90	−3.81	−6.45	−9.24	−5.77	−3.80	−7.77	−7.56	−19.26
90-100	−3.99	−5.90	−9.32	−5.78	−3.74	−7.63	−8.76	−19.60
100-125	−4.29	−5.41	−9.45	−5.89	−3.82	−7.43	−10.54	−20.41
125-150	−4.85	−4.98	−9.81	−6.44	−4.24	−7.18	−13.60	−22.46
150-175	−5.48	−4.81	−10.39	−7.60	−4.92	−7.08	−16.65	−25.21
175-225	−6.36	−4.65	−11.45	−9.92	−5.95	−7.19	−20.28	−29.39
225-275	−8.08	−4.05	−14.02	−15.75	−7.98	−7.94	−26.27	−38.44
275-325	−10.11	−2.66	−17.60	−23.73	−10.25	−9.40	−32.12	−50.25
$2.1<\|\eta_2\|<3.0$								
40-45	−3.40	−15.65	−9.31	−2.23	−7.70	−9.07	−3.25	−23.76
45-50	−3.65	−14.40	−9.84	−3.23	−7.41	−9.40	−4.02	−23.48
50-55	−3.88	−13.36	−10.29	−4.73	−7.21	−9.65	−4.83	−23.54
55-60	−4.10	−12.51	−10.69	−6.19	−7.08	−9.84	−5.66	−23.85
60-70	−4.37	−11.58	−11.16	−7.66	−6.99	−10.02	−6.80	−24.41
70-80	−4.76	−10.53	−11.75	−8.76	−7.00	−10.20	−8.55	−25.27
80-90	−5.14	−9.77	−12.26	−8.72	−7.16	−10.30	−10.34	−26.01
90-100	−5.52	−9.24	−12.71	−7.99	−7.42	−10.35	−12.14	−26.74
100-125	−6.04	−8.76	−13.25	−6.77	−7.94	−10.37	−14.65	−28.00
125-150	−7.03	−8.33	−14.11	−6.84	−9.21	−10.35	−19.26	−31.51
150-175	−8.06	−8.28	−14.87	−13.57	−10.79	−10.31	−23.84	−37.56
175-225	−9.30	−8.46	−15.67	−30.41	−12.84	−10.31	−28.87	−52.27

Table 3.5: The percentage change in the cross section from various "positive" systematic contributions and from uncertainty in the functional form of the calorimeter response function. The "All" values are systematic uncertainties of all contributions (see text) added in quadrature.

$E_{\mathrm{T}}^{measured}$	e/γ	UE	Frag.	Estab.	Res'n	π_{low}	π^{TB}	Gauss	All
$0.1<\|\eta_2\|<0.7$									
40-45	2.24	12.96	8.28	4.21	4.90	7.18	2.77	3.65	20.49
45-50	2.31	10.44	8.52	4.18	4.41	7.16	3.01	2.28	18.80
50-55	2.37	8.76	8.65	4.18	4.01	7.08	3.24	1.45	17.81
55-60	2.42	7.59	8.70	4.19	3.67	6.96	3.46	0.93	17.19
60-70	2.47	6.53	8.70	4.23	3.30	6.75	3.75	0.56	16.65
70-80	2.53	5.58	8.60	4.31	2.89	6.41	4.14	0.35	16.15
80-90	2.57	5.02	8.44	4.42	2.58	6.05	4.51	0.34	15.82
90-100	2.62	4.65	8.25	4.54	2.36	5.70	4.87	0.38	15.59
100-125	2.69	4.22	7.97	4.75	2.15	5.18	5.40	0.42	15.36
125-150	2.81	3.59	7.62	5.12	1.98	4.44	6.24	0.30	15.22
150-175	2.97	2.94	7.48	5.51	2.00	3.88	7.07	-0.07	15.39
175-225	3.25	2.22	7.72	6.02	2.19	3.48	8.14	-0.78	16.08
225-275	3.83	1.83	9.07	6.81	2.72	3.54	9.82	-1.82	18.09
275-325	4.63	3.19	11.76	7.56	3.44	4.49	11.55	-2.05	21.37
325-450	5.91	8.79	17.15	8.40	4.45	6.98	13.75	-0.14	28.26
$0.7<\|\eta_2\|<1.4$									
40-45	2.19	11.52	8.04	4.34	4.22	7.00	2.71	2.40	19.10
45-50	2.29	10.30	8.45	4.31	3.95	7.09	2.99	1.97	18.55
50-55	2.38	9.31	8.72	4.30	3.72	7.10	3.26	1.64	18.12
55-60	2.45	8.47	8.89	4.32	3.51	7.06	3.51	1.38	17.77
60-70	2.53	7.54	8.99	4.36	3.27	6.92	3.84	1.12	17.37
70-80	2.62	6.48	9.00	4.47	2.99	6.66	4.31	0.85	16.93
80-90	2.71	5.69	8.92	4.61	2.78	6.35	4.75	0.68	16.60
90-100	2.78	5.09	8.79	4.77	2.62	6.02	5.19	0.55	16.37
100-125	2.89	4.45	8.59	5.06	2.48	5.54	5.85	0.40	16.21
125-150	3.11	3.76	8.38	5.59	2.41	4.85	6.94	0.14	16.34
150-175	3.38	3.40	8.46	6.18	2.53	4.36	8.06	-0.20	16.94
175-225	3.81	3.19	9.13	6.98	2.92	4.09	9.54	-0.86	18.36
225-275	4.72	3.07	11.51	8.35	3.97	4.44	12.08	-2.49	21.89
275-325	5.94	2.98	15.77	9.80	5.52	5.85	14.88	-4.90	27.19
325-450	7.73	2.68	23.33	11.53	7.84	8.85	18.42	-8.57	35.88

Table 3.5: (Continued).

$E_{\mathrm{T}}^{measured}$	e/γ	UE	Frag.	Estab.	Res'n	π_{low}	π^{TB}	Gauss	All
$1.4<\|\eta_2\|<2.1$									
40-45	2.43	14.21	8.99	4.32	5.87	7.79	3.03	4.32	22.23
45-50	2.54	12.40	9.40	4.57	5.28	7.86	3.31	3.28	21.09
50-55	2.63	11.00	9.67	4.79	4.83	7.86	3.61	2.55	20.33
55-60	2.72	9.89	9.87	4.99	4.48	7.82	3.91	2.03	19.80
60-70	2.83	8.73	10.05	5.23	4.13	7.71	4.32	1.55	19.34
70-80	2.98	7.49	10.20	5.54	3.79	7.51	4.95	1.13	18.98
80-90	3.14	6.66	10.29	5.84	3.60	7.27	5.59	0.90	18.87
90-100	3.30	6.08	10.37	6.12	3.54	7.03	6.25	0.75	18.93
100-125	3.55	5.56	10.51	6.54	3.61	6.69	7.26	0.55	19.28
125-150	4.03	5.10	10.91	7.27	4.02	6.20	9.09	-0.01	20.38
150-175	4.59	4.92	11.61	8.05	4.70	5.89	11.03	-1.03	22.07
175-225	5.36	4.76	12.98	9.10	5.76	5.77	13.55	-3.09	24.84
225-275	6.91	4.25	16.54	11.12	7.95	6.18	18.20	-8.40	30.98
275-325	8.82	3.05	21.97	13.56	10.56	7.42	23.46	-15.93	39.18
$2.1<\|\eta_2\|<3.0$									
40-45	2.80	17.06	10.37	8.20	7.50	8.95	3.49	5.58	26.78
45-50	3.00	15.39	11.01	8.19	7.16	9.26	3.96	4.78	25.95
50-55	3.19	14.09	11.57	7.24	6.93	9.47	4.45	4.20	25.18
55-60	3.37	13.07	12.06	6.14	6.78	9.62	4.94	3.75	24.62
60-70	3.60	12.02	12.64	5.09	6.70	9.75	5.62	3.30	24.28
70-80	3.94	10.89	13.39	4.73	6.73	9.82	6.67	2.75	24.36
80-90	4.27	10.13	14.04	5.75	6.91	9.81	7.74	2.25	24.98
90-100	4.60	9.61	14.62	7.68	7.21	9.73	8.85	1.73	26.04
100-125	5.07	9.15	15.32	10.74	7.79	9.57	10.45	0.86	28.03
125-150	5.94	8.67	16.47	13.53	9.15	9.20	13.53	-1.23	31.31
150-175	6.87	8.39	17.51	7.33	10.83	8.80	16.86	-4.08	31.95
175-225	7.98	8.05	18.62	-13.01	13.04	8.38	20.88	-8.16	34.86

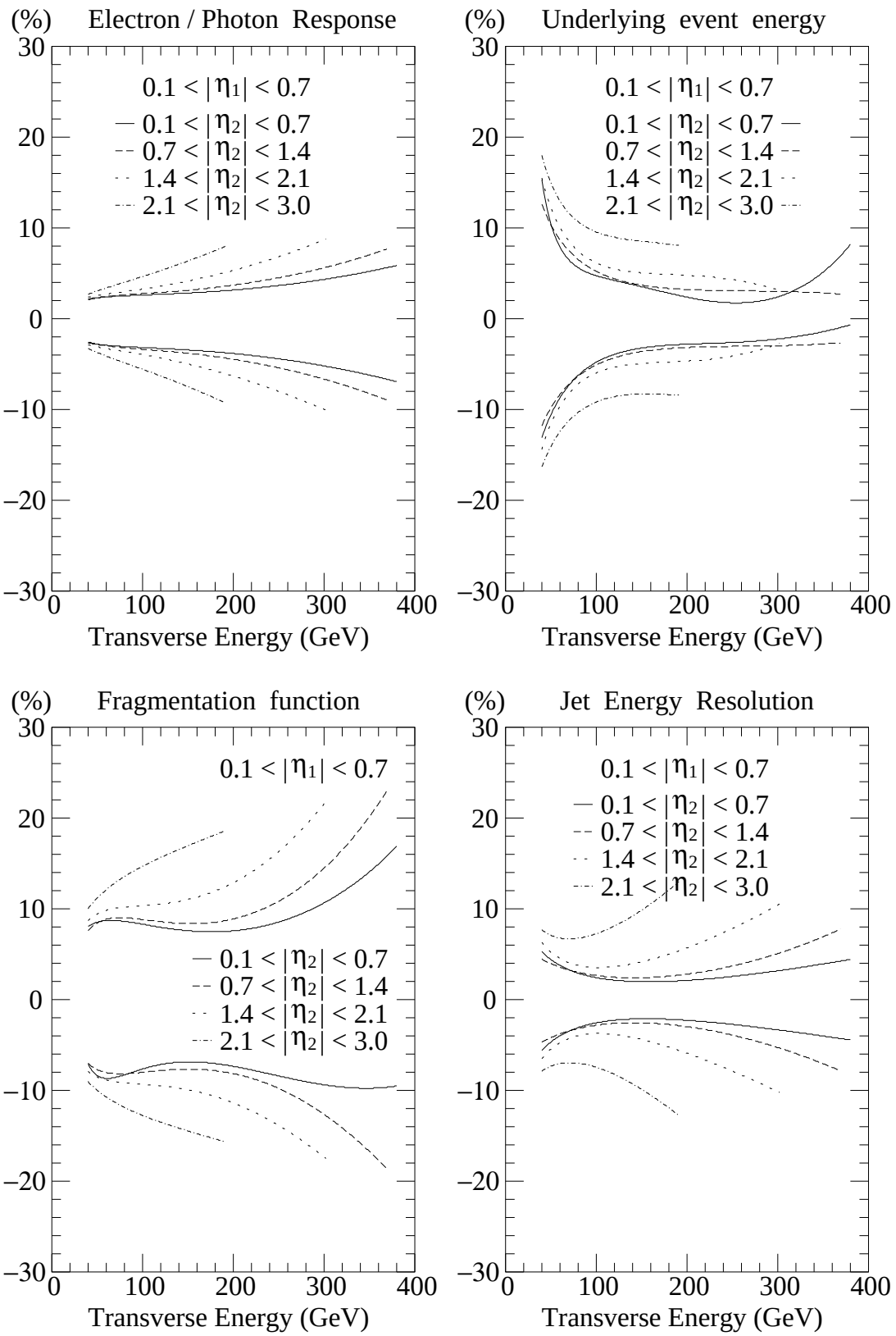

Figure 3.10: The percentage changes in the cross section. The electron/photon response and the parton fragmentation function is changed by ± 1 standard deviation from the standard one. The underlying event energy is changed by $\pm 30\%$. The jet energy resolution is changed by $\pm 10\%$.

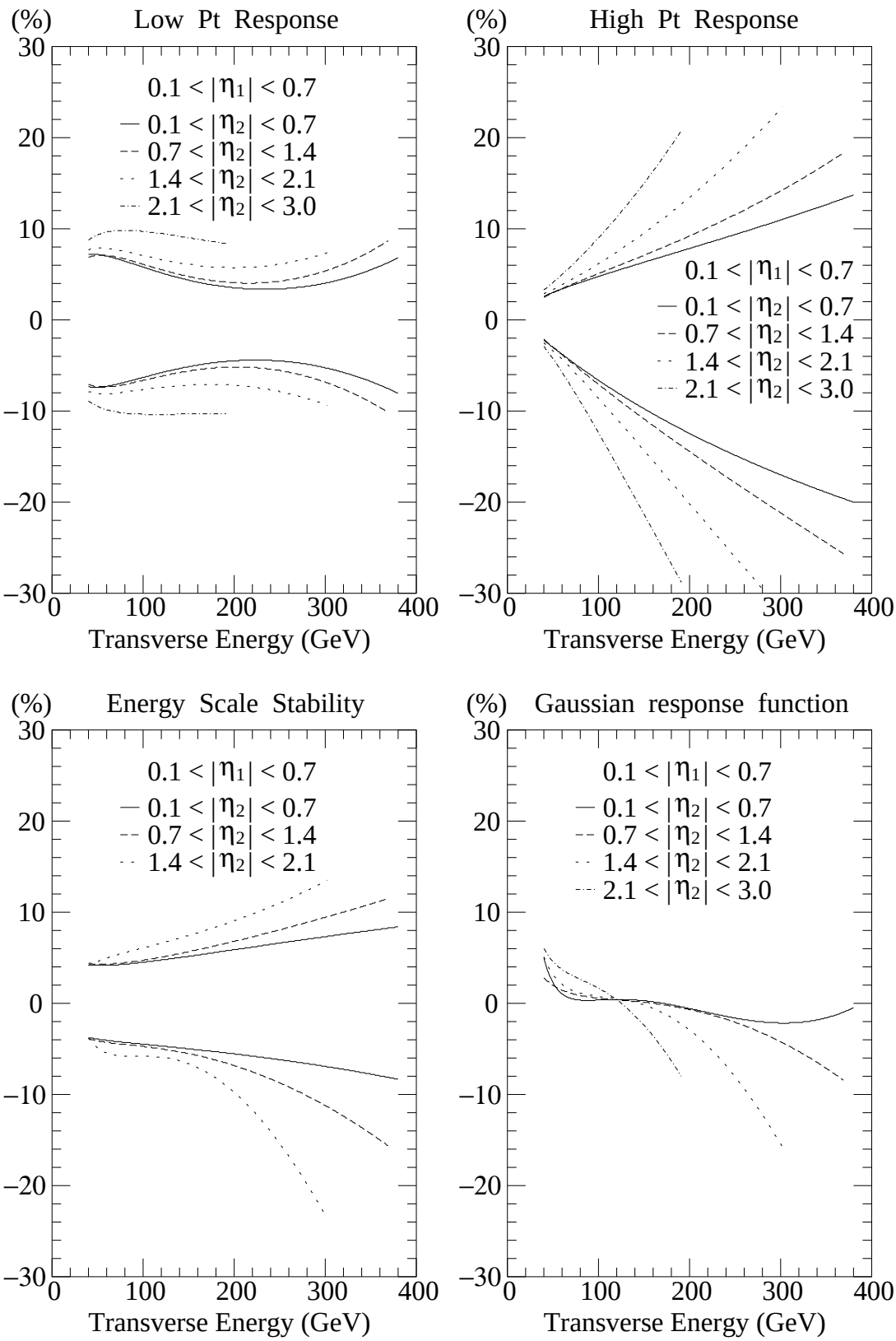

Figure 3.11: The percentage changes in the cross section. The calorimeter response to charged pions at low p_{T} and high p_{T} is changed by ± 1 standard deviation from the standard one. The calorimeter energy scale instability is changed by $\pm 1\%$. The response function is simplified to the gaussian.

Systematic and Statistical Uncertainties on the cross section

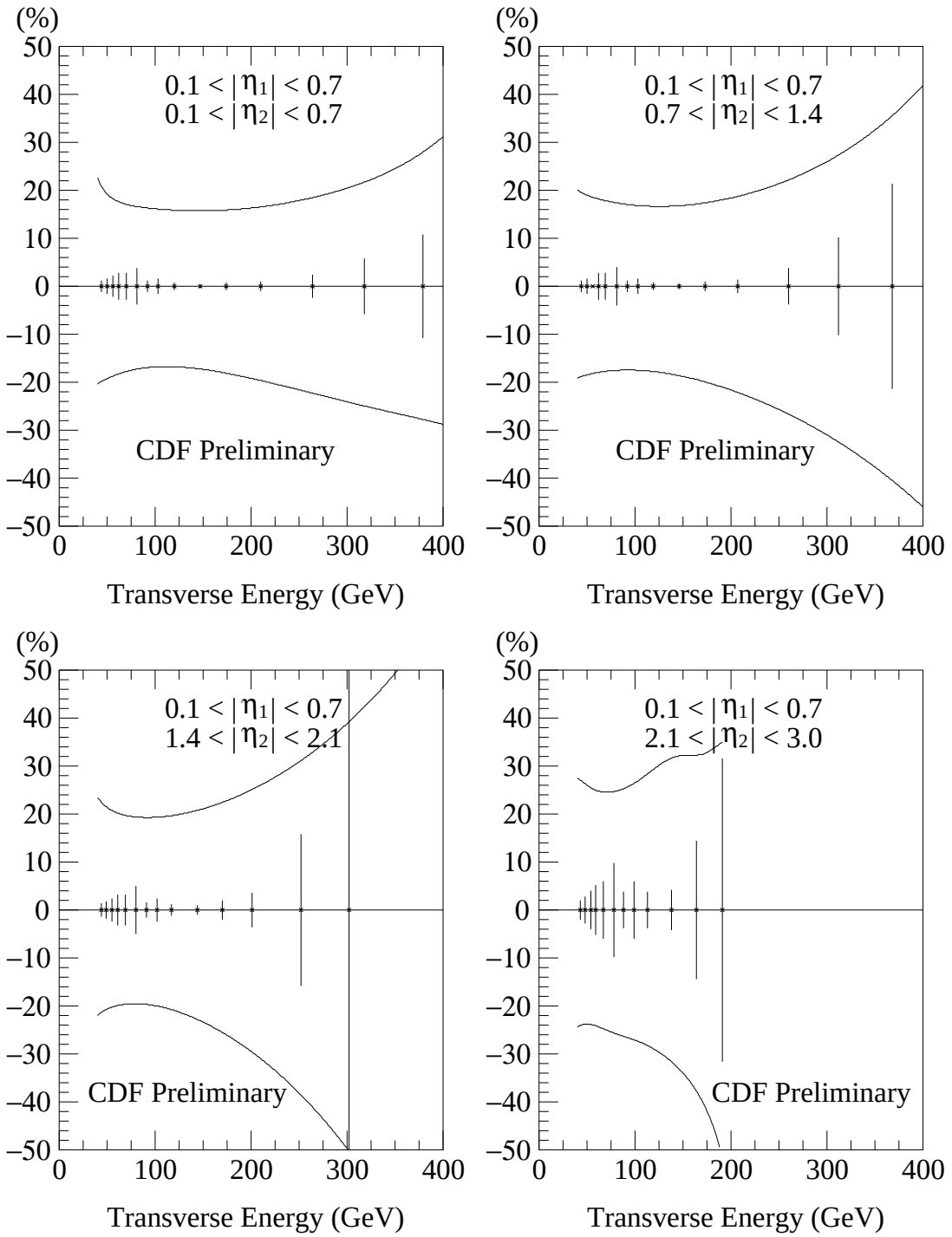

Figure 3.12: Statistical and the total systematic uncertainties versus central jet E_{T}. The vertical line shows the statistical uncertainty and the curve is the systematic uncertainty including the normalization uncertainty of 8.0%.

Chapter 4

Measurement of α_S

4.1 α_s determination from two jet production cross sections

It is discussed in Ref. [56] that inclusive jet cross section is useful to determine the strong coupling α_s by comparing with the next-to-leading order parton level calculations such as JETRAD [57].

4.1.1 Two jet production cross sections in NLO QCD

The two jet differential cross section to the order of α_s^3 is represented as

$$\frac{d\sigma^{data}}{dE_T d\eta_1 d\eta_2} = \frac{d\sigma\,[\,2 \to 2\ partons]}{dE_T d\eta_1 d\eta_2} + \frac{d\sigma\,[\,2 \to 3\ partons]}{dE_T d\eta_1 d\eta_2}. \tag{4.1}$$

Here, η_1 and η_2 refer to pseudorapidities of the two jets and E_T is the transverse energy of jet-1. In this analysis, we restrict jet-1 to be in the central region of the detector ($0.1 < |\eta_1| < 0.7$) whereas *second* jets with $E_T > 10$ GeV in wider region in η.

In QCD perturbative calculations we define two energy scales; One is the renormalization scale μ_R which arises in the matrix element for QCD hard processes, and the other is the factorization scale μ_F which associates with the structure function. For simplicity, as usual, we take these energy scales as common and proportional to E_T, $\mu_R = \mu_F = \lambda E_T$. In this analysis, we choose $\lambda = 0.5$, as used in Ref. [58]. The

systematic uncertainty of this choice is evaluated by changing λ to 1.0, as described later.

The $2 \to 2$ subprocess is expressed by:

$$\frac{d\sigma\,[\,2 \to 2\ partons]}{dE_{\rm T}d\eta_1 d\eta_2} = \alpha_{\rm s}^2(\mu_{\rm R}) \sum_{a,b} F_a^p(x_1,\mu_{\rm F}) F_b^{\bar{p}}(x_2,\mu_{\rm F}) |M_{ab}^{NLO}[2 \to 2](x_1,x_2)|^2 dx_1 dx_2 \tag{4.2}$$

with

$$x_1 = \frac{E_{\rm T}}{\sqrt{s}}(e^{+\eta_1} + e^{+\eta_2}), \quad x_2 = \frac{E_{\rm T}}{\sqrt{s}}(e^{-\eta_1} + e^{-\eta_2}) \tag{4.3}$$

and the $2 \to 3$ subprocess is expressed by:

$$\frac{d\sigma\,[\,2 \to 3\ partons]}{dE_{\rm T}d\eta_1 d\eta_2} = \alpha_{\rm s}^3(\mu_{\rm R}) \sum_{a,b} f_a^p(x_1,\mu_{\rm F}) f_b^{\bar{p}}(x_2,\mu_{\rm F}) |M_{ab}^{LO}[2 \to 3](x_1,x_2)|^2 dx_1 dx_2 \tag{4.4}$$

with

$$\begin{aligned} x_1 &= \frac{E_{\rm T1}}{\sqrt{s}}(e^{+\eta_1} + \frac{E_{\rm T2}}{E_{\rm T1}}e^{+\eta_2} + \frac{E_{\rm T3}}{E_{\rm T1}}e^{+\eta_3}), \\ x_2 &= \frac{E_{\rm T1}}{\sqrt{s}}(e^{-\eta_1} + \frac{E_{\rm T2}}{E_{\rm T1}}e^{-\eta_2} + \frac{E_{\rm T3}}{E_{\rm T1}}e^{-\eta_3}). \end{aligned} \tag{4.5}$$

Here, a square of the subprocess amplitude is

$$|M_{ab}^{NLO}[2 \to 2](x_1,x_2)|^2 = |M_{ab}^{LO}[2 \to 2](x_1,x_2) + \alpha_{\rm s}(\mu_{\rm R}) M_{ab}^{1-loop}[2 \to 2](x_1,x_2)|^2. \tag{4.6}$$

It is summed over the spins and colors of final partons 1, 2 and averaged over initial partons a, b with the "NLO" proton structure functions

$$F_a^p(x_1,\mu_{\rm F}) = f_a^p(x_1,\mu_{\rm F}) + \alpha_{\rm s}(\mu_{\rm R})\, C_a^p(x_1,\mu_{\rm F}) \tag{4.7}$$

where $f_a^p(x,\mu_{\rm F})$ is the "standard" structure function, CTEQ4 [58], MRSA′ [59], or GRV94 [60], which is evolved to NLO using the crossing function $C_a^p(x_1,\mu_{\rm F})$. The crossing function is calculated by convoluting the "standard" structure function with Altarelli-Parisi splitting function as described in Ref. [61]. The x_i relations to η_i and $E_{{\rm T}i}$, Eqs.(4.3) and (4.5), come from the momentum conservation in the transverse plane.

Substituting the above into Eq.(4.1), one obtains the following cubic equation:

$$\frac{d\sigma^{data}}{dE_{\rm T}d\eta_1 d\eta_2} = A_1(\mu_{\rm F})\alpha_{\rm s}^2(\mu_{\rm R}) + A_2(\mu_{\rm F})\alpha_{\rm s}^3(\mu_{\rm R}) + A_3(\mu_{\rm F})\alpha_{\rm s}^3(\mu_{\rm R}) \tag{4.8}$$

where

A_1 : LO $[2 \to 2]$ amplitude ($|\mathrm{M}_{ab}^{LO}[2 \to 2]|^2 \otimes f_a^p f_b^{\bar{p}}$)

A_2 : NLO $[2 \to 2]$ 1-loop process interference amplitude

$(\mathrm{M}_{ab}^{1-loop}[2 \to 2]^* \mathrm{M}_{ab}^{LO}[2 \to 2] \otimes f_a^p f_b^{\bar{p}})$

+ crossing corrections ($|\mathrm{M}_{ab}^{LO}[2 \to 2]|^2 \otimes C_a^p f_b^{\bar{p}}$ + $|\mathrm{M}_{ab}^{LO}[2 \to 2]|^2 \otimes f_a^p C_b^{\bar{p}}$)

A_3 : LO $[2 \to 3]$ amplitude ($|\mathrm{M}_{ab}^{LO}[2 \to 3]|^2 \otimes f_a^p f_b^{\bar{p}}$).

The matrix elements squared $|M|^2$ can be decomposed into four terms:

$$|M|^2 = |M|^2_{(A)} + |M|^2_{(B)} + |M|^2_{(C)} + |M|^2_{(D)} \tag{4.9}$$

which correspond to the following partonic subprocesses,

$$(A) \quad q_a + q_b \quad \to \quad q_a + q_b + (g), \quad a \neq b, \tag{4.10}$$

$$(B) \quad q_a + q_a \quad \to \quad q_a + q_a + (g), \tag{4.11}$$

$$(C) \quad q_a + g \quad \to \quad q_a + g + (g), \tag{4.12}$$

$$(D) \quad g + g \quad \to \quad g + g + (g). \tag{4.13}$$

The parenthesis (g) denotes hard gluon radiation in $2 \to 3$ parton processes.

4.1.2 $\alpha_{\rm s}$ with CTEQ4M structure functions

The following procedure is performed to extract $\alpha_{\rm s}$:

1) Calculate the coefficients A_1, A_2, and A_3 of Eq.(4.8) using the JETRAD code in each bin as functions of $E_{\rm T}$, η_1, and η_2, $E_{\rm T}$ being the transverse energy of central jets.

   Tables 4.1 and 4.2 show the results obtained for CTEQ4M proton structure functions for energy scale definition of $\mu_{\rm R} = \mu_{\rm F} = 0.5E_{\rm T}$ and of $\mu_{\rm R} = \mu_{\rm F} = E_{\rm T}$.

The E_{T} dependences of A_1 and A_2+A_3 are shown in Fig. 4.1 for the two energy scale definitions.

In the above calculation we take the CTEQ4M structure functions as our standard since they can describe the CDF distributions reasonably well, and have the best overall quantitative agreement between NLO QCD theory and global data on high energy scattering. Actually, the CTEQ4M structure functions are the result of a global fit to a variety of measurement data in various processes such as DIS, Drell-Yan processes, inclusive photon production, CDF W production asymmetry, and CDF and D0 jet production.

2) Solve the cubic Eq.(4.8) analytically to extract α_{s} in each bin.

   E_{T} dependent α_{s} values are translated into $\alpha_{\mathrm{s}}(\mathrm{M_Z})$ using the running α_{s} equation Eq.(1.26), where E_{T} or $0.5E_{\mathrm{T}}$ is taken as μ_{R} (or μ in Eq.(1.26)) according to the two definitions we have. Note that E_{T} is the average transverse energy in a given bin weighted by the cross section.

3) Take the weighted mean of $\alpha_{\mathrm{s}}(\mathrm{M_Z})$ in the range of $0.1 < |\eta_1| < 0.7$, $0.1 < |\eta_2| < 0.7$, and $50 < E_{\mathrm{T}} < 150$ GeV.

   The rms deviation from the mean value is taken as the statistical uncertainty. We restrict the η range as central where the calorimeter response is well understood. The lower bound of the E_{T} range is selected to exclude the range where the trigger efficiency decreases rapidly and unsmearing procedure has large uncertainty. The higher bound is selected because the QCD calculation starts to deviate from the CDF measurement (high E_{T} "anomaly"). The structure functions are not well measured in such a high Q^2 region. The systematic uncertainty arising from the choice of the fit range is discussed below.

The results of $\alpha_{\mathrm{s}}(\mathrm{M_Z})$ are summarized in Tables 4.5 and 4.6 with the energy scale definition of $\mu_{\mathrm{R}} = \mu_{\mathrm{F}} = 0.5E_{\mathrm{T}}$ and of $\mu_{\mathrm{R}} = \mu_{\mathrm{F}} = E_{\mathrm{T}}$, respectively. For the purpose of comparison, the tables include the results also for various other modern structure functions, and for $|\eta_2|$ range extended to 1.4 or 2.1. Also shown are the statistical errors, and the range of the value in parentheses including the statistical

and systematic uncertainties. As the central value of $\alpha_s(M_Z)$ we choose the best fit value given with CTEQ4M, $0.117 \pm 0.001(stat.)$.

4.1.3 α_s with other structure functions

The α_s as derived from Eq.(4.8) is dependent on the structure functions through the coefficients A_1 to A_3. Tables 4.3 and 4.4 show the results obtained for CTEQ4HJ proton structure functions for energy scale definition of $\mu_R = \mu_F = 0.5E_T$ and of $\mu_R = \mu_F = E_T$. Figure 4.3 shows the α_s values determined using CTEQ4HJ as a function of the central jet E_T in three η_2 bins. The best fit $\alpha_s(M_Z)$ is $0.1186 \pm 0.0004(stat.)$. Overlaid is a curve based on this $\alpha_s(M_Z)$ value with five flavors in the region $\mu = 0.5E_T < 175$ GeV, and six in the region above. The agreement between the curve and the data points are fairly good, showing clearly the running feature of the strong coupling constant.

The results with CTEQ4M, MRSA′115, and GRV94300 are shown in Fig. 4.2, Fig. 4.4, and Fig. 4.5, respectively. As described before, only the data are used in the fit of the E_T range from 50 to 150 GeV and in the η_2 range of $0.1 < |\eta_2| < 0.7$. The data points in higher E_T bins in these three figures seem to deviate from the curve. This is due to the CDF "anomaly" of high E_T jet production. Since CTEQ4HJ uses the CDF jet production cross section in calculation, the deviation is the smallest among these. We also note that the agreement of the data points in $1.4 < |\eta_2| < 2.1$ is better with CTEQ4HJ than with other structure functions.

Similar calculations were performed using other sets of structure functions. The results of $\alpha_s(M_Z)$ are summarized in Table 4.5, 4.6, and Fig. 4.12. The cross in the figure is a "recommended" $\alpha_s(M_Z)$ that has been used to evolve experimental data to the energy scale where the structure functions are defined. The agreement between the best fit $\alpha_s(M_Z)$ and the "recommended" $\alpha_s(M_Z)$ is fairly good for most of the structure functions. We note that the agreement is better with the structure function that has a "recommended" $\alpha_s(M_Z)$ around 0.115. The uncertainty arising from the value of the "recommended" $\alpha_s(M_Z)$ can be studied in some of the structure functions where other sets are provided with different values of $\alpha_s(M_Z)$ [see next section]. CTEQ4An (CTEQ4M stands for CTEQ4A3) is a modified version of CTEQ4M,

where the "recommended" $\alpha_s(M_Z)$ in CTEQ4M of 0.116 is changed to 0.110 (4A1), 0.113 (4A2), 0.119 (4A4) and 0.122 (4A5). Similarly, MRSA$'nnn$ ($e.g. nnn = 115$) is a modified MRSA$'$, where the "recommended" $\alpha_s(M_Z)$ in MRSA$'$ is changed to $0.nnn$ ($e.g. nnn = 115$). GRV94 is modified to GRV94mmm ($mmm = 300$) similarly, where the "recommended" $\alpha_s(M_Z)$ are provided in GRV in terms of Λ_{QCD} (4 flavors) – it is changed from 200 MeV to mmm ($mmm = 300$) MeV.

Table 4.1: Two jet cross section, calculated A_1, A_2, A_3, $\alpha_s(\mu)$, and $\alpha_s(M_Z)$ on each μ and η_2 bin. They are from JETRAD calculation using CTEQ4M structure function with energy scale $\mu_R = \mu_F = 0.5E_T$. The μ is the mean value of $0.5E_T$, where E_T is the transverse energy of the central jet ($0.1 < |\eta_1| < 0.7$), weighted by the differential cross section on each bin.

μ=0.5$\langle E_T \rangle$	nb/GeV	A_1(LO)	$A_2(2\to2)$	$A_3(2\to3)$	$\alpha_s(\mu)$	$\alpha_s(M_Z)$
	$0.1<\|\eta_2\|<0.7$					
21.13	1.6501E1	6.2744E2	−2.8975E4	2.9545E4	0.1520	0.1181
23.64	9.5021E0	3.7881E2	−1.8688E4	1.8949E4	0.1507	0.1193
26.15	5.7179E0	2.3860E2	−1.2450E4	1.2676E4	0.1452	0.1176
28.66	3.5717E0	1.5561E2	−8.5263E3	8.6344E3	0.1444	0.1188
32.16	1.9161E0	8.8270E1	−5.1234E3	5.1827E3	0.1408	0.1184
37.20	8.8008E-1	4.3515E1	−2.7028E3	2.7306E3	0.1364	0.1178
42.23	4.3933E-1	2.3077E1	−1.5125E3	1.5262E3	0.1328	0.1174
47.25	2.3432E-1	1.2942E1	−8.8665E2	8.9369E2	0.1300	0.1171
54.92	9.4383E-2	5.5345E0	−3.9967E2	4.0267E2	0.1263	0.1167
67.62	2.8013E-2	1.7575E0	−1.3511E2	1.3609E2	0.1222	0.1167
80.25	9.8553E-3	6.4166E-1	−5.1442E1	5.1747E1	0.1205	0.1182
96.61	2.7772E-3	1.8382E-1	−1.5270E1	1.5379E1	0.1188	0.1198
	$0.7<\|\eta_2\|<1.4$					
21.13	1.4345E1	6.0428E2	−2.8635E4	2.9106E4	0.1460	0.1144
23.64	8.3616E0	3.6034E2	−1.8207E4	1.8487E4	0.1445	0.1154
26.15	5.0562E0	2.2409E2	−1.1957E4	1.2115E4	0.1431	0.1163
28.66	3.1578E0	1.4431E2	−8.0675E3	8.1667E3	0.1412	0.1166
32.16	1.6832E0	8.0392E1	−4.7489E3	4.7943E3	0.1393	0.1173
37.19	7.6047E-1	3.8586E1	−2.4311E3	2.4544E3	0.1350	0.1168
42.22	3.7122E-1	1.9872E1	−1.3186E3	1.3294E3	0.1320	0.1167
47.24	1.9288E-1	1.0816E1	−7.4836E2	7.5360E2	0.1295	0.1167
54.85	7.4245E-2	4.3977E0	−3.1985E2	3.2197E2	0.1262	0.1165
67.53	2.0238E-2	1.2715E0	−9.8189E1	9.8831E1	0.1224	0.1169
80.15	6.4642E-3	4.1641E-1	−3.3498E1	3.3737E1	0.1205	0.1181
96.18	1.5777E-3	1.0110E-1	−8.4179E0	8.4869E0	0.1201	0.1211
	$1.4<\|\eta_2\|<2.1$					
21.12	1.2548E1	4.8131E2	−2.3897E4	2.4187E4	0.1544	0.1195
23.63	6.9217E0	2.7690E2	−1.4589E4	1.4764E4	0.1511	0.1195
26.14	3.9868E0	1.6607E2	−9.1968E3	9.2944E3	0.1486	0.1198
28.65	2.3809E0	1.0298E2	−5.9546E3	6.0039E3	0.1470	0.1205
32.12	1.1965E0	5.4221E1	−3.2991E3	3.3309E3	0.1427	0.1197
37.16	4.9730E-1	2.3867E1	−1.5408E3	1.5541E3	0.1391	0.1198
42.18	2.2288E-1	1.1192E1	−7.5776E2	7.6333E2	0.1366	0.1202
47.20	1.0585E-1	5.4979E0	−3.8689E2	3.9009E2	0.1337	0.1200
54.61	3.5193E-2	1.8816E0	−1.3846E2	1.3976E2	0.1309	0.1205
67.25	7.2757E-3	3.8947E-1	−3.0314E1	3.0732E1	0.1282	0.1220
79.83	1.6997E-3	8.5743E-2	−6.9372E0	7.0697E0	0.1286	0.1258
94.97	2.6863E-4	1.1670E-2	−9.7498E-1	1.0064E0	0.1305	0.1314

Table 4.2: Similar to Table 4.1, but with energy scale $\mu_R = \mu_F = E_T$.

$\mu = \langle E_T \rangle$	nb/GeV	A_1(LO)	$A_2(2\to2)$	$A_3(2\to3)$	$\alpha_s(\mu)$	$\alpha_s(M_Z)$
	$0.1<\lvert\eta_2\rvert<0.7$					
42.26	1.6501E1	6.1943E2	−2.6985E4	2.8666E4	0.1391	0.1222
47.28	9.5021E0	3.6825E2	−1.7162E4	1.8214E4	0.1363	0.1222
52.30	5.7179E0	2.2894E2	−1.1294E4	1.1949E4	0.1343	0.1225
57.31	3.5717E0	1.4763E2	−7.6528E3	8.0825E3	0.1322	0.1225
64.32	1.9161E0	8.2595E1	−4.5412E3	4.7832E3	0.1297	0.1225
74.40	8.8008E-1	4.0070E1	−2.3586E3	2.4823E3	0.1258	0.1218
84.46	4.3933E-1	2.0968E1	−1.3028E3	1.3663E3	0.1235	0.1220
94.50	2.3432E-1	1.1630E1	−7.5535E2	7.9247E2	0.1206	0.1213
109.85	9.4383E-2	4.9042E0	−3.3574E2	3.5207E2	0.1176	0.1210
135.24	2.8013E-2	1.5299E0	−1.1151E2	1.1679E2	0.1146	0.1216
160.50	9.8553E-3	5.5097E-1	−4.1866E1	4.3804E1	0.1131	0.1232
193.22	2.7772E-3	1.5559E-1	−1.2239E1	1.2829E1	0.1119	0.1253
	$0.7<\lvert\eta_2\rvert<1.4$					
42.27	1.4345E1	5.8802E2	−2.6273E4	2.7867E4	0.1338	0.1181
47.28	8.3616E0	3.4535E2	−1.6473E4	1.7449E4	0.1327	0.1193
52.30	5.0562E0	2.1208E2	−1.0689E4	1.1260E4	0.1326	0.1211
57.31	3.1578E0	1.3506E2	−7.1385E3	7.5243E3	0.1305	0.1210
64.31	1.6832E0	7.4255E1	−4.1494E3	4.3665E3	0.1284	0.1214
74.38	7.6047E-1	3.5073E1	−2.0920E3	2.1999E3	0.1251	0.1211
84.44	3.7122E-1	1.7832E1	−1.1205E3	1.1771E3	0.1225	0.1210
94.48	1.9288E-1	9.5980E0	−6.2907E2	6.5994E2	0.1204	0.1210
109.70	7.4245E-2	3.8491E0	−2.6526E2	2.7812E2	0.1177	0.1210
135.06	2.0238E-2	1.0936E0	−8.0025E1	8.3903E1	0.1147	0.1217
160.30	6.4642E-3	3.5313E-1	−2.6918E1	2.8222E1	0.1136	0.1237
192.35	1.5777E-3	8.4467E-2	−6.6608E0	6.9986E0	0.1134	0.1270
	$1.4<\lvert\eta_2\rvert<2.1$					
42.24	1.2548E1	4.5563E2	−2.1301E4	2.2567E4	0.1407	0.1234
47.26	6.9217E0	2.5849E2	−1.2833E4	1.3586E4	0.1382	0.1237
52.28	3.9868E0	1.5306E2	−7.9979E3	8.4294E3	0.1371	0.1248
57.29	2.3809E0	9.3929E1	−5.1269E3	5.4072E3	0.1345	0.1244
64.25	1.1965E0	4.8831E1	−2.8056E3	2.9571E3	0.1319	0.1244
74.31	4.9730E-1	2.1164E1	−1.2918E3	1.3570E3	0.1296	0.1253
84.37	2.2288E-1	9.7972E0	−6.2752E2	6.6110E2	0.1260	0.1245
94.41	1.0585E-1	4.7625E0	−3.1712E2	3.3315E2	0.1251	0.1258
109.22	3.5193E-2	1.6080E0	−1.1202E2	1.1803E2	0.1225	0.1261
134.50	7.2757E-3	3.2671E-1	−2.4078E1	2.5461E1	0.1213	0.1292
159.66	1.6997E-3	7.0749E-2	−5.4229E0	5.7699E0	0.1225	0.1344
189.94	2.6863E-4	9.4552E-3	−7.4779E-1	8.0706E-1	0.1260	0.1429

Table 4.3: Similar to Table 4.1, but obtained using CTEQ4HJ.

μ=0.5$\langle E_{\mathrm{T}}\rangle$	nb/GeV	A_1(LO)	$A_2(2\to2)$	$A_3(2\to3)$	$\alpha_s(\mu)$	$\alpha_s(M_Z)$
	$0.1<\lvert\eta_2\rvert<0.7$					
21.13	1.6501E1	6.3901E2	−2.9380E4	2.9907E4	0.1515	0.1177
23.64	9.5021E0	3.8299E2	−1.8813E4	1.9097E4	0.1494	0.1185
26.15	5.7179E0	2.3953E2	−1.2443E4	1.2672E4	0.1448	0.1174
28.66	3.5717E0	1.5516E2	−8.4611E3	8.5652E3	0.1448	0.1190
32.16	1.9161E0	8.7223E1	−5.0385E3	5.1003E3	0.1413	0.1187
37.20	8.8008E-1	4.2512E1	−2.6275E3	2.6574E3	0.1374	0.1186
42.23	4.3933E-1	2.2324E1	−1.4560E3	1.4727E3	0.1338	0.1181
47.25	2.3432E-1	1.2428E1	−8.4728E2	8.5319E2	0.1332	0.1196
54.92	9.4383E-2	5.2741E0	−3.7907E2	3.8246E2	0.1286	0.1186
67.62	2.8013E-2	1.6686E0	−1.2791E2	1.2905E2	0.1244	0.1187
80.25	9.8553E-3	6.1313E-1	−4.9158E1	4.9446E1	0.1233	0.1208
96.61	2.7772E-3	1.7937E-1	−1.4984E1	1.5102E1	0.1198	0.1209
	$0.7<\lvert\eta_2\rvert<1.4$					
21.13	1.4345E1	6.0698E2	−2.8646E4	2.9110E4	0.1458	0.1143
23.64	8.3616E0	3.5927E2	−1.8076E4	1.8350E4	0.1448	0.1156
26.15	5.0562E0	2.2189E2	−1.1787E4	1.1947E4	0.1437	0.1167
28.66	3.1578E0	1.4204E2	−7.9045E3	8.0137E3	0.1416	0.1169
32.16	1.6832E0	7.8562E1	−4.6207E3	4.6642E3	0.1410	0.1185
37.19	7.6047E-1	3.7420E1	−2.3483E3	2.3691E3	0.1374	0.1185
42.22	3.7122E-1	1.9193E1	−1.2690E3	1.2815E3	0.1334	0.1178
47.24	1.9288E-1	1.0432E1	−7.1980E2	7.2509E2	0.1316	0.1184
54.85	7.4245E-2	4.2555E0	−3.0925E2	3.1153E2	0.1278	0.1179
67.53	2.0238E-2	1.2488E0	−9.6807E1	9.7410E1	0.1237	0.1180
80.15	6.4642E-3	4.1861E-1	−3.3992E1	3.4222E1	0.1203	0.1180
96.18	1.5777E-3	1.0513E-1	−8.9125E0	8.9778E0	0.1182	0.1192
	$1.4<\lvert\eta_2\rvert<2.1$					
21.12	1.2548E1	4.7313E2	−2.3414E4	2.3710E4	0.1555	0.1201
23.63	6.9217E0	2.7127E2	−1.4251E4	1.4423E4	0.1525	0.1204
26.14	3.9868E0	1.6248E2	−8.9771E3	9.0826E3	0.1496	0.1204
28.65	2.3809E0	1.0078E2	−5.8189E3	5.8696E3	0.1483	0.1213
32.12	1.1965E0	5.3276E1	−3.2414E3	3.2681E3	0.1447	0.1211
37.16	4.9730E-1	2.3688E1	−1.5326E3	1.5431E3	0.1406	0.1209
42.18	2.2288E-1	1.1263E1	−7.6613E2	7.7086E2	0.1368	0.1204
47.20	1.0585E-1	5.6247E0	−3.9896E2	4.0188E2	0.1327	0.1193
54.61	3.5193E-2	1.9754E0	−1.4732E2	1.4839E2	0.1290	0.1189
67.25	7.2757E-3	4.2597E-1	−3.3874E1	3.4280E1	0.1236	0.1179
79.83	1.6997E-3	9.6729E-2	−8.0590E0	8.1977E0	0.1223	0.1198
94.97	2.6863E-4	1.3502E-2	−1.1687E0	1.2023E0	0.1234	0.1242

Table 4.4: Similar to Table 4.3, but with energy scale $\mu_R = \mu_F = E_T$.

$\mu = \langle E_T \rangle$	nb/GeV	A_1(LO)	$A_2(2\to2)$	$A_3(2\to3)$	$\alpha_s(\mu)$	$\alpha_s(M_Z)$
	$0.1<\lvert\eta_2\rvert<0.7$					
42.26	1.6501E1	6.2555E2	−2.7102E4	2.8805E4	0.1384	0.1217
47.28	9.5021E0	3.6943E2	−1.7126E4	1.8179E4	0.1361	0.1220
52.30	5.7179E0	2.2821E2	−1.1201E4	1.1871E4	0.1341	0.1223
57.31	3.5717E0	1.4628E2	−7.5443E3	7.9532E3	0.1334	0.1235
64.32	1.9161E0	8.1205E1	−4.4419E3	4.6835E3	0.1304	0.1232
74.40	8.8008E-1	3.9017E1	−2.2857E3	2.4087E3	0.1269	0.1228
84.46	4.3933E-1	2.0254E1	−1.2531E3	1.3153E3	0.1252	0.1236
94.50	2.3432E-1	1.1168E1	−7.2261E2	7.5826E2	0.1228	0.1235
109.85	9.4383E-2	4.6847E0	−3.1976E2	3.3531E2	0.1200	0.1236
135.24	2.8013E-2	1.4613E0	−1.0641E2	1.1152E2	0.1167	0.1240
160.50	9.8553E-3	5.3080E-1	−4.0425E1	4.2285E1	0.1150	0.1255
193.22	2.7772E-3	1.5318E-1	−1.2147E1	1.2720E1	0.1129	0.1265
	$0.7<\lvert\eta_2\rvert<1.4$					
42.27	1.4345E1	5.8686E2	−2.6094E4	2.7644E4	0.1343	0.1185
47.28	8.3616E0	3.4243E2	−1.6256E4	1.7271E4	0.1324	0.1191
52.30	5.0562E0	2.0907E2	−1.0492E4	1.1100E4	0.1322	0.1207
57.31	3.1578E0	1.3249E2	−6.9725E3	7.3641E3	0.1311	0.1215
64.31	1.6832E0	7.2433E1	−4.0315E3	4.2461E3	0.1296	0.1224
74.38	7.6047E-1	3.4021E1	−2.0227E3	2.1277E3	0.1268	0.1227
84.44	3.7122E-1	1.7251E1	−1.0816E3	1.1370E3	0.1240	0.1225
94.48	1.9288E-1	9.2879E0	−6.0808E2	6.3719E2	0.1225	0.1232
109.70	7.4245E-2	3.7439E0	−2.5826E2	2.7049E2	0.1194	0.1229
135.06	2.0238E-2	1.0809E0	−7.9541E1	8.3264E1	0.1157	0.1229
160.30	6.4642E-3	3.5691E-1	−2.7510E1	2.8797E1	0.1134	0.1235
192.35	1.5777E-3	8.8012E-2	−7.0739E0	7.4188E0	0.1117	0.1249
	$1.4<\lvert\eta_2\rvert<2.1$					
42.24	1.2548E1	4.4754E2	−2.0865E4	2.2157E4	0.1411	0.1237
47.26	6.9217E0	2.5343E2	−1.2556E4	1.3259E4	0.1402	0.1253
52.28	3.9868E0	1.5005E2	−7.8309E3	8.2705E3	0.1376	0.1252
57.29	2.3809E0	9.2222E1	−5.0312E3	5.3073E3	0.1355	0.1253
64.25	1.1965E0	4.8163E1	−2.7716E3	2.9195E3	0.1328	0.1253
74.31	4.9730E-1	2.1102E1	−1.2925E3	1.3557E3	0.1302	0.1259
84.37	2.2288E-1	9.9053E0	−6.3826E2	6.7090E2	0.1261	0.1245
94.41	1.0585E-1	4.8880E0	−3.2836E2	3.4438E2	0.1241	0.1248
109.22	3.5193E-2	1.6887E0	−1.1923E2	1.2538E2	0.1204	0.1238
134.50	7.2757E-3	3.5498E-1	−2.6718E1	2.8210E1	0.1172	0.1245
159.66	1.6997E-3	7.8825E-2	−6.2043E0	6.6077E0	0.1163	0.1269
189.94	2.6863E-4	1.0736E-2	−8.7630E-1	9.4389E-1	0.1195	0.1345

Table 4.5: Calculated $\alpha_s(M_Z)$ using various structure functions with energy scale $\mu_R = \mu_F = 0.5E_T$. The uncertainties are the rms spread of the weighted distribution of $\alpha_s(M_Z)$ calculated in each bin, which correspond to the statistical uncertainties conservatively. The range of $\alpha_s(M_Z)$ due to the systematic uncertainties of the cross section is shown in parentheses.

structure function	input $\alpha_s(M_Z)$	$0.1 < \|\eta_2\| < 0.7$	$0.1 < \|\eta_2\| < 1.4$	$0.1 < \|\eta_2\| < 2.1$
CTEQ4HJ	0.116	0.1186±0.0004	0.1183±0.0005	0.1184±0.0007
		(0.1093∼0.1264)	(0.1087∼0.1263)	(0.1085∼0.1267)
CTEQ4A1	0.110	0.1129±0.0009	0.1130±0.0007	0.1137±0.0017
		(0.1039∼0.1204)	(0.1037∼0.1207)	(0.1041∼0.1217)
CTEQ4A2	0.113	0.1147±0.0008	0.1147±0.0006	0.1153±0.0016
		(0.1056∼0.1223)	(0.1053∼0.1225)	(0.1056∼0.1234)
CTEQ4M	0.116	0.1169±0.0004	0.1168±0.0003	0.1175±0.0016
		(0.1076∼0.1246)	(0.1073∼0.1248)	(0.1076∼0.1257)
CTEQ4A4	0.119	0.1190±0.0003	0.1190±0.0004	0.1196±0.0016
		(0.1097∼0.1269)	(0.1093∼0.1270)	(0.1096∼0.1280)
CTEQ4A5	0.122	0.1212±0.0003	0.1212±0.0005	0.1218±0.0017
		(0.1117∼0.1292)	(0.1114∼0.1294)	(0.1117∼0.1303)
MRSA′	0.111	0.1159±0.0005	0.1159±0.0004	0.1167±0.0017
		(0.1067∼0.1237)	(0.1065∼0.1239)	(0.1068∼0.1249)
MRSA′115	0.115	0.1171±0.0003	0.1172±0.0004	0.1180±0.0018
		(0.1079∼0.1249)	(0.1077∼0.1253)	(0.1080∼0.1263)
MRSA′120	0.120	0.1185±0.0005	0.1187±0.0008	0.1197±0.0025
		(0.1091∼0.1264)	(0.1090∼0.1268)	(0.1096∼0.1281)
MRSA′125	0.125	0.1204±0.0009	0.1208±0.0013	0.1219±0.0031
		(0.1109∼0.1284)	(0.1110∼0.1291)	(0.1117∼0.1305)
GRV94	0.109	0.1160±0.0013	0.1158±0.0011	0.1163±0.0016
		(0.1068∼0.1237)	(0.1063∼0.1237)	(0.1065∼0.1245)
GRV94250	0.113	0.1169±0.0006	0.1167±0.0005	0.1173±0.0015
		(0.1076∼0.1247)	(0.1071∼0.1247)	(0.1074∼0.1256)
GRV94300	0.116	0.1177±0.0003	0.1176±0.0004	0.1183±0.0017
		(0.1084∼0.1256)	(0.1080∼0.1257)	(0.1083∼0.1267)
GRV94350	0.119	0.1193±0.0005	0.1192±0.0006	0.1199±0.0019
		(0.1099∼0.1273)	(0.1095∼0.1274)	(0.1098∼0.1284)
GRV94400	0.122	0.1206±0.0009	0.1205±0.0010	0.1213±0.0022
		(0.1110∼0.1286)	(0.1106∼0.1288)	(0.1110∼0.1298)
CTEQ3L	0.107	0.1159±0.0003	0.1159±0.0003	0.1164±0.0011
		(0.1067∼0.1237)	(0.1064∼0.1239)	(0.1066∼0.1246)
CTEQ3M	0.112	0.1115±0.0006	0.1118±0.0005	0.1126±0.0020
		(0.1026∼0.1190)	(0.1026∼0.1195)	(0.1031∼0.1206)

Table 4.5: (Continued).

structure function	input $\alpha_s(M_Z)$	$0.1 < \|\eta_2\| < 0.7$	$0.1 < \|\eta_2\| < 1.4$	$0.1 < \|\eta_2\| < 2.1$
CTEQ2MF	0.109	0.1175±0.0016	0.1176±0.0017	0.1182±0.0022
		(0.1082∼0.1253)	(0.1079∼0.1256)	(0.1082∼0.1265)
CTEQ2ML	0.117	0.1124±0.0018	0.1123±0.0016	0.1130±0.0022
		(0.1035∼0.1200)	(0.1031∼0.1200)	(0.1034∼0.1209)
CTEQ2MS	0.109	0.1160±0.0006	0.1158±0.0006	0.1163±0.0013
		(0.1068∼0.1237)	(0.1064∼0.1237)	(0.1065∼0.1245)
MRSD−′	0.111	0.1186±0.0006	0.1187±0.0005	0.1194±0.0018
		(0.1092∼0.1265)	(0.1090∼0.1268)	(0.1094∼0.1278)
MRSD0′	0.111	0.1131±0.0010	0.1134±0.0012	0.1144±0.0025
		(0.1040∼0.1206)	(0.1041∼0.1212)	(0.1046∼0.1225)
MRSG	0.113	0.1180±0.0014	0.1182±0.0011	0.1190±0.0022
		(0.1086∼0.1258)	(0.1085∼0.1262)	(0.1090∼0.1274)

Table 4.6: Similar to Table 4.1, but the energy scales are defined as $\mu = E_T$.

structure function	input $\alpha_s(M_Z)$	$0.1 < \|\eta_2\| < 0.7$	$0.1 < \|\eta_2\| < 1.4$	$0.1 < \|\eta_2\| < 2.1$
CTEQ4HJ	0.116	0.1238±0.0004	0.1233±0.0006	0.1235±0.0007
		(0.1139∼0.1321)	(0.1132∼0.1318)	(0.1130∼0.1323)
CTEQ4M	0.116	0.1215±0.0004	0.1215±0.0004	0.1224±0.0022
		(0.1118∼0.1297)	(0.1115∼0.1299)	(0.1120∼0.1311)
MRSA′	0.111	0.1202±0.0005	0.1202±0.0005	0.1211±0.0022
		(0.1105∼0.1283)	(0.1103∼0.1285)	(0.1108∼0.1298)
GRV94	0.110	0.1194±0.0012	0.1192±0.0010	0.1200±0.0021
		(0.1099∼0.1275)	(0.1094∼0.1275)	(0.1098∼0.1286)
CTEQ3L	0.107	0.1212±0.0006	0.1212±0.0006	0.1218±0.0016
		(0.1115∼0.1294)	(0.1112∼0.1296)	(0.1114∼0.1305)
CTEQ3M	0.112	0.1158±0.0006	0.1161±0.0007	0.1172±0.0026
		(0.1065∼0.1237)	(0.1065∼0.1242)	(0.1072∼0.1256)
CTEQ2MF	0.109	0.1220±0.0020	0.1221±0.0019	0.1229±0.0027
		(0.1122∼0.1302)	(0.1120∼0.1305)	(0.1124∼0.1317)
CTEQ2ML	0.117	0.1170±0.0016	0.1169±0.0014	0.1178±0.0025
		(0.1076∼0.1249)	(0.1073∼0.1250)	(0.1078∼0.1263)
CTEQ2MS	0.109	0.1203±0.0005	0.1201±0.0005	0.1208±0.0017
		(0.1106∼0.1284)	(0.1102∼0.1284)	(0.1105∼0.1294)
MRSD−′	0.111	0.1230±0.0006	0.1230±0.0005	0.1240±0.0023
		(0.1131∼0.1313)	(0.1129∼0.1315)	(0.1134∼0.1328)
MRSD0′	0.111	0.1171±0.0013	0.1176±0.0015	0.1187±0.0031
		(0.1077∼0.1251)	(0.1079∼0.1257)	(0.1086∼0.1272)
MRSG	0.113	0.1224±0.0013	0.1226±0.0010	0.1237±0.0028
		(0.1126∼0.1307)	(0.1125∼0.1311)	(0.1132∼0.1326)

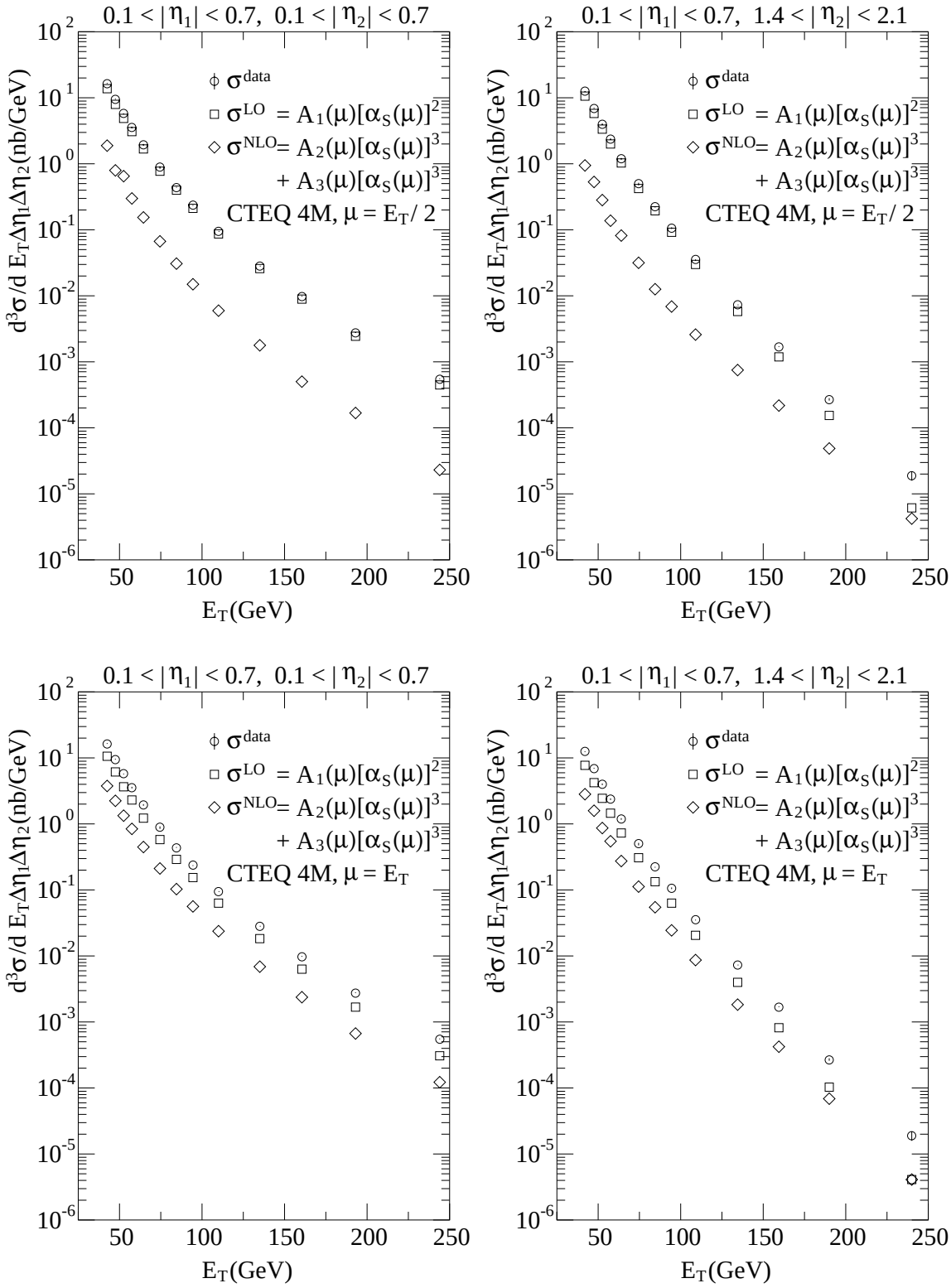

Figure 4.1: The contributions of the LO and NLO−LO two jet cross sections using CTEQ4M with energy scale definition of $\mu = 0.5E_{\mathrm{T}}$ or $\mu = E_{\mathrm{T}}$. In high η_2 and E_{T}, NLO contribution get higher.

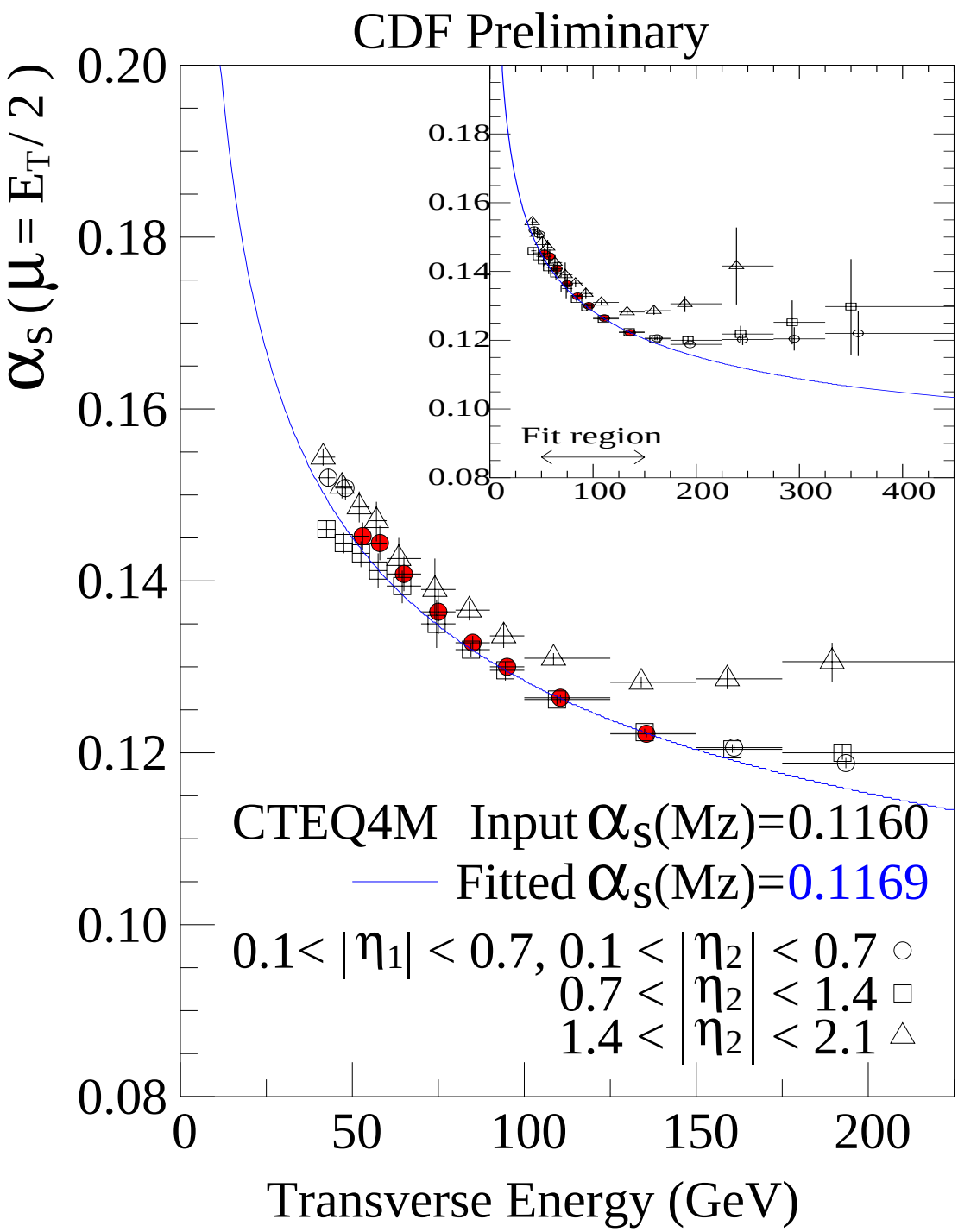

Figure 4.2: The α_s as a function of the central jet E_T obtained using CTEQ4M. The best fit $\alpha_s(M_Z)$ is 0.1169 ± 0.0004 by taking in the region $0.1 < |\eta_1| < 0.7$ and $0.1 < |\eta_2| < 0.7$ with $50 < E_T < 150$ GeV. The curve is based on this $\alpha_s(M_Z)$ value with five flavors in the region $\mu = 0.5E_T < 175$ GeV, and with six in the region beyond.

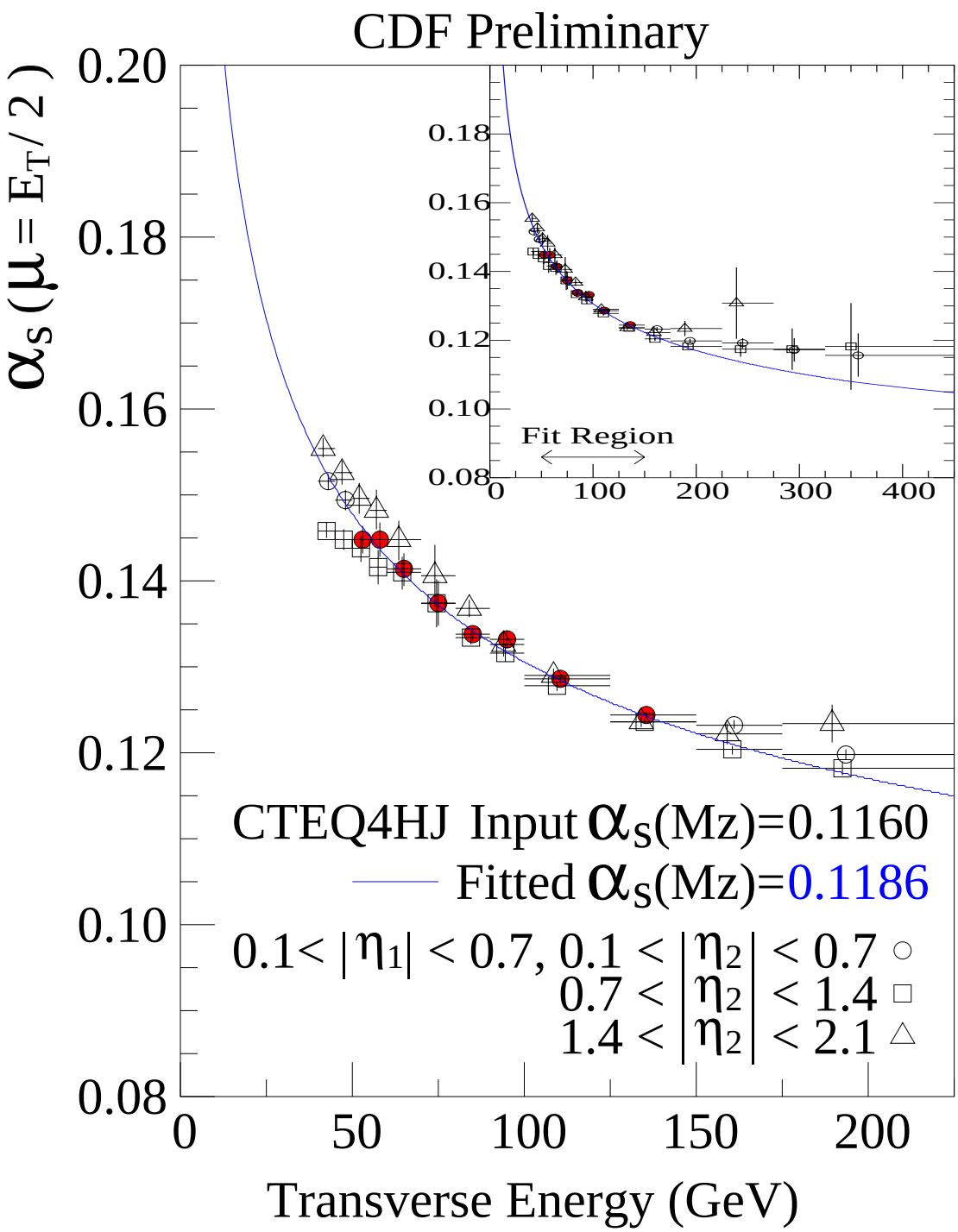

Figure 4.3: The α_s as a function of the central jet E_T obtained using CTEQ4HJ. The best fit $\alpha_s(M_Z)$ is 0.1186 ± 0.0004 by taking in the region $0.1 < |\eta_1| < 0.7$ and $0.1 < |\eta_2| < 0.7$ with $50 < E_T < 150$ GeV. The curve is based on this $\alpha_s(M_Z)$ value with five flavors in the region $\mu = 0.5E_T < 175$ GeV, and with six in the region beyond.

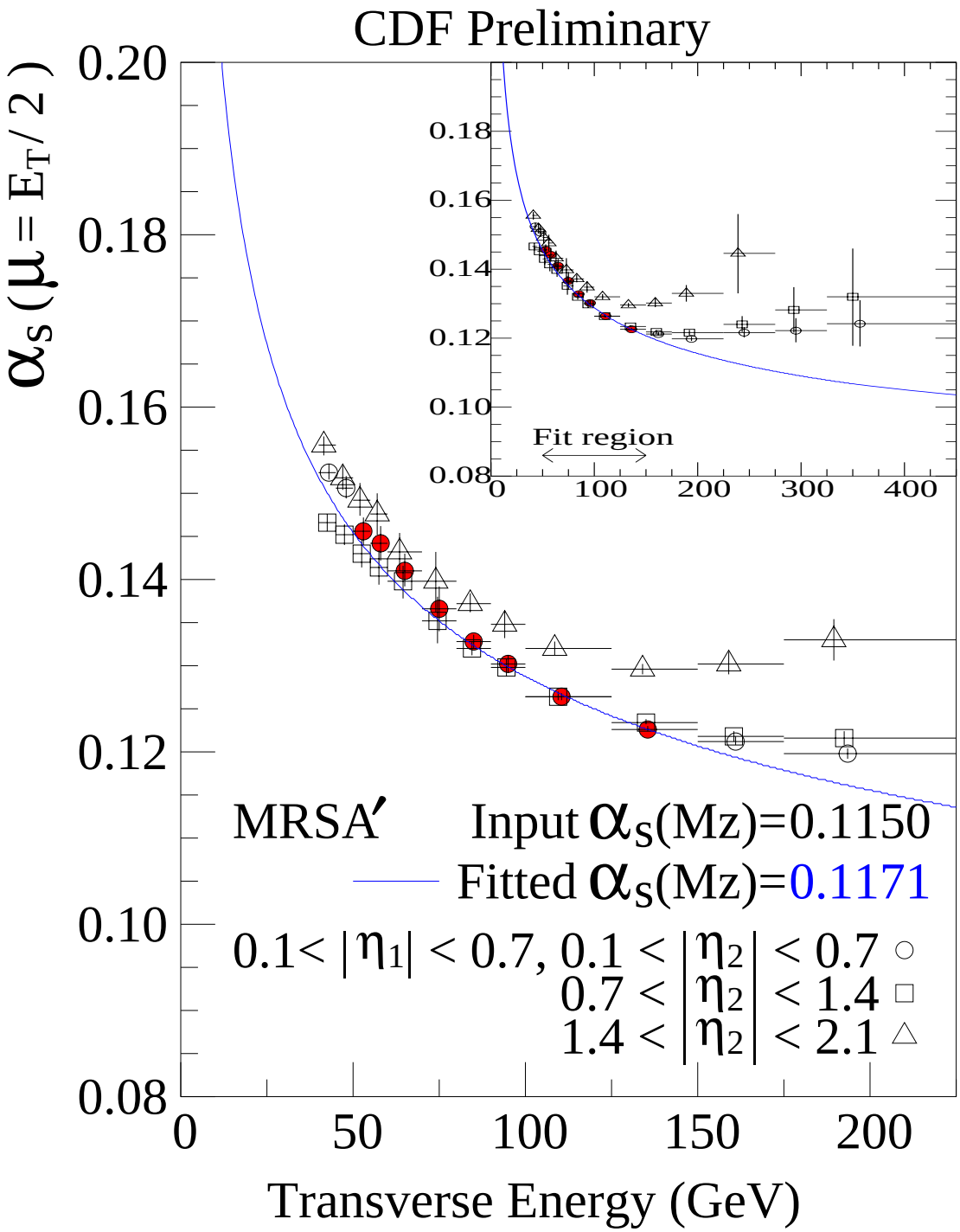

Figure 4.4: Similar to Fig. 4.2, but obtained using MRSA′115. The best fit $\alpha_s(M_Z)$ is 0.1171 ± 0.0003.

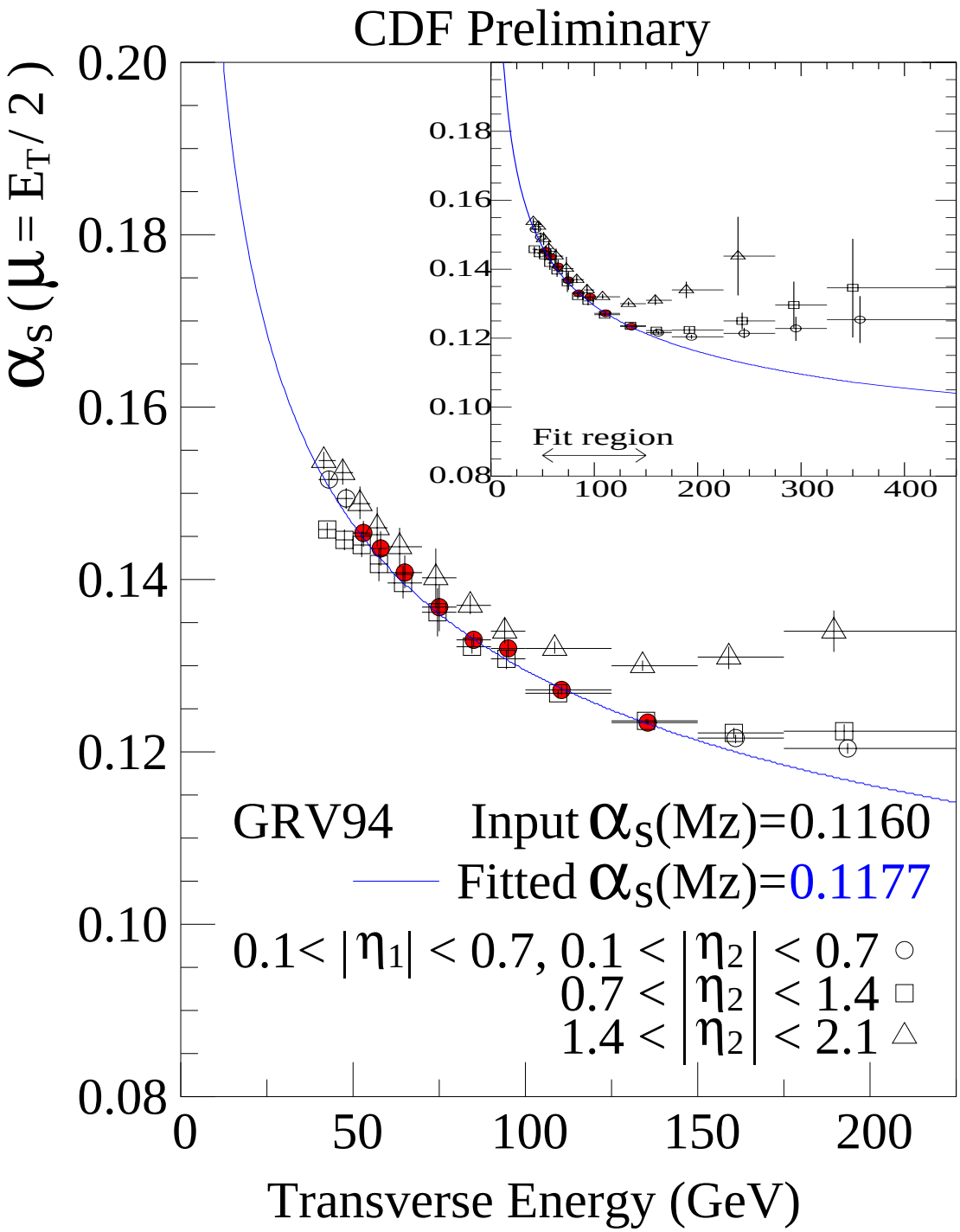

Figure 4.5: Similar to Fig. 4.2, but obtained using GRV94300. The best fit $\alpha_s(M_Z)$ is 0.1177 ± 0.0003.

4.2 Systematic uncertainties on α_s

4.2.1 Experimental systematic uncertainties

Experimental systematic uncertainties have two sources of the uncertainty on the cross section and that on the E_T range used for the α_s calculation:

1) Systematic uncertainty on the cross section.

   The systematic uncertainty on the true cross section originates from that of the response functions. Figures 4.6 to 4.9 show the α_s obtained from systematically "deviated" cross sections. The cross section may be deviated due to the electron/photon response uncertainty, the underlying event energy ($\pm 30\%$), the parton fragmentation function, the calorimeter energy scale instability ($\pm 1\%$), the jet energy resolution uncertainty ($\pm 10\%$), the calorimeter response to charged pions at low p_T or high p_T, the response function simplified to the gaussian, or the luminosity measurement uncertainty ($\pm 8\%$), respectively as discussed in Chapter 3. Table 4.7 shows the contributions from the various sources that determine the calorimeter response function. In this evaluation we used CTEQ4M structure functions with $\mu_R = \mu_F = 0.5E_T$. The quadrature sum of these contributions gives α_s uncertainty of about 7%. Note that the correlated systematic uncertainty of the cross section is typically 16% (see Section 3.4), which is explained by that the cross section is proportional to α_s^2. We assign ± 0.009 for this systematic uncertainty.

2) Dependence on the fit region.

   The central value of the α_s is obtained by taking the weighted mean of $\alpha_s(M_Z)$ in the specific η and E_T range of $0.1 < |\eta_1| < 0.7$, $0.1 < |\eta_2| < 0.7$, and $50 < E_T < 150$ GeV. To estimate the dependence on the E_T range used in the fit, we calculate α_s also in the ranges $50 < E_T < 125$, $60 < E_T < 150$, and $60 < E_T < 125$ GeV. The difference of the $\alpha_s(M_Z)$ is fairly small typically ± 0.0001 between these E_T ranges. We conservatively assign ± 0.0003 for this systematic uncertainty.

Adding the above uncertainties in quadrature, the experimental systematic uncertainty is evaluated to be ± 0.009.

Table 4.7: Contributions to the $\alpha_s(M_Z)$ uncertainty from various sources that determine the calorimeter response function.

Electron/photon	$-1.5 \sim +1.2$ %
Underlying $\pm 30\%$	$-1.9 \sim +2.0$ %
Fragmentation	$-3.3 \sim +3.5$ %
Energy stability $\pm 1\%$	$-2.1 \sim +2.1$ %
Energy resolution $\pm 10\%$	$-1.1 \sim +1.0$ %
Low p_T response	$-2.6 \sim +2.3$ %
High p_T response	$-3.6 \sim +2.4$ %
Gaussian response	$0.0 \sim +0.2$ %
Normalization $\pm 8\%$	$-3.7 \sim +3.5$ %
Total	$-7.5 \sim +6.9$ %

4.2.2 Theoretical systematic uncertainties

The theoretical uncertainties can be summarized as follows:

1) Dependence on the structure functions.

   The uncertainty from the choice of the structure functions is described in detail in Section 4.1.3. Among the original CTEQ4M, MRSA′, and GRV94 structure functions, we found the α_s to change by about ± 0.001. Including other structure functions, CTEQ2M(F,L,S) and MRS(D$-'$, D0′), this uncertainty increases slightly to ± 0.002. We assign ± 0.002 for this uncertainty.

2) Choice of the energy scales μ_R and μ_F.

   The uncertainty arising from the choice of the energy scales is studied for some sets of structure functions, CTEQ4M, MRSA′, GRV94, and CTEQ4HJ. The scales were changed from $\mu_R = \mu_F = 0.5E_T$ to $\mu_R = \mu_F = E_T$. The α_s obtained with CTEQ4M and CTEQ4HJ at $\mu_R = \mu_F = E_T$ are shown in Fig. 4.10 and Fig. 4.11. By changing the scales to $\mu_R = \mu_F = E_T$, the best fit $\alpha_s(M_Z)$ are shifted upward by 0.005 for this set of structure functions. The shifts for other sets of structure functions are in the range $(0.003 - 0.005)$. We assign ± 0.005 for this uncertainty.

3) Dependence on the "recommended" $\alpha_s(M_Z)$.

Each set of structure functions provides the "recommended" $\alpha_s(M_Z)$ that has been used to evolve experimental data to the energy scale where the structure functions are defined. The uncertainty due to this dependence is studied using CTEQ4M by changing the "recommended" $\alpha_s(M_Z)$ from 0.110 to 0.122, the corresponding sets of structure functions being CTEQ4Ai ($i = 1, \ldots, 5$). Fig. 4.13 shows this dependence using the sets of CTEQ4M, MRSA$'$, and GRV94 structure functions. The uncertainty on CTEQ4M, MRSA$'$, and GRV94 are ± 0.003, ± 0.002, and ± 0.002 respectively. We assign ± 0.003 for this uncertainty.

4) Higher order corrections to A_i.

The contributions from $\mathcal{O}(\alpha_s^4)$ and higher are partially available: the matrix element of two-to-two partonic scattering subprocesses with two loops is missing for the next-to-next-to-leading order calculation. Here, we estimate the NNLO contribution by assuming naively that the ratio of σ^{NNLO} to σ^{NLO} is the same as of σ^{NLO} to σ^{LO}. According to Fig. 4.1, σ^{NNLO} contribution is typically $\sim 1\%$ at energy scale definition $\mu_R = \mu_F = 0.5E_T$ and $\sim 10\%$ at $\mu_R = \mu_F = E_T$ in the whole fit region. Therefore we estimate a shift of $\alpha_s(M_Z) \sim -0.0006$ at $\mu_R = \mu_F = 0.5E_T$ and ~ -0.006 at $\mu_R = \mu_F = E_T$ from the higher order processes. As discussed in 2), $\alpha_s(M_Z)$ at NLO is shifted upward by 0.005 by changing $\mu_R = \mu_F = 0.5E_T$ to $\mu_R = \mu_F = E_T$. This shift compensates the NNLO contribution of ~ -0.006 at $\mu_R = \mu_F = E_T$. Thus we expect a smaller dependence on the choice of the energy scales μ_R and μ_F if we include higher order processes. Note that we consider 2 or 3 parton final state matrix elements in the NLO calculation. The measured cross section with the second jets at large η is larger than the NLO calculation, which could be attributed to that the phase space with ≥ 4 jets is larger in the real events than with ≤ 3 jets. We assign ± 0.006 for this uncertainty.

5) Validity of the CTEQ4M structure functions.

The uncertainty of the gluon parton distribution may be considerable especially in high Q^2 and high x region [58]. One of such evidences is the discrepancy observed in the CDF inclusive jet cross section at high E_{T} [62]. With CTEQ4HJ which describes better the CDF jet cross section at high E_{T}, we obtain α_{s} of 0.1186. The difference of α_{s} is 0.002. We assign ± 0.002 for this uncertainty.

Table 4.8: Contributions to the theoretical uncertainties on $\alpha_{\mathrm{s}}(\mathrm{M_Z})$.

Dependence on the structure functions	± 0.002
Choice of the energy scales μ_{R} and μ_{F}	± 0.005
Dependence on the "recommended" $\alpha_{\mathrm{s}}(\mathrm{M_Z})$	± 0.003
Higher order corrections to A_i	± 0.006
Validity of the CTEQ4M structure functions	± 0.002
Total	± 0.009

Adding the above in quadrature, we obtain ± 0.009 as the theoretical uncertainty (see Table 4.8). Some of the above estimates are, however, naive and premature. We do not quote this uncertainty in our α_{s} value, expecting further theoretical understanding will provide a more reliable estimate of the uncertainty.

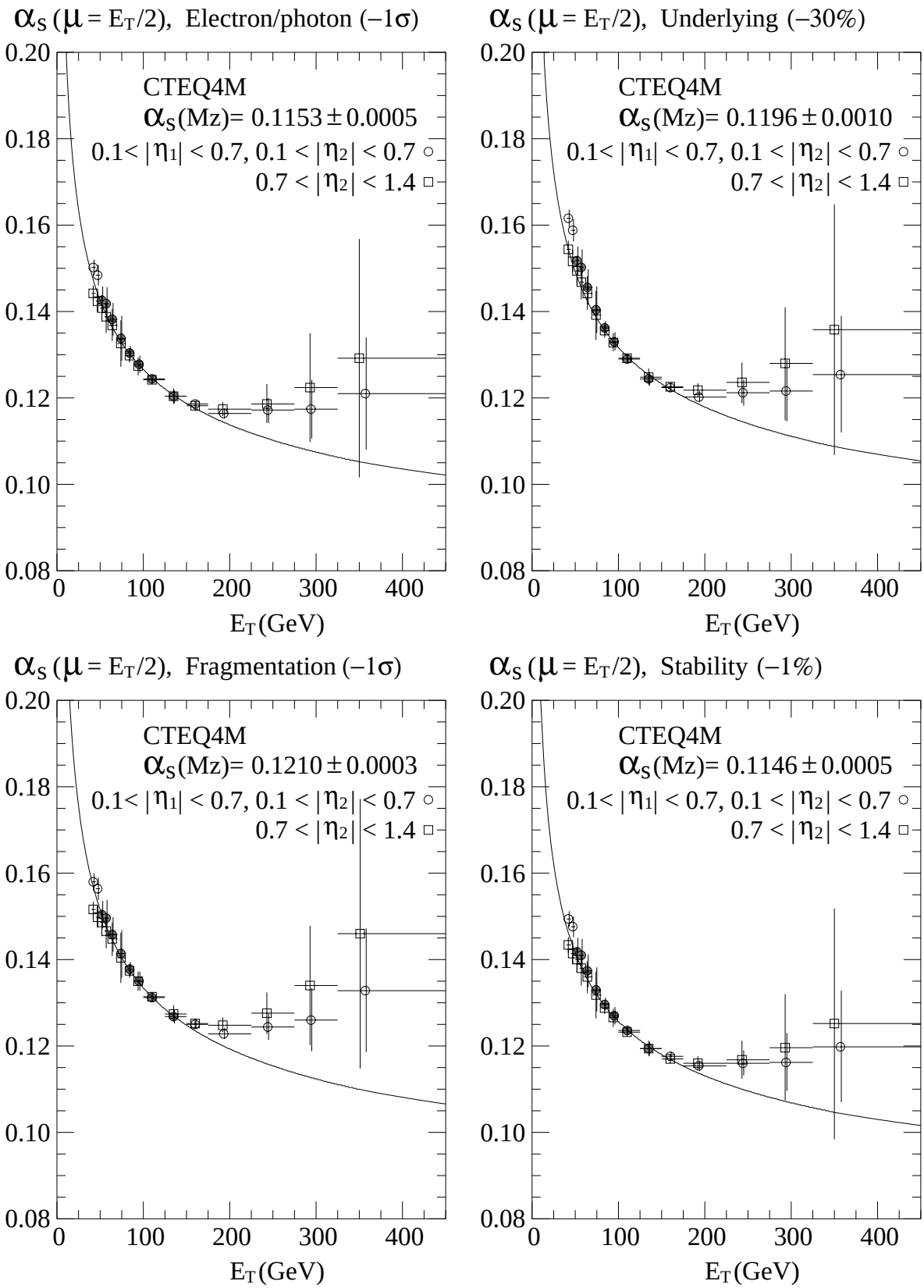

Figure 4.6: The α_s obtained using CTEQ4M from systematically "deviated" cross sections. The cross section is deviated due to the electron/photon response uncertainty (-1σ), the underlying event energy (-30%), the parton fragmentation function (-1σ), or the calorimeter energy scale instability (-1%), respectively.

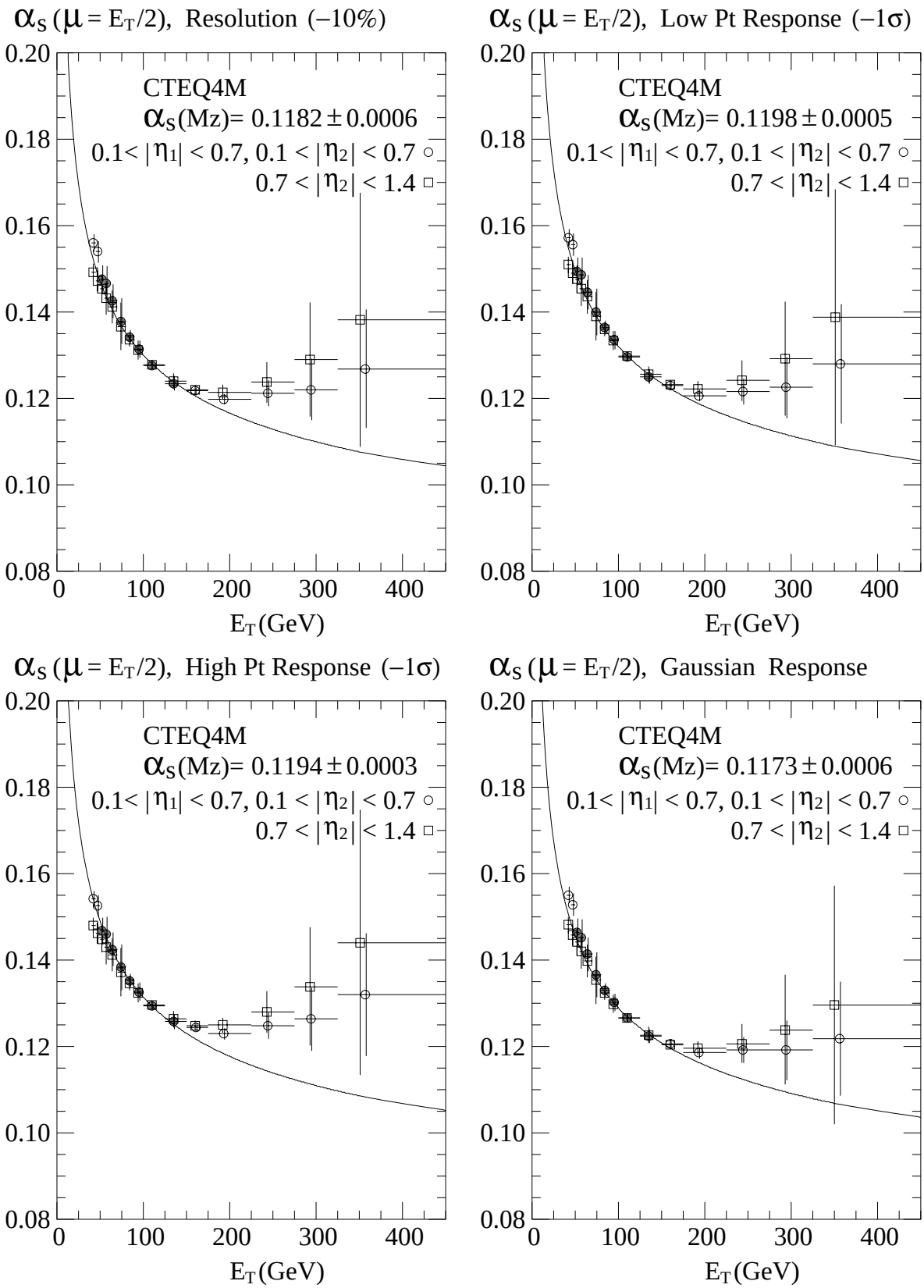

Figure 4.7: Similar to Fig. 4.6, but the cross section is deviated due to the jet energy resolution uncertainty (-10%), the calorimeter response to charged pions at low p_{T} (-1σ) or high p_{T} (-1σ), or the response function simplified to the gaussian, respectively.

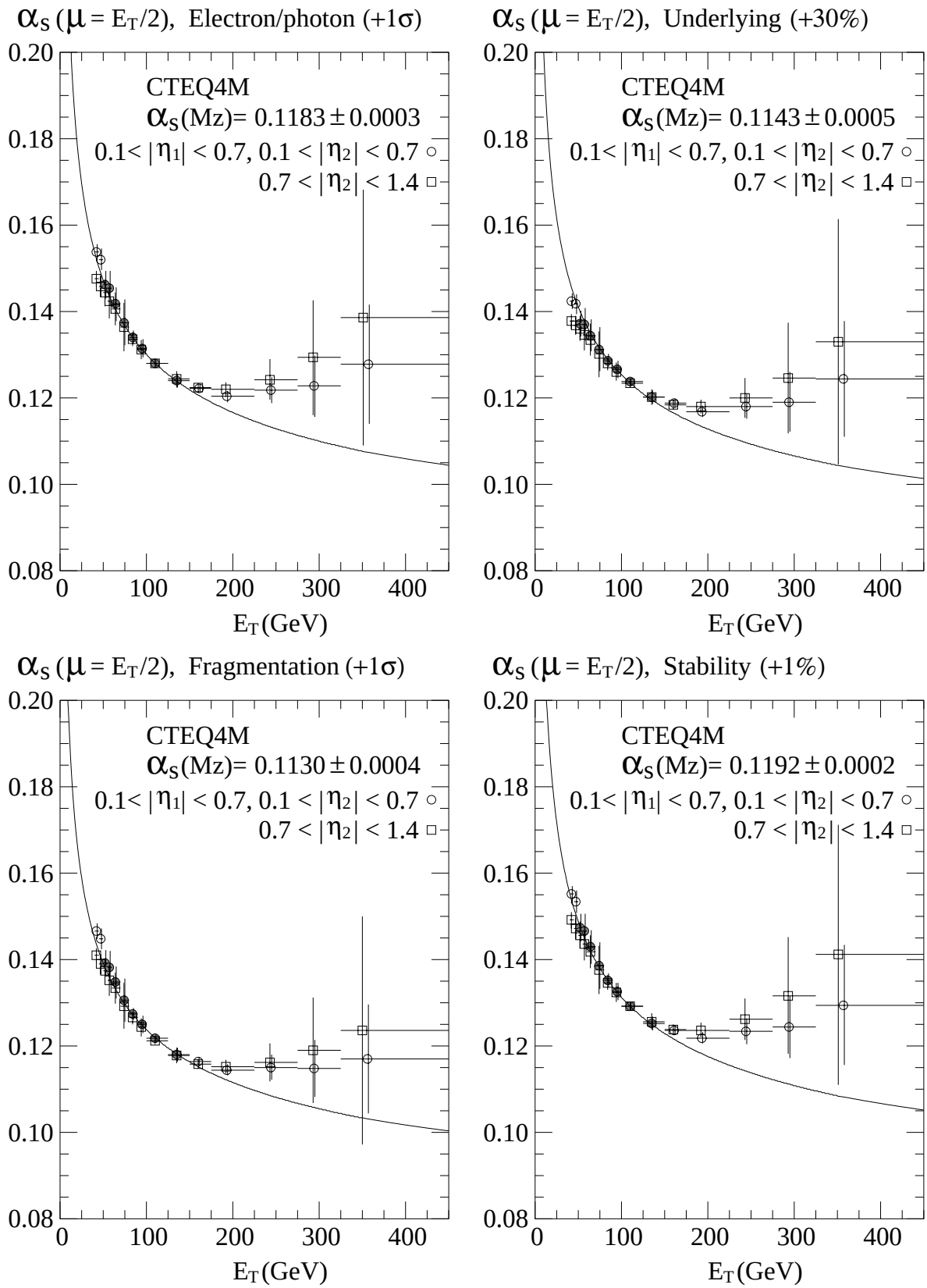

Figure 4.8: Similar to Fig. 4.6, but the cross section is deviated due to the electron/photon response uncertainty ($+1\sigma$), the underlying event energy ($+30\%$), the parton fragmentation function ($+1\sigma$), or the calorimeter energy scale instability ($+1\%$), respectively.

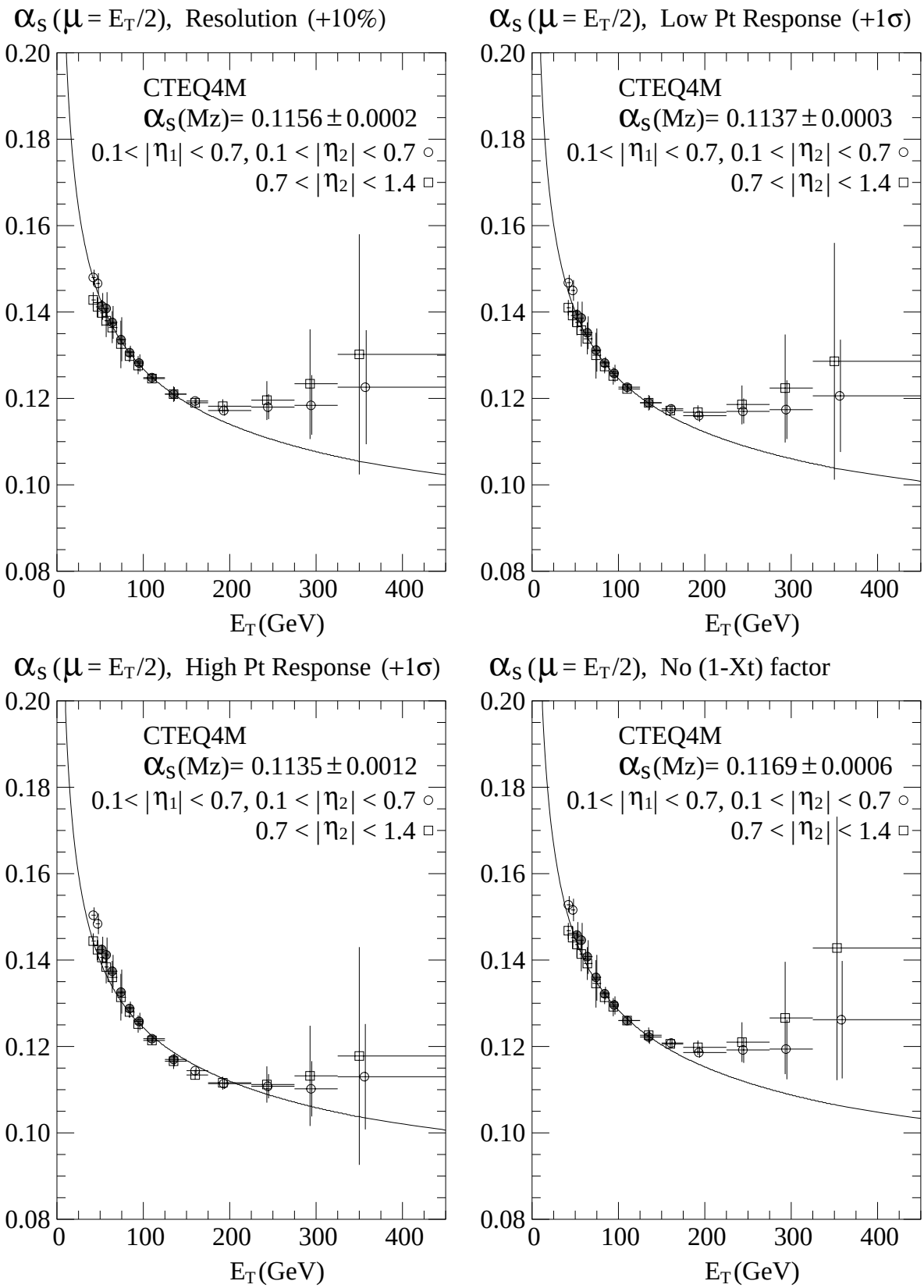

Figure 4.9: Similar to Fig. 4.6, but the cross section is deviated due to the jet energy resolution uncertainty (+10%), the calorimeter response to charged pions at low p_T ($+1\sigma$) or high p_T ($+1\sigma$), or the response function simplified to P6 in Eq.(3.9) being 0, respectively.

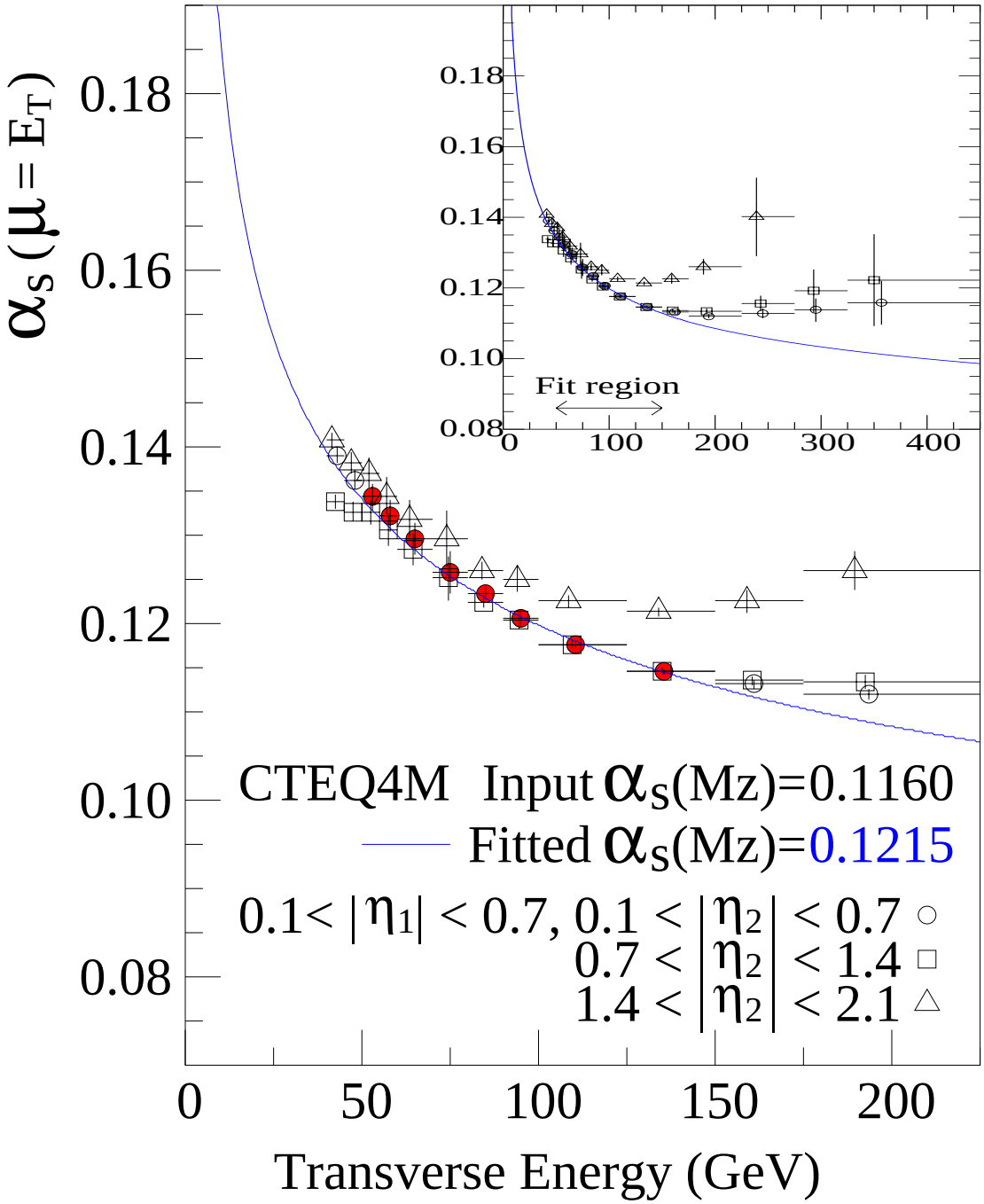

Figure 4.10: Similar to Fig. 4.2, but the energy scales are defined as $\mu = E_{\mathrm{T}}$. The best fit $\alpha_{\mathrm{s}}(\mathrm{M_Z})$ is 0.1215 ± 0.0004. The number of flavors is assumed to change to six at $\mu = 175$ GeV.

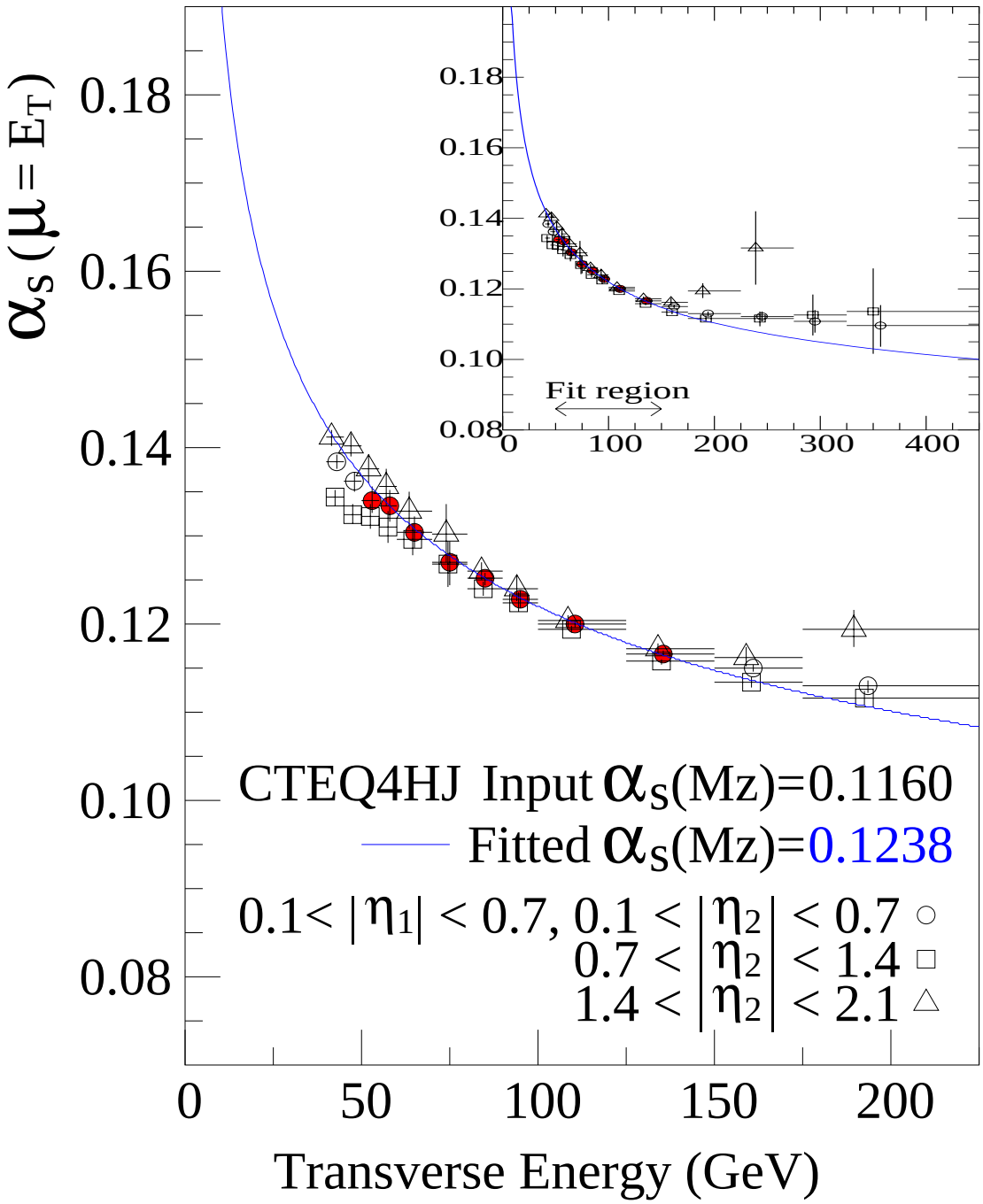

Figure 4.11: Similar to Fig. 4.3, but the energy scales are defined as $\mu = E_{\mathrm{T}}$. The best fit $\alpha_{\mathrm{s}}(\mathrm{M_Z})$ is 0.1238 ± 0.0004.

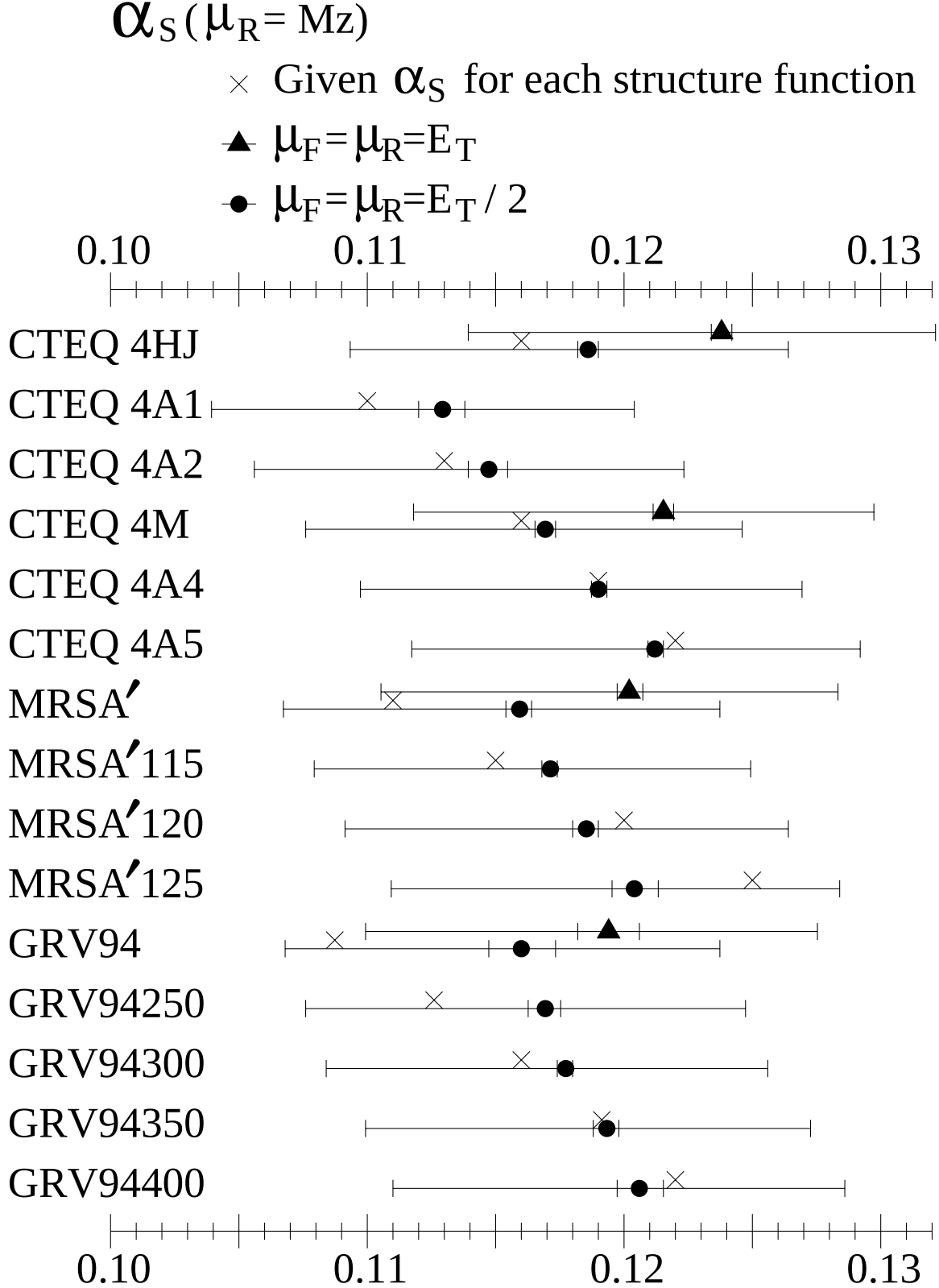

Figure 4.12: Summary of the $\alpha_s(M_Z)$ measurements. The obtained $\alpha_s(M_Z)$ values are shown for some of the recent structure functions. The circle and triangle are the central values of α_s with the factorization and renormalization scales defined as, $0.5E_T$ and E_T, respectively. The bar shows the statistical and total systematic error due to the cross section uncertainty; inside bar shows the statistical error only. X is the $\alpha_s(M_Z)$ used at parton evolution for each structure function.

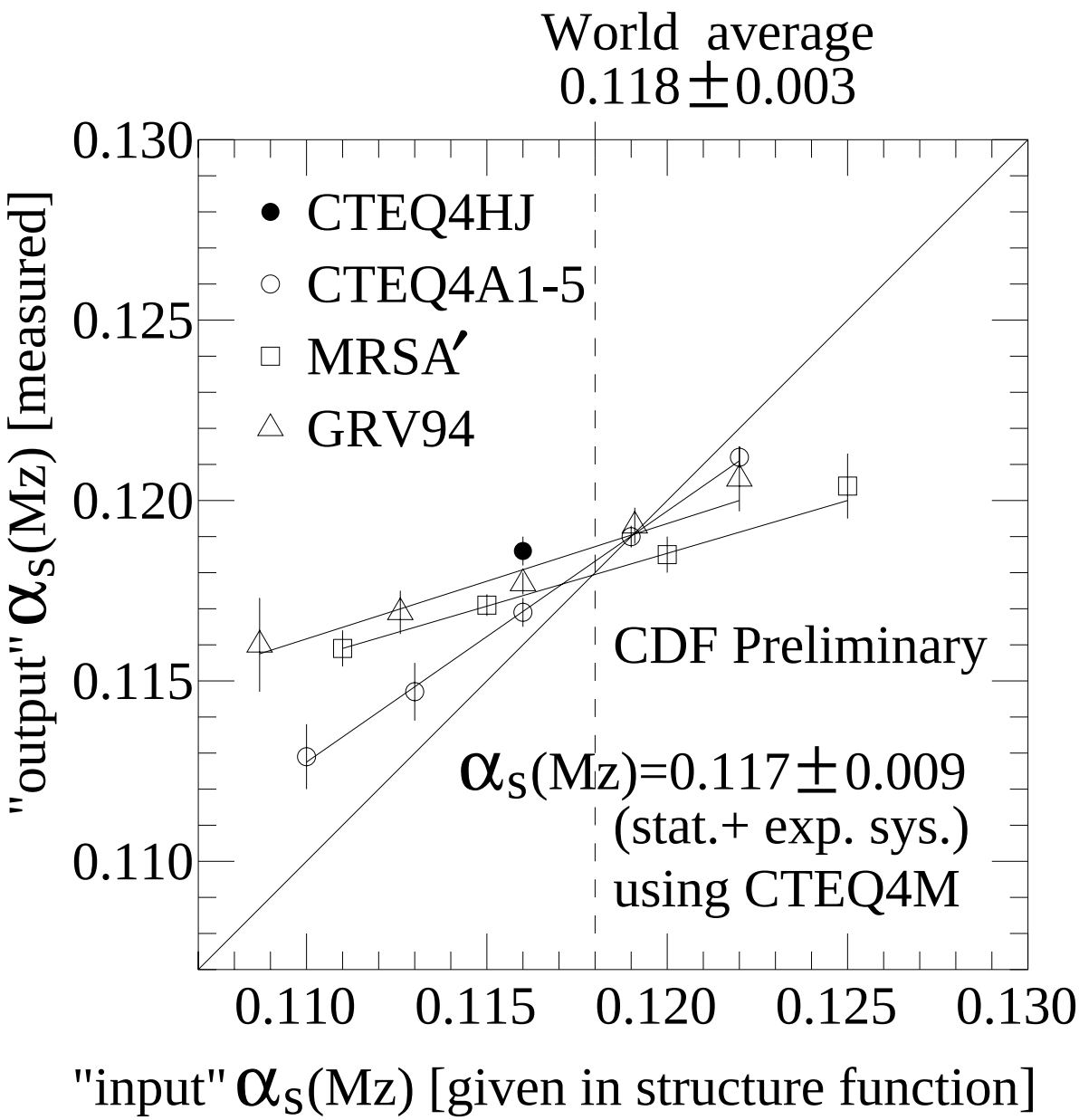

Figure 4.13: "Input" $\alpha_s(M_Z)$ versus "output" $\alpha_s(M_Z)$. "Input" $\alpha_s(M_Z)$ is the one used at parton evolution for each structure function. "Output" $\alpha_s(M_Z)$ is value obtained by a comparison with the experimental cross section. The vertical line shows the place where "Input" and "output" values are the same. CTEQ4M is equivalent to CTEQ4A3.

Chapter 5

Conclusion

We have performed the first measurement of the strong coupling constant α_s using two jet production cross sections in proton-antiproton collisions at a center of mass energy of 1.8 TeV. We have measured the two jet differential cross sections requiring one central jet ($0.1 < |\eta_1| < 0.7$) with $E_T > 40$ GeV and a second jet with $E_T > 10$ GeV in $0.1 < |\eta_2| < 3.0$. The measured cross sections are well described by next-to-leading order QCD calculation in the E_T range of the central jet up to 200 GeV and in the second jet η range of $0.1 < |\eta_2| < 1.4$. Since the magnitude and the shape of the cross section are sensitive to α_s through the higher order QCD processes, we extract α_s by fitting the cross section with a theoretical expectation. We have calculated the α_s values using various modern proton structure functions. The resulting α_s values are consistent to each other within $\Delta\alpha_s(M_Z) \simeq \pm 0.005$. The running feature of α_s is clearly seen in the transverse energy range between 50 and 150 GeV we considered. We quote $\alpha_s(M_Z) = 0.117 \pm 0.001(stat.) \pm 0.009(exp.sys.)$, where the central value is obtained with CTEQ4M structure functions and the systematic uncertainty is experimental only. This result is consistent with the PDG world average of 0.118 ± 0.003 [see Fig.5.1].

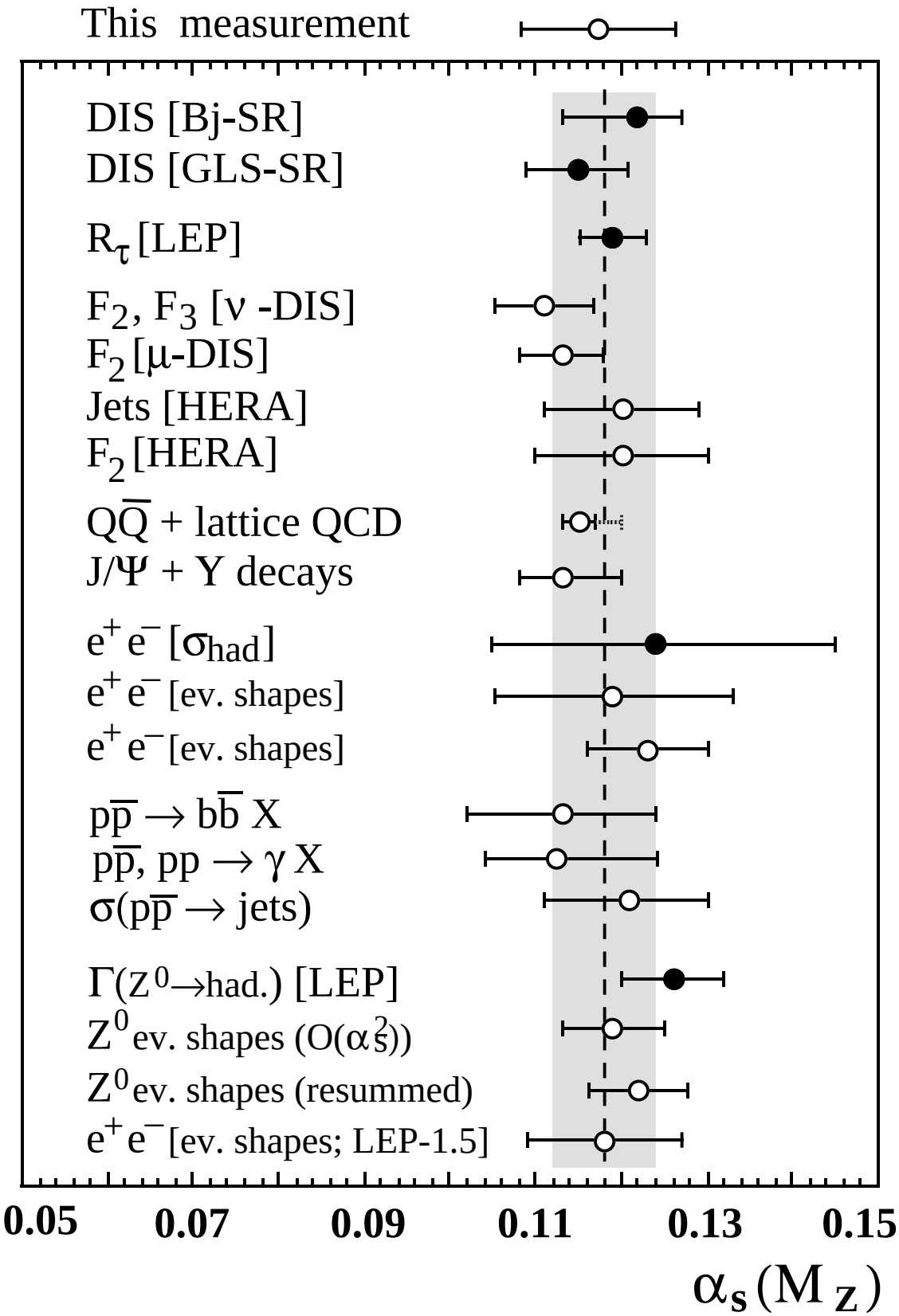

Figure 5.1: The result of $\alpha_s(M_Z)$ comparison with other measurements. Filled symbols are derived using NNLO QCD; open symbols are derived using NLO QCD or based on lattice calculations. The vertical line and the shaded area represent the world average of 0.118 ± 0.006, where the uncertainty of 0.006 corresponds to a estimate of a "90% confidence level", derived from the scatter of the individual results.

Bibliography

[1] S. Bethke, Nucl. Phys. **B** (Proc. Suppl.) **54**A, 314-324 (1997).

[2] D. J. Gross and F. Wilczek, Phys. Rev. Lett. **30**, 1343-46 (1973);
H. D. Politzer, Phys. Rev. Lett. **30**, 1346-49 (1973).

[3] W. Bartel *et al.*, Phys. Lett. **B 91**, 142-147 (1980).

[4] D. P. Barber *et al.* (MARK J collaboration), Phys. Lett. **B 89**, 139-144 (1979).

[5] W. Bartel *et al.* (JADE collaboration), Phys. Lett. **B 119**, 239-244 (1982).

[6] S. Bethke *et al.* (JADE collaboration), Phys. Lett. **B 213**, 235-241 (1988).

[7] T. van Ritbergen *et al.*, Phys. Lett. **B 400**, 379-384 (1997).

[8] W. A. Bardeen *et al.*, Phys. Rev. **D 18**, 3998-4017 (1978).

[9] Particle Data Group, R. M. Barnett *et al.*, Phys. Rev. **D 54**, 1-720 (1996).

[10] V. Branchina, M. Consoli, R. Fiore, and D. Zappalà, Phys. Rev. **D 46**, 75-83 (1992); R. Marshall, Z. Phys. **C 43**, 595-606 (1989).

[11] T. Hebbeker *et al.*, Phys. Lett. **B 331**, 165-170 (1994).

[12] M. A. Shifman, A. L. Vainshtein, and V. I. Zakharov, Nucl. Phys. **B 147**, 385-534 (1979).

[13] W. J. Marciano and A. Sirlin, Phys. Rev. Lett. **56**, 22-25 (1986).

[14] L. R. Surguladze and M. A. Samuel, Rev. of Mod. Phys. **68**, 259-303 (1986).

[15] M. Neubert, Nucl. Phys. **B 463**, 511-546 (1996).

[16] G. T. Bodwin, E. Braaten, and G. P. Lepage, Phys. Rev. **D 51**, 1125-71 (1995).

[17] M. Consoli, and J. H. Field, J. Phys. G: Nucl. Part. Phys. **23**, 41-67 (1997).

[18] M. Consoli, and J. H. Field, Phys. Rev. **D 49**, 1293-1301 (1994).

[19] W. Bartel *et al.* (JADE collaboration), Z. Phys. **C 33**, 23-31 (1986).

[20] K. Abe *et al.* (SLD collaboration), Phys. Rev. **D 51**, 962-984 (1995).

[21] S. Catani, L. Trentadue, G. Turnock, and B. R. Webber, Nucl. Phys. **B 407**, 3-42 (1993).

[22] M. Acciarri *et al.* (L3 collaboration), Phys. Lett. **B 371**, 137-148 (1996); M. Acciarri *et al.* (L3 collaboration), Phys. Lett. **B 404**, 390-402 (1997).

[23] R. D. Ball and S. Forte, Phys. Lett. **B 358**, 365-378 (1995).

[24] J. Chýla and A. L. Kataev, Phys. Lett. **B 297**, 385-397 (1992); W. G. Seligman *et al.* (CCFR collaboration), Phys. Rev. Lett. **79**, 1213-16 (1997).

[25] C. Albajar *et al.* (UA1 collaboration), Phys. Lett. **B 369**, 46-54 (1996).

[26] G. Sozzi *et al.* (UA6 collaboration), Phys. Lett. **B 317**, 243-249 (1993); G. Ballocchi *et al.* (UA6 collaboration), Phys. Lett. **B 317**, 250-256 (1993).

[27] J. Alitti *et al.* (UA2 collaboration), Phys. Lett. **B 263**, 563-572 (1991).

[28] D. Amidai *et al.*, "The Silicon Vertex Detector of the Collider Detector at Fermilab", CDF internal note 2398 (1993).

[29] The CDF collaboration, "Proposal for an upgraded CDF detecor", CDF internal note 1172 (1990).

[30] F. Snider *et al.*, Nucl. Instrum. Methods **A 268**, 75-91 (1988).

[31] F. Bedeschi *et al.*, Nucl. Instrum. Methods **A 268**, 50-74 (1988).

[32] F. Abe *et al.* (CDF collaboration), Phys. Rev. **D 50**, 2966-3026 (1994).

[33] L. Balka *et al.*, Nucl. Instrum. Methods **A 267**, 272-279 (1988).

[34] S. Bertolucci *et al.*, Nucl. Instrum. Methods **A 267**, 301-314 (1988).

[35] Y. Fukui *et al.*, Nucl. Instrum. Methods **A 267**, 280-300 (1988).

[36] W. C. Carithers *et al.*, "Performance and calibration studies of the CDF endplug hadron calorimeter", CDF internal note 368 (1985).

[37] G. Brandenburg *et al.*, Nucl. Instrum. Methods **A 267**, 257-271 (1988).

[38] S. Cihangir *et al.*, Nucl. Instrum. Methods **A 267**, 249-256 (1988).

[39] G. Ascoli *et al.*, Nucl. Instrum. Methods **A 268**, 33-40 (1988).

[40] A. Gauthier *et al.*, "Design and performance of drift chambers for the central muon upgrade of the CDF detector", CDF internal note 1500 (1991).

[41] F. Abe *et al.*, Nucl. Instrum. Methods **A 271**, 387-403 (1988).

[42] G. W. Foster *et al.*, Nucl. Instrum. Methods **A 269**, 93-100 (1988).

[43] E. Barsotti *et al.*, Nucl. Instrum. Methods **A 269**, 82-92 (1988).

[44] M. Bozzo *et al.* (UA4 collaboration), Phys. Lett. **B 147**, 392-398 (1984).

[45] F. Abe *et al.* (CDF collaboration), Phys. Rev. **D 44**, 29-52 (1991).

[46] F. Abe *et al.* (CDF collaboration), Phys. Rev. **D 50**, 5518-34 (1994).

[47] F. Abe *et al.* (CDF collaboration), Phys. Rev. **D 50**, 5550-61 (1994).

[48] N. Amos *et al.*, Phys. Rev. Lett. **68**, 2433-36 (1992).

[49] C. Grosso-Pilcher *et al.*, "Luminosity for the Top PRL", CDF internal note 3021 (1995).

[50] R. D. Field, and R. P. Feynman, Nucl. Phys. **B 136**, 1-76 (1978).

[51] F. Abe *et al.* (CDF collaboration), Phys. Rev. Lett. **65**, 968-971 (1990).

[52] S. Behrends, "Central Calorimeter Pion Response in Light of 1990 Test Beam Data", CDF internal note 1286 (1990).

[53] F. Abe *et al.* (CDF collaboration), Phys. Rev. **D 52**, 4784-4827 (1995).

[54] B. Flaugher, and S. Kuhlmann, "Underlying event energy in clusters", CDF internal note 685 (1988).

[55] S. Behrends, and A. F. Garfinkel, "Xt Scaling (Updated): Comparison of Jet Production at $\sqrt{s} = 546$ and 1800 GeV", CDF internal note 1650 (1992).

[56] W. T. Giele, E. W. N. Glover, and J. Yu, Phys. Rev. **D 53**, 120-130 (1996).

[57] W. T. Giele, E. W. N. Glover, and D. A. Kosower, Phys. Rev. Lett. **73**, 2019-22 (1994).

[58] H. L. Lai *et al.*, Phys. Rev. **D 55**, 1280-96 (1997).

[59] A. D. Martin, R. G. Roberts, and W. J. Stirling, Phys. Lett. **B 387**, 419-426 (1996).

[60] M. Glück, E. Reya, and A. Vogt, Z. Phys. **C 67**, 433-447 (1995).

[61] W. T. Giele, E. W. N. Glover, and D. A. Kosower, Nucl. Phys. **B 403**, 633-667 (1993).

[62] F. Abe *et al.* (CDF collaboration), Phys. Rev. Lett. **77**, 438-443 (1996).